

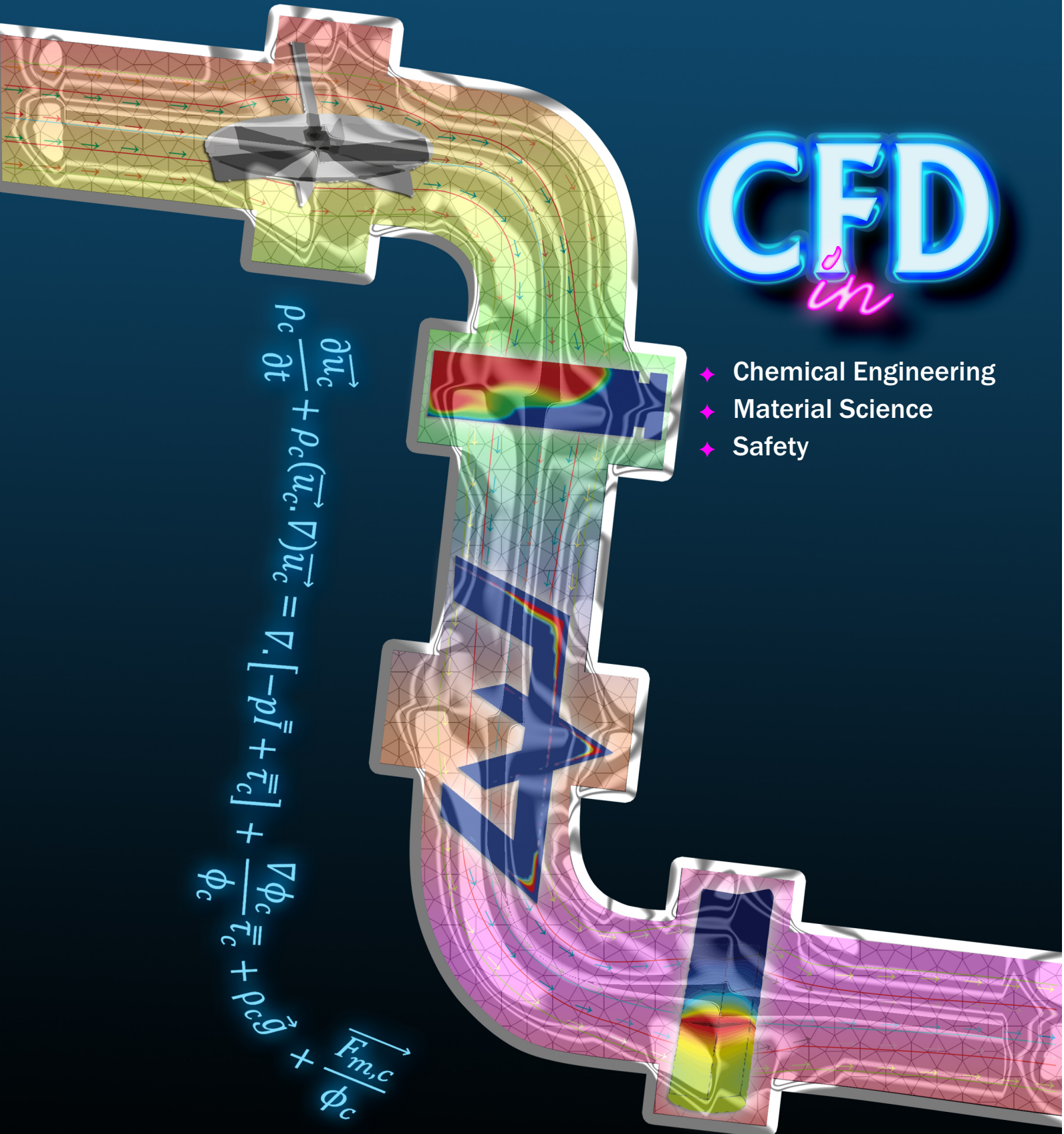


# BARC newsletter



Volume 379 | November-December 2021 | ISSN:0976-2108

On Applications of Computational Fluid Dynamics (CFD)



# CFD *in*

- ◆ Chemical Engineering
- ◆ Material Science
- ◆ Safety

$$\rho_c \frac{\partial \vec{u}_c}{\partial t} + \rho_c (\vec{u}_c \cdot \nabla) \vec{u}_c = \nabla \cdot [-p \vec{I} + \vec{\tau}_c] + \frac{\nabla \phi_c}{\phi_c} \vec{\tau}_c + \rho_c \vec{g} + \frac{F_{m,c}}{\phi_c}$$

**This page is intentionally left blank**

# BARC newsletter

Volume 379 | November-December 2021 | ISSN:0976-2108

On Applications of Computational Fluid Dynamics (CFD) in Chemical Engineering, Material Science & Safety

## PART-I

### 5. ASSOCIATE EDITOR'S MESSAGE

#### RESEARCH ARTICLES

### 9. Development of a CFD model for catalytic recombination of hydrogen and oxygen in a packed bed reactor

*Sachin Kamath et al*

### 17. 2-D simulation study of radioactive solid waste incinerator system

*Keyur C. Pancholi et al*

### 22. Synthesis of carbon nanotube aerogel by chemical vapour deposition - A CFD Study

*Amit Kaushal et al*

### 29. Quantification of lead melting in a radioactive transport cask using CFD

*P. Goyal et al*

### 36. Numerical modelling of deflagration to detonation transition in hydrogen air mixtures

*Aditya Karanam et al*

#### REVIEW ARTICLE

### 45. CFD modelling of solvent extraction equipment

*K.K. Singh et al*

#### BOOK REVIEW

### 59. CFD in nuclear reactor design and safety assessment

*Dr. R.B. Grover*

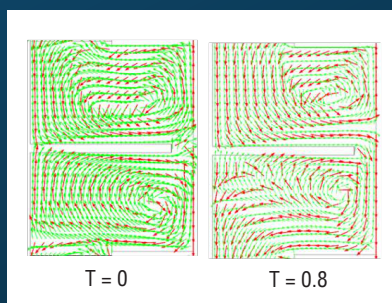
#### RESEARCH SYNOPSES

### 63. Diffusion and decomposition of SO<sub>2</sub>, Dispersion of aerosols, CFD modelling of pulsed disc doughnut column

*S. Sujeesh, N. Sen and S. Sarkar*



Bird's eye view of Bhabha Atomic Research Centre Mumbai



## PART-II

#### FEATURES SEGMENT

### 68. Nobel Prize 2021 in Sciences

*Musharaf Ali, B.S. Patro and K.K. Singh*

#### BOOK REVIEW

### 75. Natural hazards, impact assessment and eco-engineering through artificial intelligence

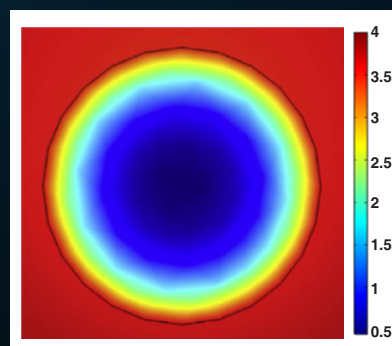
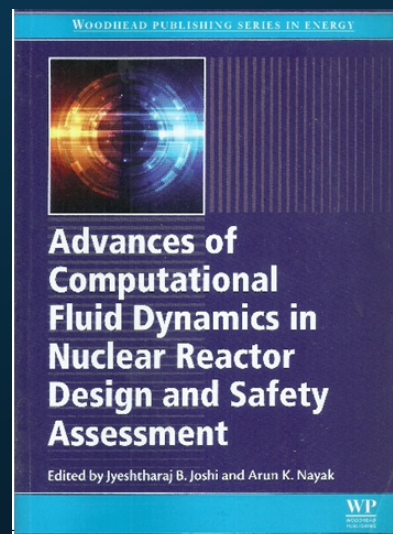
*Tirumalesh Keesari*

#### TECHNOLOGY TRANSFER AND HONORS

### 79. BARC develops titanium diboride ceramics

*Materials Group, BARC*

### 79. BARC scientist elected fellow of Indian National Science Academy



#### On the Cover

Artist's impression of fluid flowing in a pipe-shaped column

@Bhushan Chavan, SIRD

**This page is intentionally left blank**

# associate editor's MESSAGE



## Editorial Committee

### Chairman

Dr. A.P. Tiwari  
KMG

### Editor

Dr. S. Adhikari  
SIRD

### Members

Dr. A.K. Nayak, RED  
Dr. G. Sugilal, PSDD  
Dr. V.H. Patankar, ED  
Dr. (Smt.) B.K. Sapra, RP&AD  
Dr. L.M. Pant, NPD  
Dr. Ranjan Mittal, SSPD  
Dr. (Smt.) S. Mukhopadhyay, ChED  
Dr. K.P. Muthe, TPD  
Dr. V. Sudarsan, ChD  
Dr. A.V.S.S.N. Rao, AGS  
Dr. S.R. Shimjith, RCnD  
Dr. Sandip Basu, RMC  
Dr. Pranesh Sengupta, MSD  
Dr. R. Tripathi, RCD

### Member Secretary & Coordination

Shri Madhav N, SIRD

### Art, Design, Creative Work

Shri Bhushan S. Chavan, SIRD  
Shri Dinesh J. Vaidya, SIRD  
Shri Madhav N., SIRD

It gives me immense pleasure to bring out the first special issue of BARC Newsletter on the theme "Applications of Computational Fluid Dynamics in Chemical Engineering, Material Science and Safety".

While Computational Fluid Dynamics (CFD) is routinely used for analysis of thermal hydraulics and safety systems of nuclear reactors, the applications of CFD in chemical engineering, material science and safety (other than nuclear reactors) in BARC have emerged in last fifteen years or so. Chemical Engineering Division have played a key role in the applications of CFD modelling in the field of chemical engineering and, hence, was entrusted with the responsibility of bringing out this special issue.

This special issue has research articles and a review article. First two research articles are focused on the use of CFD in typical chemical engineering applications – one is focused on CFD modelling of catalytic recombination of hydrogen and oxygen in a packed bed reactor to analyze the reactor performance under different conditions of heat transfer and the other is focused on predicting concentration and temperature profiles in a diesel fired incinerator. The next research article is on the application of CFD in the field of material science, more precisely, on synthesis of carbon nanotubes using floating catalyst - chemical vapour deposition (FC-CVD) process. It elucidates the role CFD modelling can play to understand the effect of operating conditions of FC-CVD reactor on the properties of synthesized carbon nanotubes. The remaining two research articles are focused on applications of CFD in the field of safety. One of these articles is on CFD modelling of melting of lead shielding in casks used for transportation of radioactive material in the event of a fire. The other article on safety is focused on CFD modelling of deflagration to detonation transition (DDT) in hydrogen-air mixtures. Though the motivation of the authors to study DDT is the safety of containment of a nuclear reactor, the results are relevant for chemical processes which involve hydrogen either as a reactant or product. The research articles are followed by a review article which provides an overview of the approaches and challenges involved in CFD modelling of the equipment used in solvent extraction which is the most commonly used separation process in the front-end and the back-end of the nuclear fuel cycle.

The issue also contains three research synopses summarizing three recent papers on CFD modelling published by BARC colleagues in peer-reviewed international journals. The issue also contains a review of the book titled "Advances of Computational Fluid Dynamics in Nuclear Reactor Design and Safety Assessment". To the best of my knowledge, this is the first ever book review published in a BARC Newsletter. I hope subsequent issues will have more such book reviews.

I would like to express my heartfelt appreciation to the authors for contributing articles to this special issue, and the reviewers who have meticulously gone through the articles to ensure that they come out well. I would also like to thank Prof. R.B. Grover for contributing the book review.

I hope this special issue will motivate young researchers to take up CFD to understand and solve the problems in their respective areas of research in the broader domains of chemical engineering, material science and safety.

(K.K. Singh)

Chemical Engineering Division

**This page is intentionally left blank**



# **RESEARCH ARTICLES**

**This page is intentionally left blank**



# Development of a CFD model for catalytic recombination of hydrogen and oxygen in a packed bed reactor

Sachin Kamath\*, Sandeep K C, Kalyan Bhanja

Heavy Water Division, Chemical Engineering Group, BARC

## ABSTRACT

Oxygen production has become a crucial process to meet the increasing demand of medical grade oxygen during the current pandemic period. Water electrolysis is one of the techniques capable of producing high purity, medical grade oxygen. The oxygen gas produced by electrolyser at low current densities typical of that encountered in a renewable energy coupled water electrolyser system consists of hydrogen impurity which can hinder continuous operation schedule of the system. A catalytic recombiner consisting of copper beads, catalytic and non-catalytic alumina beads is designed to mitigate hydrogen impurity present in the oxygen stream. Development of a CFD model is necessary to test certain Beyond Design Basis Accident (BDBA) scenarios which are not possible to be examined experimentally due to explosive nature of the gases. Accordingly, a CFD model is developed to predict the performance of packed bed reactor system under different modes of operation and at different impurity levels. The study recommends against the operation of reactor in the adiabatic mode or isothermal mode. In the adiabatic mode, very high temperatures are encountered at high hydrogen impurities whereas operation of the bed at coolant temperature, leads to water vapour condensation in the catalytic section thus impacting the hydrogen conversion rate. Hence, it is advisable to operate the reactor at temperatures above the expected dew point temperature of the gas mixture.

**Keywords:** Computational Fluid Dynamics Model, Catalytic Recombiner, Oxygen Purification, Packed Bed Reactor, Adiabatic Case, Isothermal Wall, Convective Heat Transfer

## Introduction

During the present COVID – 19 pandemic, oxygen has become the most vital, life saving element of the periodic table. The conventional processes used for oxygen production are mainly based on separation of air using liquefaction or selective adsorption technique. The cryogenic air distillation process separates the constituents of air based on difference in their respective vapour pressures [1,2]. This technology has been the preferred choice for large- scale production of high purity oxygen to the tune of around more than 1000 MT/day[3]. On the other hand, the selective adsorption process makes use of synthetic zeolites like molecular sieves for preferential adsorption of air constituents based on their molecular diameter. This technology has the capability of producing oxygen at scale of 100 MT/day, however, the maximum purity attainable in a single cascade is limited to approximately 95% [3].

Water electrolysis is one of the non-conventional techniques for production of oxygen directly from water[4]. This non – air based process utilises DC electricity sourced from solar, wind, tidal or nuclear energy resources to split demineralised water into hydrogen and oxygen at near ambient conditions. The electrolyser can be operated in on demand and on site basis thus serving as both centralised as well as decentralised source for hydrogen and oxygen supply[5]. The hydrogen and oxygen gases produced by electrolysis method are relatively pure but require further purification as a polishing step for direct end use application. There is an inherent, small crossover of hydrogen and oxygen gases through the diaphragm employed in an electrolyser cell module. This could be attributed to the presence of slight differential pressure across the diaphragm. The mixing of gas soluble anolyte and catholyte is also cited as another reason resulting in increased hydrogen concentration in oxygen stream due to concentration gradient driven diffusion pathway[6].

Depending upon the construction, design and operation of the electrolyser cell, the hydrogen impurity in oxygen stream in industrial electrolysers is limited to 2%. The operation of electrolyser system at low current densities especially when coupled to renewable energy can lead to impurities beyond the set industrial range. This would severely affect and limit the operating schedule of the system thus interrupting vital oxygen flow from the electrolyser system[7]. In order to avoid this scenario and ensure uninterrupted, prolonged operation of electrolyser without safety shutdown, the impure oxygen gas stream can be further purified

using a passive method wherein the hydrogen impurity reacts with stoichiometric proportions of the bulk oxygen gas over a suitable catalyst in a reactor. This process is usually referred to as the catalytic recombination of hydrogen and oxygen gas to produce water using supported Platinum Group Metal (PGM) catalysts.

In the present study, the electrolyser operates at a low current density (2000 Ampere per square meter (ASM)) corresponding to 40% electrolyser loading. At this condition, the oxygen production flowrate is 2 Nm<sup>3</sup>/hr and hydrogen impurity is considered to be up to 2.5%. A catalytic recombiner is designed in order to ensure continuous and complete conversion of hydrogen impurity. The model developed in this article analyses reactor behaviour in terms of temperature reached by the bed under different modes of operation and also at different impurity levels.

### Estimation of packed bed flow parameters

The catalytic recombiner (CR) is a packed bed reactor which consists of sections of copper beads of 5 mm diameter, alumina beads and 0.5 % (w/w) Pd on alumina beads of approximately 4 mm diameter as catalyst for the recombination reaction.

The product gas from the electrolyser is moist and assumed to be fully saturated at 30 deg C. The corresponding water vapour is adsorbed in a silica gel – molecular sieve bed. The moisture-free gas then enters the CR filled with copper beads up to 100 mm length followed by 50 mm length each of catalytic and non-catalytic alumina beads. These are then followed by 100 mm length of copper beads as shown in the computational domain shown in Fig. 1. The non-catalytic alumina section downstream of the catalytic alumina section helps in slowing down the rate of heat transfer to coolant stream due to relatively lower thermal conductivity and higher heat capacity as compared to copper. As a result, moisture produced during recombination reaction is prevented from condensing over the catalytic section. This justifies the presence of a non-catalytic alumina section between the catalytic alumina and the copper beads section. An alternative arrangement is to introduce coolant stream near non-catalytic sections and provide heater with temperature controller over catalytic section in order to always maintain catalytic section at temperatures conducive to reaction kinetics.

The design of the reactor involves determination of diameter

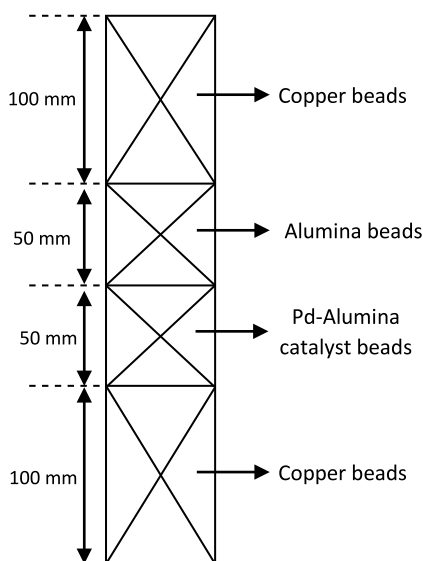


Fig. 1: Geometry of problem domain

of the packed bed which meets the maximum pressure drop restrictions in the bed for a maximum feed gas flow rate corresponding to 2 Nm<sup>3</sup>/hr.

Pressure drop in a packed bed can be calculated using Ergun's equation (Equation (1)) which is a combination of Kozeny – Karman equation for laminar flow (1<sup>st</sup> term on R.H.S of Equation (1)) and Burke – Plummer equation (2<sup>nd</sup> term on R.H.S of Equation (1)) for turbulent flow of the reacting fluid [8]. The sphericity is taken as unity since spherical beads are assumed.

$$\frac{\Delta P}{L} = \frac{150\mu(1-\varepsilon)^2}{d_p^2\varepsilon^3}\bar{u} + \frac{1.75\rho(1-\varepsilon)}{d_p\varepsilon^3}\bar{u}^2 \quad (1)$$

In this study, it is desirable to maintain laminar flow conditions in the bed to restrict the pressure drop values to a lower range. To ensure laminar flow conditions, the particle Reynolds number ( $Re_p$ ) defined by Equation (2) should be less than 20 [9].

$$Re_p = \frac{d_p\bar{u}\rho}{\mu} = 20 \quad (2)$$

At very low particle Reynolds number, the overall reaction may be controlled by external mass transfer effects. Since the concentration of impurities present in the oxygen gas stream is less, the thermo physical properties of pure oxygen gas are used for determination of dimensionless numbers, pressure drop, etc. Using Equation (2), the superficial velocity of oxygen gas stream is estimated which is later substituted in the Kozeny-Karman equation (Equation (3)) to evaluate the bed pressure drop. The bed porosity is estimated using the bulk and true density of alumina and copper beads Equation (4).

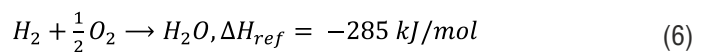
$$\frac{\Delta P}{L} = \frac{150\mu(1-\varepsilon)^2}{d_p^2\varepsilon^3}\bar{u} \quad (3)$$

$$\varepsilon = 1 - \frac{\rho_B}{\rho_t} \quad (4)$$

The bed diameter is calculated based on the superficial velocity of oxygen from Equation (5).

$$D = \sqrt{\frac{4Q}{\pi\bar{u}}} \quad (5)$$

The reaction between hydrogen (H<sub>2</sub>) and oxygen (O<sub>2</sub>) is represented by Equation (6).



Hydrogen acts as a limiting reactant in our case and due to low impurity levels, the reaction can be considered as a pseudo first order reaction with respect to hydrogen and can be expressed using Equation (7) [10]. The diffusion phenomenon is accounted by the apparent rate of recombination reaction consisting of both extrinsic as well as intrinsic mass transfer effects which are lumped together in the form of an effective activation energy and an effective pre-exponential factor as shown in Equation (7).

$$-r_{H_2} = 1.96 \times 10^{11} \exp\left(\frac{-73.77 \times 10^3}{RT}\right) C_{H_2} \quad (7)$$

The fractional change in the system volume is considered to be negligible considering the low concentration of hydrogen and water vapour as compared to oxygen.

## Development of CFD model for catalytic recombiner

A CFD model is developed in order to evaluate the steady state performance of the reactor in beyond design basis events wherein the oxygen gas stream entering the reactor contains hydrogen impurity level of more than 4%. CFD becomes an important tool in studying such events since it is not safe and advisable to carry out experiments in explosive range of the gas mixture (4 – 96% H<sub>2</sub> in O<sub>2</sub>).

The model is developed using a multi-physics approach to predict the performance of the recombiner system. The recombiner is modelled as a 2D axi-symmetric domain with the centre axial line of the reactor considered as  $r = 0$ . The recombiner model solves governing equations of flow, reactive species transport and energy balance in porous media. The governing equations of the model are described in subsequent sections.

The following assumptions have been made while developing the model:

- 1) Thermo physical properties of oxygen stream are considered to be constant with respect to the concentration of its constituents throughout the reactor. Hence, the density of the gas is assumed to be constant in the fluid flow equations. These properties are calculated for pure oxygen gas and are a function of temperature.
- 2) The effect of moisture in reduction of the catalytic activity is not considered in this model.
- 3) The back mixing effects are negligible in the packed bed.
- 4) The gas entering the reactor is assumed to be free from moisture. Hence, rate of reaction described by Equation (7) on dry basis can safely be used in the model.
- 5) All properties including bed porosity are considered to be isotropic.

### Darcy's law (Momentum Conservation)

The Darcy's law describes fluid velocity through a packed bed in terms of viscosity of the fluid and permeability of the bed (Equation (8)). The equation indicates a linear relationship between the velocity and bed pressure drop [11]. This is obvious for laminar flow profile of a fluid passing through a packed bed. The Kozeny – Karman equation can be re-arranged and presented as Equation (9).

$$\bar{u} = -\frac{k}{\mu} \left( \frac{\Delta P}{L} \right) \quad (8)$$

$$\bar{u} = \frac{d_p^2 \varepsilon^3}{150(1-\varepsilon)^2 \mu} \left( \frac{\Delta P}{L} \right) \quad (9)$$

Comparing Equations (8) & (9), the bed permeability which is required as an input for the model can be determined (Equation (10)). This value is observed to be a function of the particle diameter and bed porosity.

$$k = \frac{d_p^2 \varepsilon^3}{150(1-\varepsilon)^2} \quad (10)$$

A no slip boundary condition is applied at the wall as described by Equation (11) whereas a normal inflow velocity boundary condition (Equation (12)) is applied at the inlet of the reactor. The exit at top of the reactor is considered open to atmosphere ( $p = 0$ ).

$$\bar{u} = 0 \quad (11)$$

$$-n \cdot \bar{u} = u_0 \quad (12)$$

The velocity profile obtained from Darcy's law is used as an input for solving species and energy transport equations for estimation of the respective convective transfer phenomena whereas the temperature profile predicted by solution of energy transport equation helps in calculation of the temperature dependent thermo physical properties required for solving Darcy's law equation. The temperature profile also helps in determination of temperature dependent rate constant of the recombination reaction incorporated in the species transport equation. In this way, the developed model strongly couples the various physics involved in the recombination reactor.

### Heat Transfer through Porous Media (Thermal Energy Conservation)

The heat transfer equation solved in the model is presented in Equation (13). Thermal conductivity and specific heat capacity of the bed is contributed by solid beads as well as oxygen gas stream flowing through it. Hence, effective thermal conductivity of the bed is described as a function of bed porosity and respective thermal conductivities of the beads and oxygen gas. Similarly, specific heat capacity of the bed ( $\rho C_p$ )<sub>eq</sub> is a function of bed porosity, respective heat capacities and densities of beads and oxygen gas as represented in Equation (14) [11].

$$(\rho C_p)_{eq} \bar{u} \cdot \nabla T = \nabla \cdot (k_{eq} \nabla T) + Q_s \quad (13)$$

$$k_{eq} = \varepsilon k_f + (1 - \varepsilon) k_p \quad \& \quad (\rho C_p)_{eq} = \varepsilon \rho C_p + (1 - \varepsilon) \rho_s C_{ps} \quad (14)$$

The heat of recombination reaction acts as a heat source for the packed bed reactor. Rate of heat transferred to the bed depends upon the reaction kinetics between hydrogen and oxygen and is expressed by Equation (15). The heat of reaction is calculated at steady state temperature attained by the system.

$$\bar{Q}_s = (-r_{H_2}) \cdot \Delta H \quad (15)$$

The bed inlet boundary condition is fixed as  $T = 303$  K. An outflow boundary condition as described by Equation (16) is applied to the bed outlet wherein heat transfer is only by convection.

$$-n \cdot (-k_{eq} \nabla T) = 0 \quad (16)$$

The heat generated by the reactor is removed using chilled water which flows through a jacket enveloping the reactor bed. Three different heat transfer boundary conditions can be envisaged at the reactor wall during reactor operation:

(1) Constant heat transfer coefficient case: In this case, there exists a finite overall heat transfer coefficient which helps in transfer of heat from the reactor to the external cooling fluid. The boundary condition for this case is described by Equation (17). The heat transfer coefficient for present case is taken from literature [12]. In the present study,  $T_{ext}$  is considered to be 283 K.

$$-n \cdot (-k_{eq} \nabla T) = h(T_{ext} - T) \quad (17)$$

(2) Adiabatic case: The reactor wall is considered to be thermally insulated to estimate maximum wall temperature for safety purposes. This situation arises when the cooling circuit has

failed and developed a huge leak. In this case, the heat transfer from wall to surrounding chilled water does not take place. However, heat of recombination reaction continues to heat the beads and some amount of this heat is also carried away by the gas due to forced convection. The equation used to represent this condition at the wall is expressed as Equation (16).

(3) **Constant wall temperature case:** In this case, the reactor wall is maintained at a lower uniform temperature equivalent to the chiller water temperature. This case arises when the overall heat transfer coefficient is very high so that the cooling fluid is able to maintain a constant temperature ( $T = T_{ext} = 283 \text{ K}$ ) over the reactor wall.

### Mass Transport through Porous Media (Mass Conservation)

Mass transfer phenomenon occurring within the packed bed reactor involves mass transfer due to diffusion, adsorption and convection along with back mixing effects, which is characterized by dispersion coefficient [12]. The participating species that are either produced or consumed during reaction are accordingly accounted by source or sink terms. The dispersion due to back mixing effects and mass transfer due to adsorption are assumed to be negligible to simplify the model. The internal diffusion phenomenon and external mass transfer effect are accounted by apparent rate of recombination reaction expressed by Equation (7)[10]. The intrinsic and extrinsic effects have been accounted in Equation (7). The mass conservation equations solved for  $i^{\text{th}}$  component are given by Equations (18) and (19).

$$\nabla \cdot \bar{N}_i = S_i \quad (18)$$

$$\nabla \cdot \bar{N}_i = \bar{u} \cdot \nabla C_i \quad (19)$$

Source and sink terms are derived from the rate of reaction for the individual components as presented in Equation (20) [13].

$$-(r_{H_2}) = -2(r_{O_2}) = (r_{H_2O}) \quad (20)$$

A no-flux boundary condition for the species is applied at the reactor wall (Equation (21)). Inward flux of the individual species is specified at the bed inlet (Equation (22)) and outflow boundary condition describes the bed outlet (Equation (23)).

$$-n \cdot \bar{N}_i = 0 \quad (21)$$

$$-n \cdot \bar{N}_i = N_{0,i} \quad (22)$$

$$-n \cdot D_i \nabla C_i = 0 \quad (23)$$

### Results and Discussion

Pressure profile in the bed is presented in Fig. 2 (a) and Fig. 2 (b). The pressure drop in each section of the bed is different due to difference in bead diameter and bulk density of alumina (catalytic and non-catalytic) and copper beads. The main differentiating factor in Darcy's equation used in the model is permeability of the bed. Slope of the graph indicates resistance to fluid flow in the packed bed. The pressure drop is comparatively more in alumina bead (catalytic and non-catalytic) section due to low bed permeability value in that region.

#### Constant heat transfer coefficient case

The catalytic bed is cooled using chilled water to remove the exothermic heat of reaction. This will prevent overheating of catalyst and also avoid formation of hotspots in the bed. The

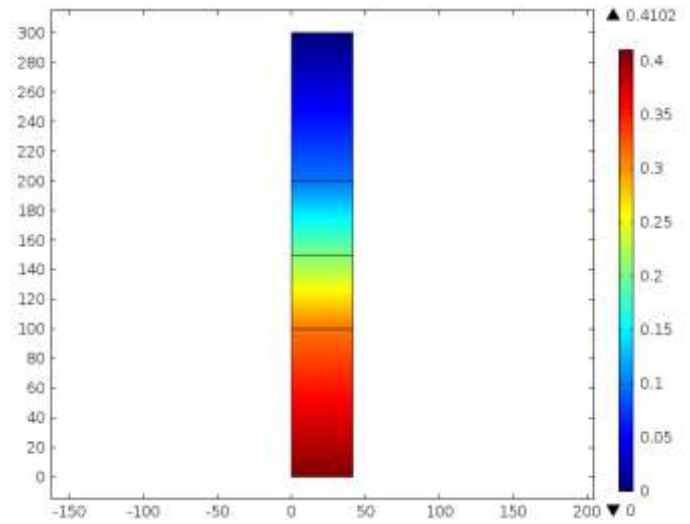


Fig.2 (a): Surface plot of pressure profile in the reactor (Pressure unit: Pa)

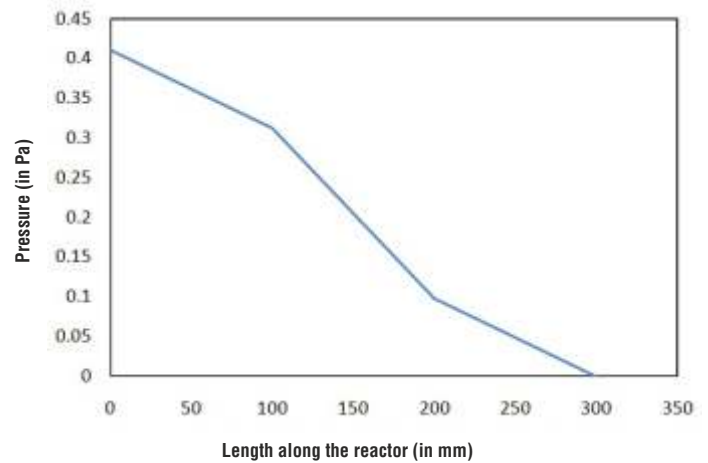


Fig.2 (b): Variation of pressure along the length of the reactor

overall heat transfer coefficient is considered to be approximately  $285 \text{ W/m}^2\text{K}$  with chilled water inlet temperature of  $283 \text{ K}$  [12]. Accordingly, a convective heat flux boundary condition is employed at wall boundary to simulate dissipation of heat from bed to the coolant stream.

A grid independence test is essential to ensure that the simulation results are independent of the grid size. The mesh consists of unstructured triangular type mesh which is defined by the maximum and minimum element size. Analysis is carried out on the axial temperature plot of packed bed with maximum mesh element size ranging from  $0.277 \text{ mm}$  to  $9.11 \text{ mm}$ . The details of the various mesh element sizes used in this analysis are tabulated in Table 1. The maximum temperature predicted by the model is observed to be constant within acceptable limits for mesh sizes below  $1.86 \text{ mm}$ . This mesh size is used for further studies. The error is calculated by subtracting the corresponding temperature value from the successive value for the lower mesh and dividing the difference by value at the lower mesh.

Temperature profile in the bed for this condition with  $2.5\%$  hydrogen impurity in oxygen stream is shown in Fig. 3 (a) and Fig. 3 (b). A sharp increase in temperature is noticed when gas enters the catalyst section implying a rapid decrease in the hydrogen impurity content of the gas which is attributed to the high reaction

**Table 1:** Details of mesh element sizes

Sr. No.	Element size		No. of Domain elements	No. of boundary elements	Maximum Temperature (K)	Location of maximum (mm)	Error (%)
	Maximum (mm)	Minimum (mm)					
1.	9.11	0.29	448	93	316.1176	108.3155	0.79
2.	2.77	0.124	4184	291	318.6624	102.7698	0.09
3.	1.86	0.0828	9288	439	318.9506	101.8274	-0.085
4.	1.45	0.0414	15148	561	318.6812	101.4281	0.033
5.	0.277	$8.28 \times 10^{-4}$	453686	2918	318.7862	101.9336	-

rate between oxygen and hydrogen. This effect is supported by the hydrogen conversion plotted in Fig. 4 for the catalytic alumina section. Heat generated by the catalyst is transferred by conduction to the upstream copper beads due to high conductivity of copper beads leading to preheating of the feed gas before it reaches the catalytic alumina bed. The high convective heat transfer coefficient ensures that the bed temperature decreases below the inlet gas temperature of 303 K near the catalytic alumina section.

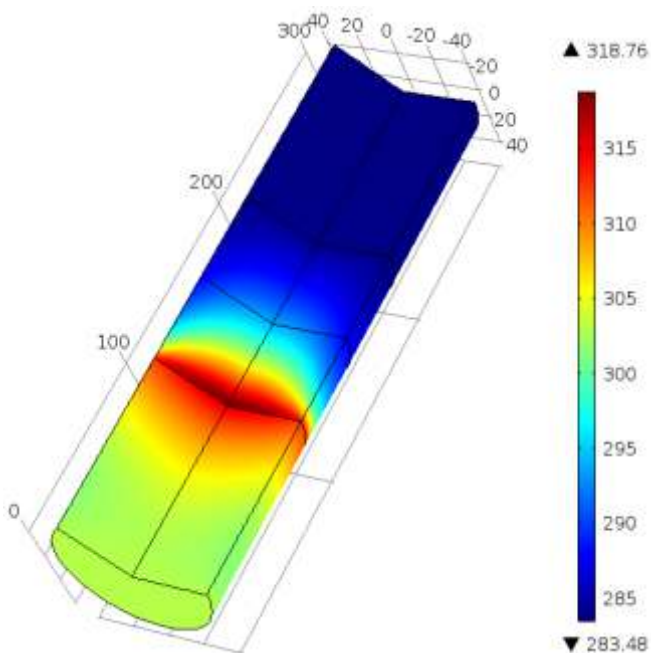


**Fig. 3(a):** Temperature profile in the reactor for constant heat transfer coefficient case (Temperature unit: K)

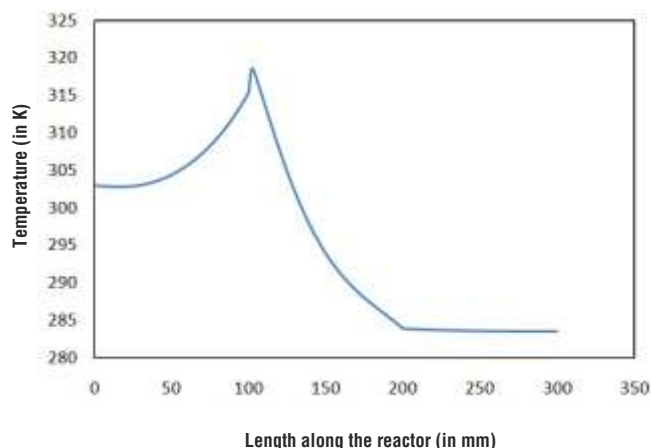


**Fig. 3(b):** Temperature along central axis of the reactor for constant heat transfer coefficient case

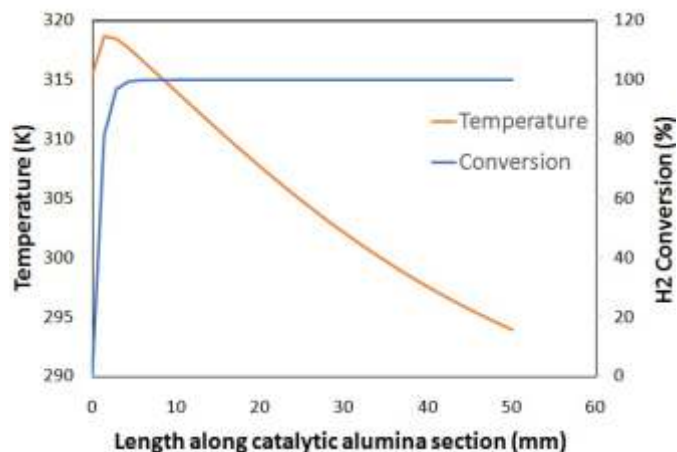


**Fig. 4:** Hydrogen conversion and temperature along central axis of the catalytic alumina section

The moisture content corresponding to 2.5% hydrogen impurity is equivalent to 2.5% in case of total conversion. This corresponds to a dew point of approximately 293 K. As seen in Fig. 3 (b), the temperature in the catalytic alumina section is observed to be above the corresponding dew point value, thus preventing condensation of water vapour on the catalyst. It is crucial to maintain the catalyst in a relatively dry state to avoid significant decrease in reaction rate which could further hamper the hydrogen conversion rate.

#### Adiabatic case

Chilled water supplied to the reactor is assumed to have failed in this case. The heat produced by the exothermic reaction is no longer dissipated to the coolant stream. To estimate the maximum temperature reached by the reactor wall, adiabatic boundary condition is considered at the wall. This expectedly leads to an increase in the central axial reactor temperature as compared to the convective heat transfer case as shown in Fig. 5 (a) and Fig. 5 (b).

The temperature rises steadily in the initial copper bead section, followed by a sharp increase at the beginning of the catalytic section which is later followed by a constant temperature regime in both the non-catalytic and copper bead section due to steady heat transfer by convection to the outgoing oxygen gas and by conduction to the non-catalytic alumina and copper bead section.

Since the present case results in higher bed temperatures, the model is used with hydrogen impurity varying from 1% to 10% to study the worst-case scenario expected in the bed. The results are presented in Fig. 6. It is observed that the maximum temperature encountered in the bed increases with increase in hydrogen impurity level in the feed, as is evident from Table 2.

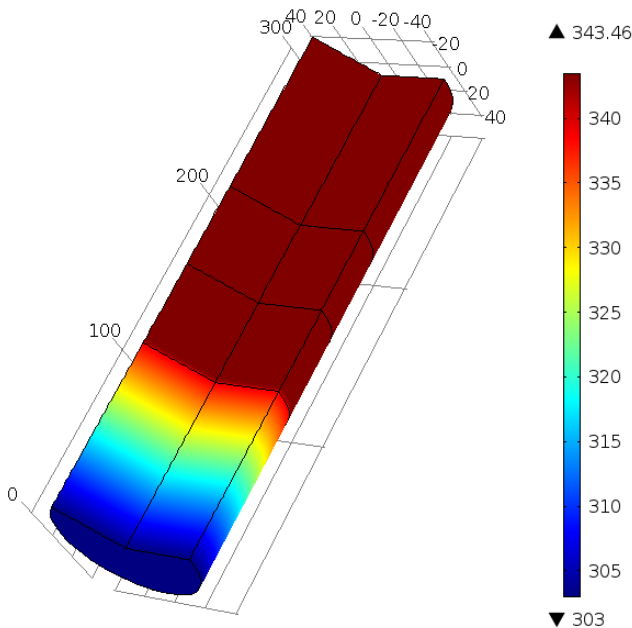


**Fig. 5(a):** Temperature profile of the reactor for adiabatic case (Temperature unit: K)

observed in the catalyst section due to the exothermic reaction. Thereafter, the product gas temperature decreases gradually in the non-catalytic section followed by a quick decline in the last copper bead section.

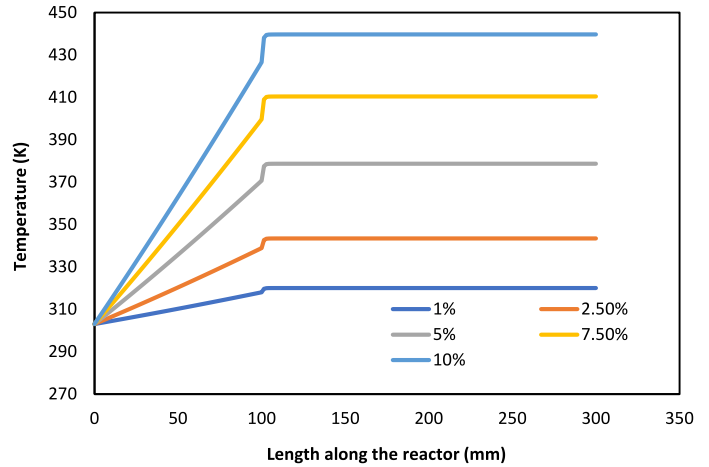


**Fig. 6:** Temperature along central axis of the reactor for adiabatic case with different hydrogen impurity levels

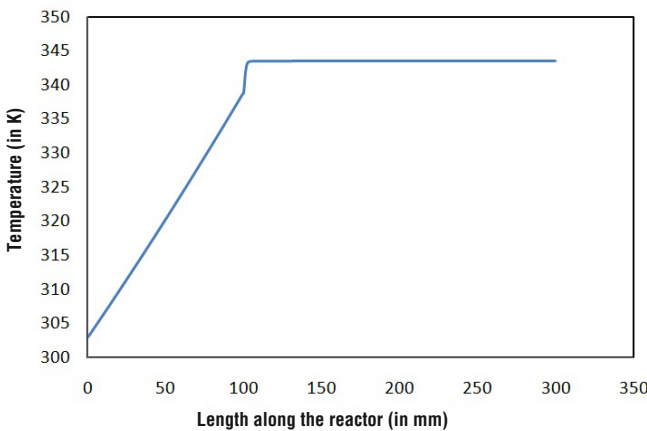


**Fig. 5(b):** Temperature along central axis of the reactor for adiabatic case

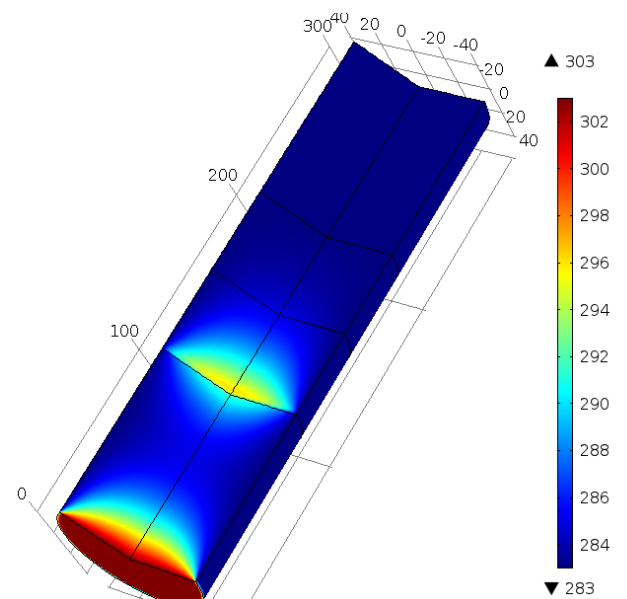


**Fig. 7 (a):** Temperature profile of the reactor for isothermal wall case (Temperature unit: K)

**Table 2:** Overall rise in temperature at different hydrogen impurity levels for adiabatic reactor

H <sub>2</sub> impurity in O <sub>2</sub> stream (%)	Overall rise in temperature (T <sub>max</sub> – T <sub>in</sub> ) (°C)
1	17
2.5	40.46
5	75.67
7.5	107.44
10	136.71

### Constant wall temperature case

In this case, it is assumed that the coolant flow rate is so high that temperature throughout the reactor wall is maintained at a constant value equivalent to the coolant inlet temperature. The temperature profile in the reactor and the temperature distribution along the reactor centre are plotted in Fig. 7 (a) and (b), respectively. It is observed that the copper beads in the initial section of the reactor rapidly cool the incoming oxygen gas, as a result of which the temperature of oxygen gas entering the catalytic alumina section is very low. A small spike in the gas temperature is

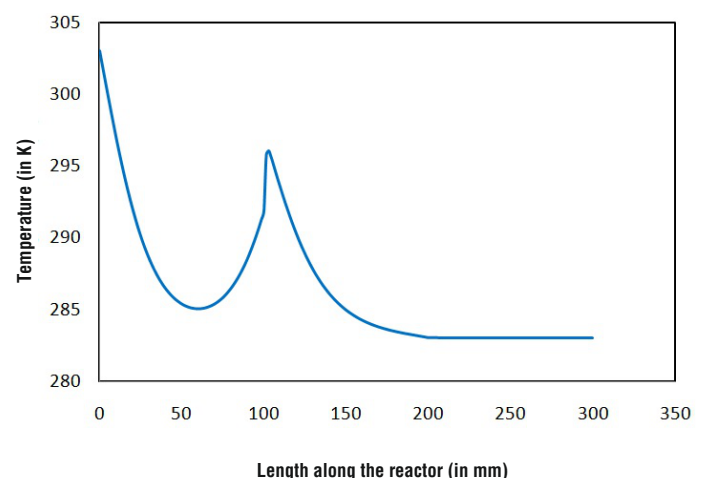


**Fig. 7 (b):** Temperature along central axis of the reactor in constant wall temperature case

It is important to note that temperature in bulk of the catalytic section is less than the dewpoint temperature of the product gas. This may lead to condensation of water vapours on the catalyst beads which would reduce the recombination reaction rate as well as hydrogen conversion. It is always desirable to maintain the bed temperature above dew point temperature of the product gas to avoid vapour condensation. Hence, it is recommended that the reactor should not be operated in this regime so that an appreciable rate of reaction and a significant conversion of hydrogen is achieved.

The reactor temperature profiles for all the above 3 cases are compared in Fig. 8. It is evident that the bed temperature in the isothermal wall case is lesser than that encountered for constant heat transfer coefficient case due to the presence of higher driving force for heat transfer in the isothermal wall case. As expected, higher bed temperature is reached by the bed when adiabatic boundary condition is imposed on the reactor wall.

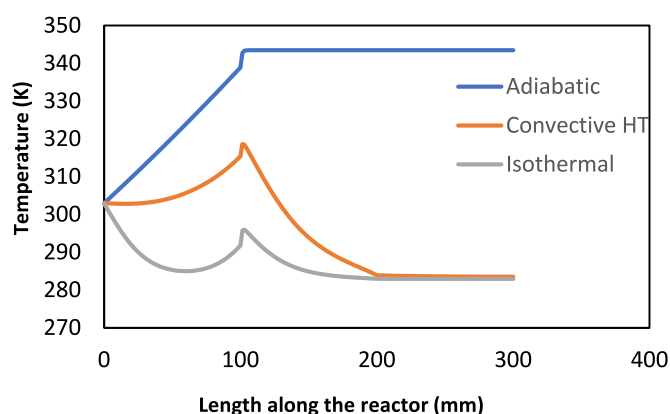


**Fig. 8:** Temperature along central axis of the reactor for all 3 cases compared in this study

## Conclusion

A model for predicting the performance of a packed bed catalytic recombiner in terms of pressure drop, temperature and hydrogen conversion has been developed. Performance of the reactor under the three modes of operation has been evaluated. The behaviour of reactor at different hydrogen impurities in the adiabatic case is also considered in the present study. In adiabatic case, very high temperatures are experienced in the bed whereas in isothermal wall case, the catalyst section encounters temperatures lower than the dew point which could lead to water vapour condensation on catalyst thereby reducing the recombination rate. Hence, the reactor operation in either of these modes should be avoided. This study recommends operation of reactor at temperatures above dew point temperature especially in the catalytic section in order to achieve complete conversion of hydrogen.

As a part of future studies, an experimental system of the recombination reactor would be set up and tested under safe, normal operating conditions. The data from the experimental test set up would be used for validation of the simulation results.

## Acknowledgement

The authors acknowledge the requisite computing support provided by Dr. K.K. Singh, Chemical Engineering Division (ChED), BARC.

## Notations

$\epsilon$	Bed porosity	-
$\mu$	Fluid viscosity	Pa.s
$\rho$	Density of oxygen stream	kg/m <sup>3</sup>
$\rho_s$	Density of beads	kg/m <sup>3</sup>
$\rho_B$	Bulk density of copper/ alumina beads	kg/m <sup>3</sup>
$\rho_t$	True density of copper/ alumina beads	kg/m <sup>3</sup>
$C_i$	Concentration of $i^{\text{th}}$ species	mol/m <sup>3</sup>
$C_{H_2}$	Concentration of hydrogen	mol/m <sup>3</sup>
$C_p$	Specific heat capacity of oxygen stream	kJ/kg.K
$C_{ps}$	Specific heat capacity of beads	kJ/kg.K
$d_p$	Diameter of copper/ alumina bead	m
$D$	Diameter of packed bed	m
$D_i$	Diffusivity of $i^{\text{th}}$ species	m <sup>2</sup> /s
$H$	Heat transfer coefficient	W/m <sup>2</sup> .K
$\Delta H$	Heat of reaction	kJ/kmol
$k$	Bed permeability	m <sup>2</sup>
$k_{eq}$	Equivalent thermal conductivity of packed bed	W/m.K
$k_r$	Thermal conductivity of fluid	W/m.K
$k_p$	Thermal conductivity of copper/ alumina bead	W/m.K
$L$	Length of packed bed	m
$\bar{N}_i$	Total flux of $i^{\text{th}}$ species	mol/m <sup>2</sup> .s
$N_{0,i}$	Flux of $i^{\text{th}}$ species at bed inlet	mol/m <sup>2</sup> .s
$P$	Pressure	Pa
$Q$	Volumetric flowrate of gas	m <sup>3</sup> /s
$Q_s$	Volumetric heat generation rate	W/m <sup>3</sup>
$-r_{H_2}$	Apparent rate of consumption of hydrogen	mol/m <sup>3</sup> .s
$r_{H_2O}$	Apparent rate of production of water vapour	mol/m <sup>3</sup> .s
$-r_{O_2}$	Apparent rate of consumption of oxygen	mol/m <sup>3</sup> .s
$R$	Universal gas constant	kJ/kmol.K
$Re_p$	Particle Reynolds number	-
$S_i$	Rate of production/ consumption of $i^{\text{th}}$ species	mol/m <sup>3</sup> .s
$T$	Temperature	K
$T_{ext}$	External temperature	K
$\bar{u}$	Superficial gas velocity	m/s
$u_0$	Superficial gas velocity at inlet	m/s

## Corresponding Author\*

Sachin Kamath (sachin@barc.gov.in)

## References

- [1] Industrial Oxygen: Its Generation and Use, ACEEE Summer Study on Energy Efficiency in Industry, 2007.

- [2] Improved Oxygen Production Technologies, IEA Green House Gas R&D Programme, 2007, 14.
- [3] Emerging and Existing Oxygen Production Technology Scan and Evaluation, COSIA, GHG Working Group, 2018.
- [4] Takeyoshi Kato, Mitsuhiro Kubota, Noriyuki Kobayashi, Yasuo Suzuki, *Energy*, 2005, **30**, 2580.
- [5] K.C. Sandeep, Sachin Kamath, Krunal Mistry, Ashok Kumar M, S.K. Bhattacharya, Kalyan Bhanja, Sadhana Mohan, *Int. Journal of Hydrogen Energy*, 2017 **42**, 12094.
- [6] Jörn Brauns, Thomas Turek, *Processes*, 2020, **8**, 248.
- [7] Philipp Haug, Matthias Koj, Thomas Turek, *Int. Journal of Hydrogen Energy*, 2017, **42**, 9406.
- [8] Warren L. McCabe, Julian C. Smith, Peter Harriott, Unit Operations of Chemical Engineering, McGraw-Hill International, Fifth edition., 1993.
- [9] O. Levenspiel, Engineering Flow and Heat Exchange, Springer, Third edition., 2014.
- [10] K.C. Sandeep, Rupsha Bhattacharyya, Chandrashekhar Warghat, Kalyan Bhanja, Sadhana Mohan, *Int. Journal of Hydrogen Energy*, 2014, **39**, 17906.
- [11] COMSOL Multiphysics documentation.
- [12] Convective Heat Transfer Coefficients Table Chart, [www.engineersedge.com/heat\\_transfer/convective\\_heat\\_transfer\\_coefficients\\_\\_13378.htm](http://www.engineersedge.com/heat_transfer/convective_heat_transfer_coefficients__13378.htm)
- [13] O. Levenspiel, Chemical Reaction Engineering, Wiley, Third edition, 1998.



# 2-D CFD simulation study of radioactive solid waste incinerator system

Keyur C. Pancholi<sup>\*1,2</sup>, S. Agarwal<sup>2</sup>, T. Vincent<sup>3,1</sup>, C.P. Kaushik<sup>2,1</sup>

<sup>1</sup>Homi Bhabha National Institute, Mumbai-400094, India

<sup>2</sup>Waste Management Division, Nuclear Recycle Group

<sup>3</sup>Process Development Division, Nuclear Recycle Group

Bhabha Atomic Research Centre, Trombay, Mumbai-400085, India

## ABSTRACT

Low active radioactive solid waste of Category-I nature ( $\leq 20$  mR/h) requires volume reduction before its eventual disposal in Near Surface Disposal Facility (NSDF). Conventional incineration is used for management of cellulosic waste which provides a volume reduction factor in the range 30-50. A 2D CFD (Computational Fluid Dynamics) study of an existing diesel fired solid waste incinerator is presented by simulating turbulent flow coupled with heat transfer and reactions to understand the temperature and concentration distributions inside the incinerator chamber during incineration of cellulosic waste. The temperature at a reference thermocouple location obtained from simulation is compared with actual operational data and a good agreement is observed. The results of the present study will form reference data of temperature and concentration distributions in the incinerator chamber for a similar study with plasma-based system planned for combustible waste forms.

**Keywords:** Incineration, Radioactive Solid Waste, Volume Reduction Factor, 2D CFD study

## Introduction

Large quantities of secondary solid wastes with potential radioactive contamination are generated from the operation and maintenance of nuclear power plants, the nuclear fuel cycle facilities, research laboratories, radiation facilities and medical facilities. These wastes have major contribution of Very Low-Level Waste and Low-Level Waste ( $\leq 20$  mR/h) [1,2], having more than 50% volume of combustible materials such as cellulose, rubber and plastics [3,4]. These wastes need to be treated and conditioned into a form acceptable for safe storage and disposal. Processes like incineration, compaction or melt densification [4,5] are in practice for the same. Incineration is the most preferred option as a treatment method due to associated advantage of high Volume Reduction Factor (VRF more than 30) [4,5]. Cellulosic wastes are generally treated by diesel fired incinerators.

At present a diesel fired incinerator of 50 kg/h capacity is in use at Solid Waste Management Facility of Waste Management Division of BARC for effective management of potentially contaminated cellulosic wastes. A CFD simulation study of

incineration chamber of this system for processing of cellulosic waste using diesel burner has been performed. The study provides useful insights into the concentration and temperature distributions inside the incineration chamber. Temperature at the reference thermocouple location obtained from CFD simulation is compared with actual measurement during experimental runs.

Processing of rubber and plastic wastes by conventional incineration could release toxic gases like dioxins and furans due to lower operating temperatures and hence not preferred [6,7]. Plasma-based incineration is considered as a source of high temperature ( $>1500$  K) which can effectively help in suppressing the formation of dioxins and furans [7-10]. Therefore, experiments with plasma torch as an intense heat source for preheating and waste decomposition are underway. Simulating existing incineration chamber is important before simulating plasma-based incineration chamber as, due to very high temperature gradients, simulations of plasma incineration chamber are expected to be computationally challenging. Also understanding of the temperature distribution in the existing diesel fired incineration chamber will lead to better insights into expected temperature distribution in plasma incineration chamber.

## System Description

The system studied is a typical diesel fired incinerator for management of radioactive cellulosic waste. The main component of the system is a combustion chamber. Diesel fired burner is used to preheat the chamber and then the waste box (containing cellulosic waste) is introduced inside the chamber for incineration in presence of adequate air supply. The chamber is a cuboidal geometry with cross-section of 1 m x 1 m. The 2D schematic image of the combustion chamber is shown in Fig. 1.

Pilot air and diesel are fed from a side nozzle in segregated mode, and mix while entering the chamber. At the entry of the diesel and air, ignition spark is provided for onset of combustion. Main air for waste combustion is fed from a side nozzle at the bottom. Waste is fed in a carton box. A thermocouple is used to track the progress of combustion process in the chamber by measuring the temperature.

The detailed inlet conditions of air and diesel are given in Table 1. Flow pattern inside the chamber, temperature of gaseous mixture in the chamber and the temperature of the surfaces of the

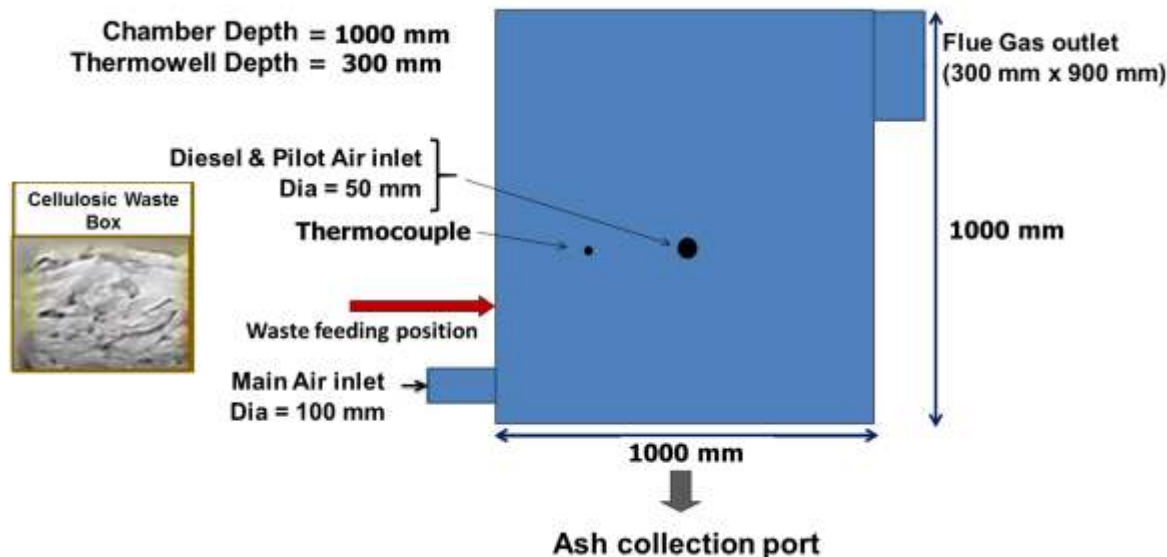


Fig.1: Schematic of primary chamber of incinerator setup

Table 1: Inlet conditions for diesel, pilot air and combustion air

	Air (For waste combustion)	Pilot Air (For diesel ignition)	Diesel
Flow rate	4 m <sup>3</sup> /min	0.8 m <sup>3</sup> /min	0.2 kg/min
Velocity	4 m/s	4 m/s	2 m/s
Temperature	300 K		
Pressure	100 kPa		

waste box are important parameters which affect cellulose combustion and rate of heat evolved during combustion.

### Reaction Kinetics:

Overall reactions of diesel and cellulose combustion are as given below [11]:

Diesel combustion:



Two-step cellulose combustion:

Step-1:



Step-2:



Eq. 1 is used for simulating the diesel reaction in the chamber. The cellulose combustion is two step reaction, in which step-1 is volatile formation by decomposition of cellulose and step-2 is combustion of volatile formed in step-1. However, in the model overall rate of combustion (Eq. 4) is used for simulating the surface reaction of the waste box. For estimating the combustion rate, order of reaction is taken as first order with respect to O<sub>2</sub> concentration and zeroth order with respect to cellulose

concentration (cellulose in excess at the surface). To estimate the local surface reaction rate and corresponding local heat generation rate, the surface temperature and local oxygen concentration are used. The kinetic data in literature [11] suggests that, the decomposition reaction is very fast for the temperature greater than 673 K, fast for temperature range of 573-673 K and slow if the temperature is less than 573 K. Further, if temperature is less than 473 K, hardly any decomposition takes place.

### Experimental study for cellulosic waste incineration

Actual low active cellulosic waste is incinerated in the incineration chamber (Fig. 1). Preheating of the chamber is done with diesel feed at 12 kg/h. The steady state temperature achieved in the chamber at the reference location, only with diesel combustion, is 573-673 K, which is adequate for onset of decomposition of cellulosic wastes [11]. Only after attaining the adequate steady state temperature, waste cellulosic feed is introduced in the form of a waste box. Combustion of cellulose provides additional heat to the chamber leading to further increase in the temperature. After sometime, temperature starts reducing which indicates that combustion is subsiding due to significant reduction in the combustible mass. At this time, a new box is fed for continuation of combustion and heat addition for sustaining the temperature in the chamber. The two-stage combustion phenomena, volatilization on box surface and oxidation nearby the surface of the box, observed during combustion of box in the chamber is shown in Fig. 2.

### Simulations

The present study involves the simulation of diesel fired incinerator for a specific geometry using COMSOL Multiphysics software. The model solves turbulent flow (using standard k-ε model) coupled with heat transfer and reactions. The governing equations solved include continuity equation, momentum equation, energy equation, species transport equation, and equations of k-ε model of turbulence. The simulation procedure is benchmarked for the combustion studies using Sandia Flame D experimental results [12]. Geometry used for validation is shown in Fig. 3 (a).

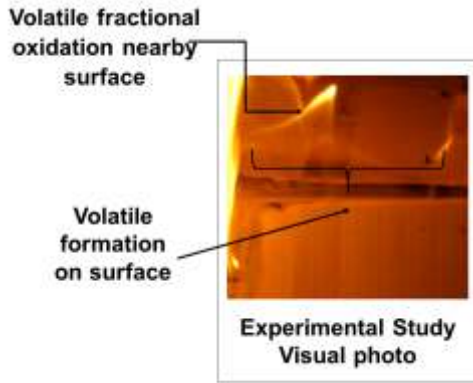


Fig.2: Photograph of waste box processing in combustion chamber

Sandia Flame D is a turbulent piloted methane jet flame and provides a standard and high-quality reference data set for validation of turbulent flame calculations. The experimental setup consists of central main jet surrounded by a pilot jet and a slow co-flow of air outside. The hot mixture from the pilot jet, besides stabilising the main jet, is also responsible for igniting the fuel which is injected from the main jet.

The simulation uses standard  $k-\epsilon$  model for turbulence modelling, reacting flow with turbulence chemistry interaction and energy transport equations. The simulation results need to be independent of the grid resolution. This is verified by running simulations with higher resolution grids. Adequate grid resolution is provided near the jet axis and close to the burner where gradients are expected to be large.

Dirichlet boundary condition is prescribed at the inlets for all variables i.e. velocity, temperature and species mass fractions. At the chamber walls, no-slip, insulated wall and zero-flux boundary conditions are used for momentum, energy transport and species

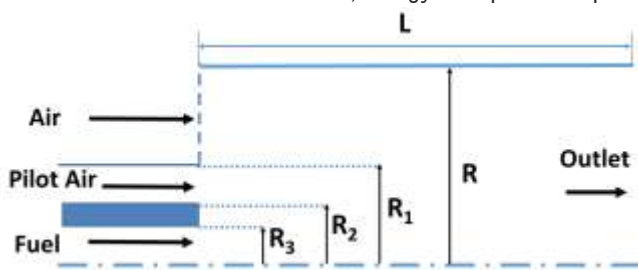
transport, respectively. At the surface of the waste box, no-slip condition along with species flux and heat flux due to surface reaction are specified. Pressure outlet and outflow boundary conditions (zero concentration and temperature gradients) are specified at the outlet. As observed in Fig. 3(b), predicted results are in good agreement with the experimental results of Sandia D Flame with minor under-prediction or over-prediction of product species.

After validation of the CFD model with literature data, the CFD analysis was taken up for the incineration chamber. The complexity of the system requires transient multiphysics (coupled solution of momentum transport, energy transport, species transport along with an appropriate model of turbulence) 3D simulation. During the course of processing, the waste box shrinks as it undergoes combustion. This should also be accounted in the CFD model. However, a CFD model incorporating complete physics will be too complex. Due to the complexities involved, in the first-step of CFD model development, a CFD model with certain assumptions has been developed and reported in this study. The model will be gradually taken forward by incorporating more complexities to realistically simulate the actual system.

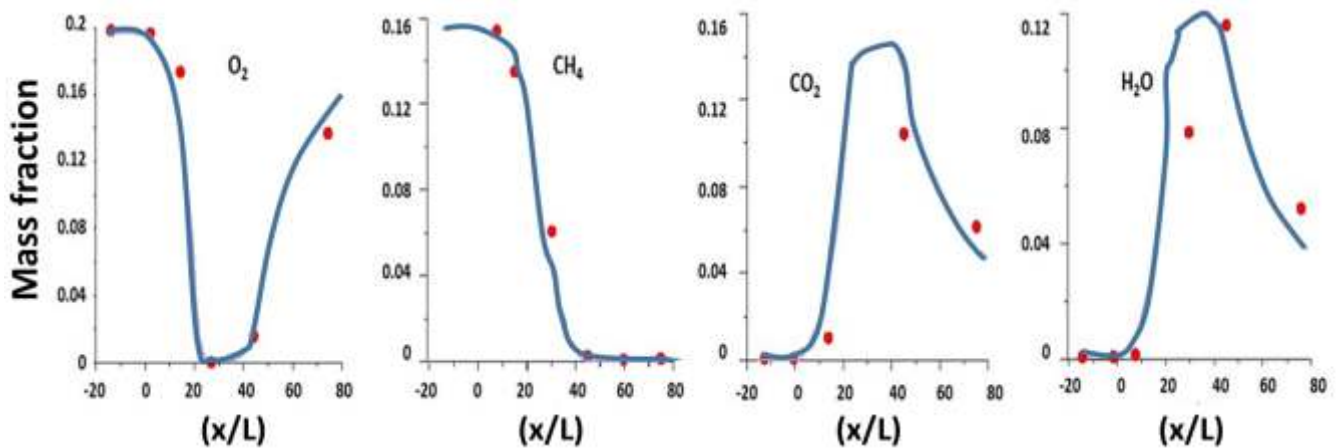
A 2D geometry has been considered for the simulation. The geometry and meshed computational domain are shown in Fig. 4. There are five sub-components in the system, i.e. main incineration chamber, fuel and pilot air inlet nozzles, air supply nozzle, outlet of the flue gases and waste box. Mass feed rate of diesel and air have been kept the same as in the actual plant conditions.

Following assumption are used while carrying out the CFD simulations:

1. 2D CFD steady state simulation is performed maintaining the geometric and kinetic similarity.
2. Walls of the chamber are assumed to be perfectly insulated with no heat loss. Only heat loss from the system is through the outgoing flue gases.
3. Combustion of waste box is considered as the surface reaction. No bulk reaction is simulated for the waste box. Overall combustion reaction as given in Eq. 4 is used.



(a) Geometry used for validation of simulation methodology



— CFD study results      ● Results of bench marking reference

(b) Comparison of predicted and experimental mass fraction profiles

Fig.3: Validation of the CFD model using Sandia Flame D experimental results ( $x/L$ : relative axial position)

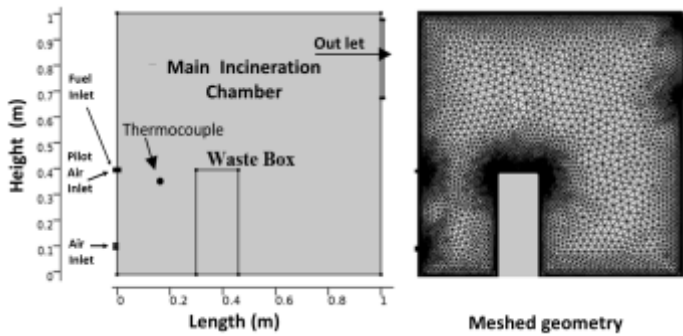


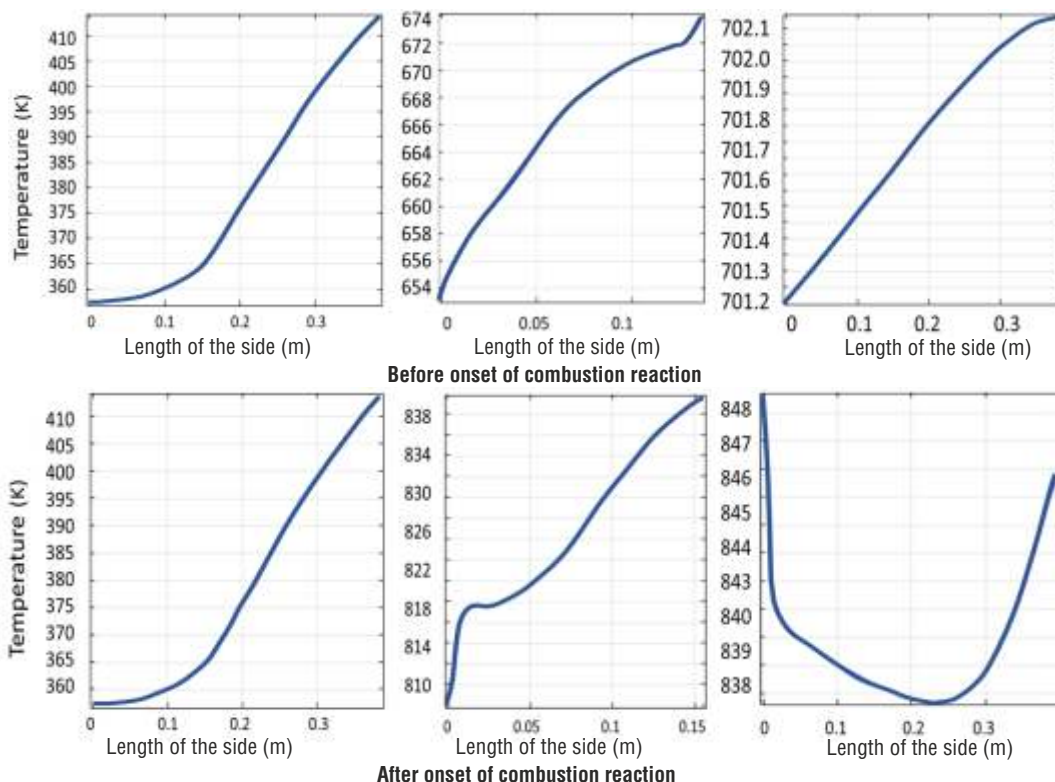
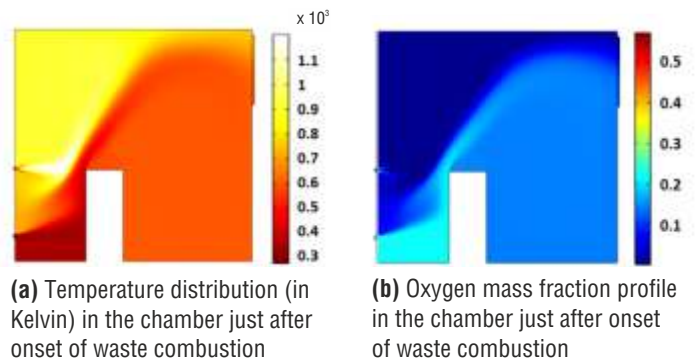
**Fig.4:** Typical geometry for CFD simulation and meshed computational domain

4. Size of the waste box is considered to remain same while the surface reactions at the edges of the waste box continue.
5. Turbulent mixing model has been assumed for diesel combustion as the reaction is spontaneous once favourable temperature is achieved.

The simulations are carried out in phase-wise manner. Initially, flow patterns of diesel (vapor phase) and air are simulated. The results of this simulation are taken as initial solution for simultaneous solution of flow and diesel combustion to estimate the temperature and species distribution in the chamber. These results are then used as the initial conditions to simultaneously solve flow, diesel reaction and waste box combustion reaction. This methodology of solution is opted to ensure convergence. Typical spatial distribution of temperature and oxygen inside the chamber as predicted by the simulation just after the onset of box processing are shown in Fig. 5(a) and (b), respectively. Temperature profiles on the three faces of the box are shown in Fig. 5(c) for two different conditions, i.e. before onset of the surface reaction and after onset of the surface reaction.

As observed from Fig. 5(a) and 5(b), very high temperature ( $> 1273$  K) and lowest concentration of oxygen are observed in top left corner of the chamber. This is due to rising hot gaseous mixture depleted in oxygen concentration generated in the combustion of diesel. In fact, as is clearly evident from Fig. 5 (a), the maximum temperature in the chamber is observed in the diesel jet. Temperature observed at the front face of the waste box is lower ( $< 423$  K) because of its direct exposure to the room temperature combustion air coming into the chamber, resulting into blanketing effect. Thus, reaction is slow along the front face and so is the consumption of oxygen resulting in higher oxygen concentration in the vicinity of the front face. The top and back faces are not directly swept by the incoming air at room temperature and hence temperatures are higher at these faces (654-702 K), which leads to faster reaction which in turn leads to reduced oxygen concentration in the vicinity of these faces.

The front face sees average temperature less than 423 K throughout the process, hence even though higher concentration of oxygen is present lower temperature causes very slow decomposition at the front face compared to decomposition at other two faces which have higher temperatures. Temperatures at top and back side faces are more than 800 K during waste



**(c)** Predicted temperature profiles (in Kelvin) on the surface of the waste box before and after onset of decomposition

**Fig.5:** Concentration and temperature profiles obtained from simulation

processing, i.e. after onset of waste combustion, giving favourable condition for further decomposition and incineration of the waste box.

The comparison of the experimental and predicted temperatures at the reference location, after the onset of decomposition reaction, was also done. The values are found to be 825 K and 840 K, respectively, showing a reasonably good match despite the several assumptions involved in the CFD model.

## Conclusions

The study reports a CFD model of a diesel-fired incineration chamber used for radioactive waste processing. The CFD model has been bench-marked with the reported data of Sandia Flame D experiments. The developed model is used to gain an understanding of distribution of temperature and chemical species involved in the reaction inside the incinerator chamber. The visual observation, during waste processing in experimental run, confirm the two-stage combustion phenomenon i.e. volatilization on box surface and oxidation nearby the surface of the box. Simulation result shows that the front face of the waste box sees more oxygen concentration compared to the top and back faces. Results also show that for both before and after onset of waste combustion the front face of the box has lower temperature (<423 K), compared to other two faces (>650 K), due to cooling effect of combustion air. The temperature at the front face is very low to initiate effective combustion reaction. Hence, combustion is predominantly occurs on the top and back side faces of the waste box kept in the chamber. The temperature predicted by simulation compares well with measured temperature at a reference location during an experimental run.

The reported CFD model provides useful insights into the temperature and concentration distributions inside the chamber and will be useful for further model development to understand inherently complex process of incineration. The results of the present study will also form reference data of temperature and concentration distributions in the incinerator chamber for a similar study with plasma-based system planned for combustible waste forms.

## Acknowledgement:

Authors acknowledge with gratitude constant encouragement of K. Agarwal and P.K. Wattal (former Directors of NRG, BARC) as well as K. Banerjee (former Associate Director, NRG, BARC). Authors convey heartfelt thanks to K.K. Singh (ChED) and his team for technical contribution towards successful CFD study. Authors thank all team members at SWM/WMD towards contribution in demonstration runs of the system.

## Corresponding author\*

K.C. Pancholi (keyur@barc.gov.in)

## References

- [1] L.P. Sant'ana and T. Cordeiro, "Management of radioactive waste: A review", in Proceedings of the International Academy of Ecology and Environmental Sciences, 2016, **6**, 38-43.
- [2] International Atomic Energy Agency (IAEA), General Safety Guide GSG-1, "Classification of radioactive waste", Vienna, 2009.
- [3] International Atomic Energy Agency (IAEA), Specific Safety Guide, SSG-40, "Predisposal management of radioactive waste from nuclear power plants and research reactors", Vienna, 2016.
- [4] K. Raj, K.K. Prasad and N.K. Bansal, "Radioactive waste management practices in India", *Nuclear Engineering and Design*, April, 2006, **236**, 7–8, 914-930.
- [5] P.K. Wattal, "Indian programme on radioactive waste management", *Indian Academy of Sciences*, October, 2013, **38**, Part 5, 849–857.
- [6] H. Fiedler, "Dioxins and furans (PCDD/PCDF)", *Persistent Organic Pollutants - The Handbook of Environmental Chemistry*, Springer, 2003, **3**, 123-201.
- [7] Incineration and Dioxins: Review of Formation Process, Consultancy report prepared by Environmental and Safety Services for Environment Australia, Commonwealth Department of the Environment and Heritage, Canberra, Available at: <https://www.environment.gov.au/protection/publications/incineration-and-dioxins-review-formation-processes-1999>.
- [8] International Atomic Energy Agency (IAEA), Tech Doc series no 1527, "Application of thermal technologies for processing of radioactive waste", Vienna, 2006.
- [9] E.S. Prado, F.S. Miranda, L.G. de Araujo, G. Petraconi and M.R. Baldan, "Thermal plasma technology for radioactive waste treatment: a review", *Journal of Radioanalytical and Nuclear Chemistry*, 2020, 1-12.
- [10] S. Nema and K. Ganeshprasad, "Plasma pyrolysis of medical waste", *Current Science*, 2002, 271-278.
- [11] A.L. Sullivan and R. Ball, "Thermal decomposition and combustion chemistry of cellulosic biomass", *Journal of Atmospheric Environment*, 2012, **47**, 133-141.
- [12] A. Kadar, "Modeling turbulent non-premixed combustion in industrial furnaces using the open source toolbox OpenFOAM (MS thesis)", Delft University of Technology, Netherlands, 2015.

# Synthesis of carbon nanotube aerogel by chemical vapour deposition - A CFD Study

Amit Kaushal<sup>1,2\*</sup>, Rajath Alexander<sup>1,2</sup>, P.T. Rao<sup>1</sup>, Jyoti Prakash<sup>1</sup>, Kinshuk Dasgupta<sup>1,2</sup>

<sup>1</sup>Glass and Advanced Materials Division

Bhabha Atomic Research Centre, Trombay, Mumbai-400085, India

<sup>2</sup>Homi Bhabha National Institute, Anushaktinagar, Mumbai-400094, India

## ABSTRACT

Carbon nanotubes (CNTs) and various carbon nanostructures (0D, 1D, 2D and 3D) are gaining importance in material research due to their unique properties owing to nano dimensions. Chemical vapour deposition (CVD) process is found to be one of the economic ways to produce these structures in large quantities and thus capable of fulfilling the future demand. Providing a wide range of operating window suitable to produce property specific customised material is the special attraction of the CVD process. Despite various advantages, lower conversion of the precursor and catalyst remain the greatest challenge associated with this process. Predicting the flow pattern and temperature profile inside a CVD reactor are important steps to enhance process efficiency. In this work computational fluid dynamics (CFD) analysis is carried out to analyse flow dynamics inside a CVD reactor. The deviation from plug flow behaviour due to recirculation of incoming gas is found to be correlated with diameter and thus properties of the synthesized CNTs. Catalyst agglomeration, the prime contributor of large diameter CNTs, can be prevented by selecting suitable flow and temperature conditions inside the reactor. Knowledge of location of decomposition of all the precursors is the key to control the size of CNTs as different precursors decompose at different temperatures. Recirculation tendency has also been investigated and compared at various carrier flow for argon and hydrogen as carrier gases. Narrow distribution of diameter is observed using hydrogen as a carrier and correlated with no recirculation inside the heating zone while use of argon provides wider diameter distribution due to decomposition of thiophene and its recirculation in heating zone.

**Keywords:** Carbon Nanotube, Chemical Vapour Deposition, Computational Fluid Dynamics

## Introduction

Carbon nanotube (CNT) finds application in the field of nano-electronics, nano-medicine, nano-sensors, high strength and low-density composites, energy storage solutions, stealth technology and others due to very high thermal & electrical conductivities, high tensile strength, high modulus of elasticity, low density, high specific surface area, chemical stability, and high aspect ratio. Some of the novel applications include high

strength composites, EMI shielding, supercapacitor, battery electrodes, green catalysis, efficient drug delivery and biosensors, energy storage and energy conversion devices, transparent conducting films, field emission display, highly porous membrane, thermal interface, electrical interconnect, etc. [1,2] It is also highly demanded for used in materials of sustainable future and green technologies. CNTs can be synthesized by various methods. However, being continuous process and low-cost operation, chemical vapour deposition (CVD) has many advantages over other methods like laser ablation, arc discharge and is capable to produce CNTs in large quantity [2-4]. In the present CVD process, carbon precursor is allowed to decompose in presence of a catalyst in a tubular reactor in continuous mode to produce CNTs of various shape and size. There are flexibilities with respect to selection of catalyst (transition metal single or bimetallic) and carbon precursor (liquid or gaseous hydrocarbon feed), reactor operating conditions along with addition of growth promoter and reaction controlling agent like oxygen containing compound, which lead to evolution of various useful carbon nano structures like single-walled carbon nanotube (SWCNT), multi-walled carbon nanotube (MWCNT), CNT aerogel, CNT fibre, carbon nano dots and doped CNT. In this way, CVD process provides an ability to produce customised carbon nano materials of desired properties for the given purpose with greater control. Nano-electronics, sensor development and other applications require production of CNTs with enhanced control as electronic properties are very sensitive to CNT diameter and internal structures. CFD study is required to correlate the diameter of CNT produced in a CVD reactor with various operating conditions. Various CFD work reported in literature were focused on predicting growth rate of CNT and ferrocene decomposition in the temperature range of 800-1000K [5-7], which is not suitable for synthesis of CNT aerogel. Recirculation of carrier gas at the inlet and the outlet of heating zone plays important role in deciding the product quality for synthesis of CNT aerogel and it has been predicted by various researchers [8-10]. However, the location and degree of recirculation have not been quantified and reported in a scientific manner so far for the synthesis of CNTs. Hou *et al.* [10] have shown that recirculation at the outlet helps in stable sock formation which is required for direct spinning of CNT aerogel to produce fibre. This recirculation decreases with increase in the flow rate and spinning ability vanishes above a flow rate of 3200 standard cubic centimetre per minute (SCCM). The reduction in specific strength of CNT fibre due to recirculation has been shown by Oh *et al.* [8]. They found the effect of recirculation

in a 70 mm diameter quartz tube reactor operating at 1200°C but no recirculation is observed in alumina tube reactor of the same dimension. Lee *et.al* [9] found the recirculation at 3200 SCCM flow rate in 50 mm diameter alumina tube reactor at 1250°C and observed increase in specific strength with reduction in recirculating behaviour. The impact of recirculating flow has also not been evaluated in great detail. In this work we used COMSOL Multiphysics 5.5 for flow and temperature analysis inside the reactor to predict the recirculation at various operating conditions. Flow and temperature profiles have been generated in order to get the idea of thermal decomposition timeline. These plots have been used as a strategy input for controlling CNT diameter by providing a sulphur coating on catalyst particles before start of catalyst agglomeration. Grashoff number and Rayleigh number have been plotted along the length of the reactor in order to provide a qualitative analysis of recirculation. The properties of CNTs synthesized in different conditions have been compared to find out the effect of recirculation on diameter. Recirculation has also been compared at different carrier flow conditions. A mixture of argon and hydrogen has been used as a carrier flow in order to get advantage of lower recirculation in presence of hydrogen due to lower molecular mass while maintain a reducing environment for better yield.

## Materials & Methods

### CNT synthesis process:

CNTs in this work has been synthesized by floating catalyst chemical vapor deposition (FC-CVD) process in a horizontal tubular reactor (40mm ID, Alumina) shown in Fig.1. Ethanol, ferrocene and thiophene have been used as precursors for carbon, catalyst and sulfur promoter, respectively. Liquid feed (1 weight percent ferrocene and 0.5 weight percentage thiophene mixed in 80ml ethanol) is pumped to the preheater zone maintained at 200°C and is allowed to be carried in the main furnace with a carrier flow (mixture of argon and hydrogen) of 1-3 lpm. Reaction took place in the main furnace maintained at 1250°C temperature where CNT aerogel was produced through catalytic cracking of carbon precursor in presence of catalyst. CNT produced in the form of spinnable sock along with other gaseous product was continuously drawn in a harvest box. Gaseous product was diluted through supply of excess inert gas (argon) in the harvest box in order to prevent any fire related hazard.

CNT synthesized was characterised by Raman spectroscopy, scanning electron microscope and thermogravimetric analysis. Raman spectra of the synthesized

SWCNT was obtained using a WITec alpha 300R polarized Raman instrument with a laser wavelength of 514 nm and a 50X objective lens. RBM peak position (characteristics feature of SWCNT) has been used to calculate the diameter as per Eq. (1).

$$\omega_{\text{RBM}} = \frac{233}{d} + 10 \quad (1)$$

Structural analysis of the synthesized material was carried using field emission scanning electron microscope (Model-SIGMA, Carl Zeiss, Germany) at 5 kV accelerating voltage using In-lens Detector. Thermal analysis of the synthesized sample was carried out using Thermal Gravimetric Analyzer (TGA) (Setaram TGA 1600, France). The mass change and its corresponding temperature range were used for the quantification of CNT, amorphous carbon and catalyst present in the sample.

### CFD study

To understand the flow condition in the FC-CVD reactor, we used computational fluid dynamics modelling to solve the continuity, momentum and energy equation in the reactor. Numerical simulation was carried out using COMSOL Multiphysics (COMSOL, Inc.). The continuity, momentum and energy equations are shown in Eqs. (2-5)

$$\nabla \cdot \rho \mathbf{u} = 0 \quad (2)$$

$$\rho(\mathbf{u} \cdot \nabla) \mathbf{u} = \nabla \cdot [-p\mathbf{I} + \mu(\nabla \mathbf{u} + (\nabla \mathbf{u})^T)] + \mathbf{F}_g \quad (3)$$

$$\rho C_p (\mathbf{u} \cdot \nabla) T = \nabla \cdot (k \nabla T) + W_p \quad (4)$$

$$\mathbf{n} \cdot \mathbf{q} = \varepsilon \sigma (T^4 - T_s^4) \quad (5)$$

$\rho$  [g/cm<sup>3</sup>] is the density of the gas,  $\mathbf{u}$  [m/s] is the velocity field of the gas,  $p$  [kg/(m·s<sup>2</sup>)] is the fluid pressure,  $\mu$  [kg/(m·s)] is the viscosity of the gas,  $C_p$  [J/(K·kg)] is the thermal capacity of the gas,  $k$  [W/(m·K)] is the thermal conductivity of the gas,  $T$  [K] is the gas temperature,  $\mathbf{F}_g$  [kg/(m<sup>2</sup>·s<sup>2</sup>)] is the body force due to gravity.  $W_p$  [kg/(m<sup>2</sup>·s<sup>2</sup>)] is the pressure work induced by density variation.  $\mathbf{q}$  [W/m<sup>2</sup>] is the net radiative heat flux through a heated surface.  $\varepsilon$  [m<sup>2</sup>] is emissivity of surface,  $T_s$  is temperature of the heated surface and  $\sigma$  [J/s/m<sup>2</sup>/K<sup>4</sup>] = 5.67x10<sup>-8</sup> is Stefan-Boltzmann constant.

A 3-D, steady-state, non-isothermal laminar flow model was used for study. The low-Mach-number formulation has been used to account for density variations. Radiative heat transfer in the reactor has been incorporated using 'Hemicube' model available

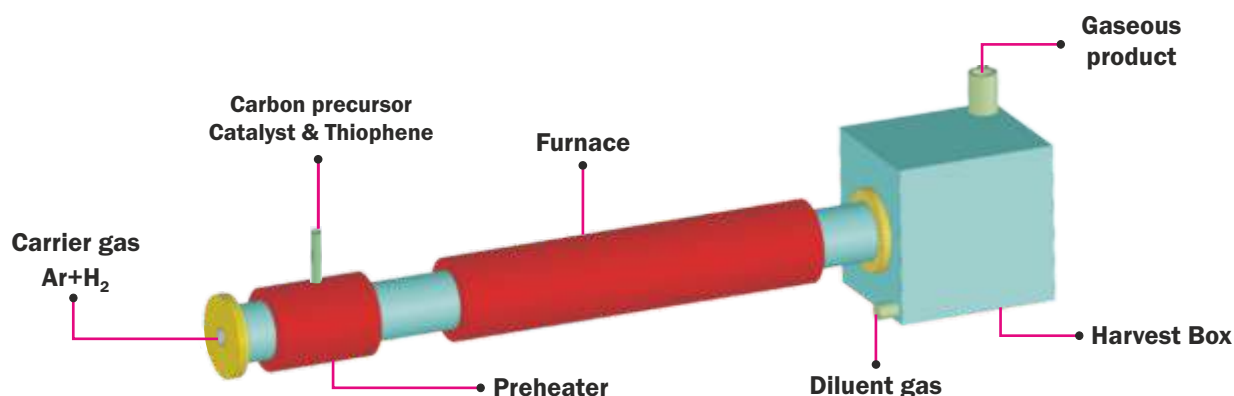


Fig.1: Schematic of floating catalyst chemical vapour deposition system for CNT aerogel synthesis

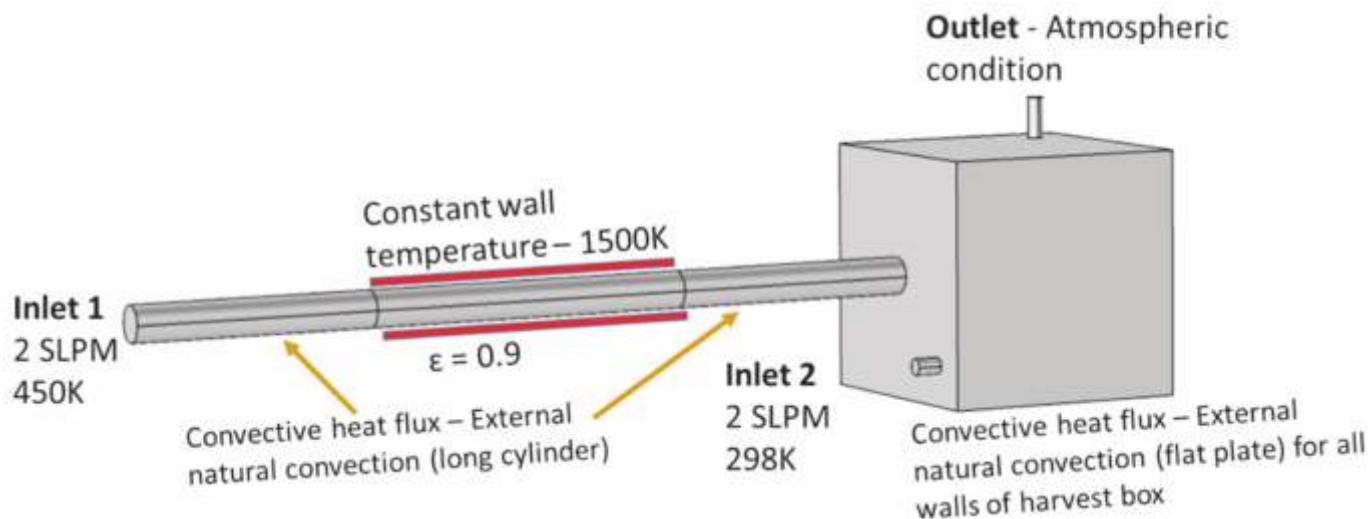


Fig.2: Computational domain along with boundary conditions

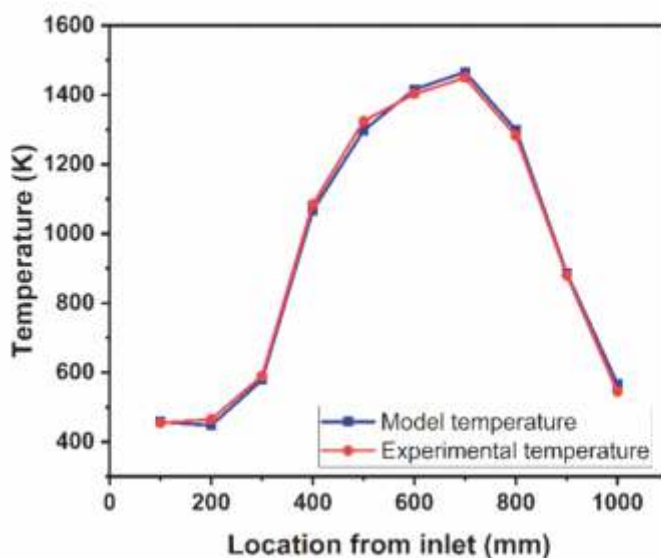


Fig.3: Comparison of experimentally measured temperature profile with model predicted temperature profile

in COMSOL Multiphysics. Boundary conditions along with computational domain over which conservation equations were solved are shown in Fig.2. Discretization was carried out using physics controlled meshing option available in COMSOL Multiphysics where 116633 domain elements, 11286 boundary elements, and 816 edge elements were used for entire domain. To verify the simulation model, the numerical results were compared with the temperature distribution inside the reactor heated at experimental condition with argon flow and without precursor flow using external thermocouple and readout box (shown in Fig.3)

### Results and discussion

CNT aerogel is self-agglomerated long CNT produced at higher temperatures (>1200°C) in CVD furnace as compared to powder CNT which consist of mainly short length CNTs. CNT fibre can easily be produced by direct spinning of CNT aerogel on continuous basis in FC-CVD furnace. Properties of fibre produced are highly dependent on length of constituent CNT which is very

sensitive to amount and size of the catalyst used. Catalyst particle grows in size with increase in temperature along the axial direction due to agglomeration. It is found that larger size of catalyst yields MWCNT while smaller size catalyst yields SWCNT. In addition to this, a critical amount of catalyst is also required to produce SWCNT/MWCNT. It is very difficult to maintain smaller size of catalyst above this critical mass requirement but can be possible by providing a sulphur coating as soon as catalyst starts nucleating [11]. Ferrocene (catalyst precursor) decomposition and nucleation of iron particle start at about 550°C temperature, while thiophene (sulphur precursor) decomposition starts at 850°C [12]. Hence, local flow and temperature conditions inside the reactor are very critical to prevent agglomeration and thus controlling the diameter of CNT, which is predicted using CFD simulations. Fluid flow streamlines along with temperature surface are generated and shown in Fig.4 (a, b and c). It is observed that a recirculation cell is formed just before the high temperature zone of the reactor and extends inside the reactor (indicated in the left box in Fig. 4 c).



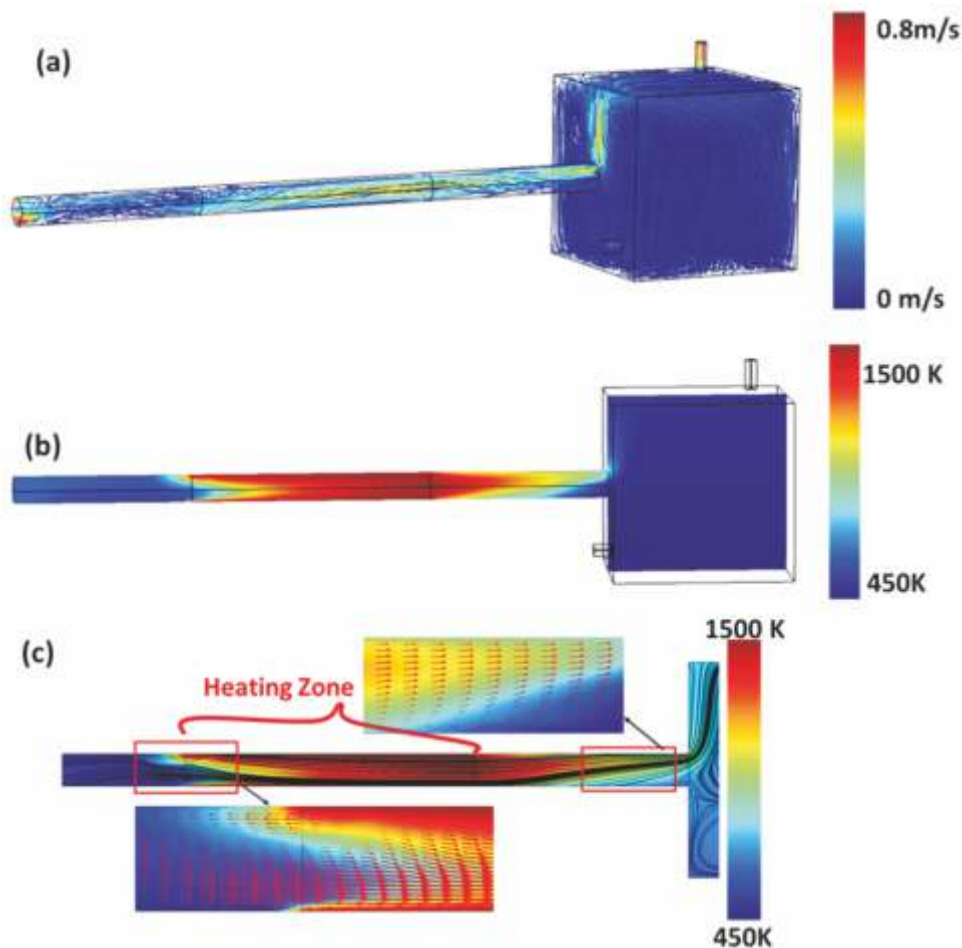


**Fig.4:** (a) Streamlines with velocity magnitude represented by colour code (b) temperature profile in central 2D plane and (c) flow field represented by streamlines overlying on the temperature contour showing recirculation at the inlet and the outlet of heating zone in case of pure argon flow

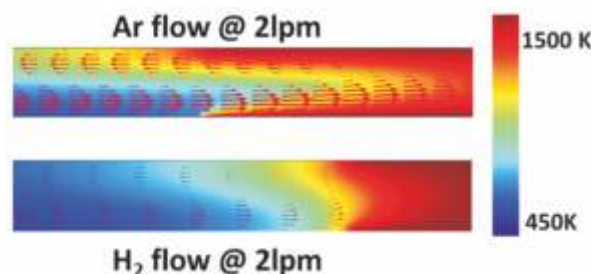


**Fig.5:** Velocity vectors overlying on the temperature contour for argon and hydrogen used as carrier showing recirculation penetrating deeper inside the heating zone in case of argon

### Effect of carrier gas on recirculation and CNT aerogel

CNT starts growing once the feed mixture reaches yellow and red colour region, corresponding to start and end of thermal decomposition of thiophene (Fig.4 and 5). In high temperature zone, catalyst particle starts nucleating and CNT grows. If recirculation penetrates the heating zone, some of nucleated catalyst particles come out of high temperature zone and growth of CNT terminates as reaction mixture goes to the lower temperature region. In this way recirculation in heating zone causes the formation of short length CNT which ultimately reduces the product uniformity and thus property of CNT aerogel. Length and position of this recirculation can be controlled by adjusting flow rate and composition of feed. Fig.5 shows recirculation cell extended deep inside the reactor when only

argon is used as carrier gas while it is formed outside the heating zone if only hydrogen is used as carrier gas. Recirculation outside heating zone does not contain nucleated catalyst particle and there is no chance of CNT growth in recirculating stream. Higher fraction of feed is converted into short length CNT if recirculation cell extended deep inside the reactor. Thus, pure hydrogen as a carrier produces CNT aerogel with more uniform length and diameter as CNT grows only in high temperature zone. While a mixture of short and large length CNT can be found and the uniformity of product reduces significantly as CNT grows in two different regions (recirculation stream and high temperature zone) when pure argon is used as carrier gas. The diameter of CNT is also found to be affected by carrier gas flow and the location of recirculation. Diameter distribution of CNT aerogel produced

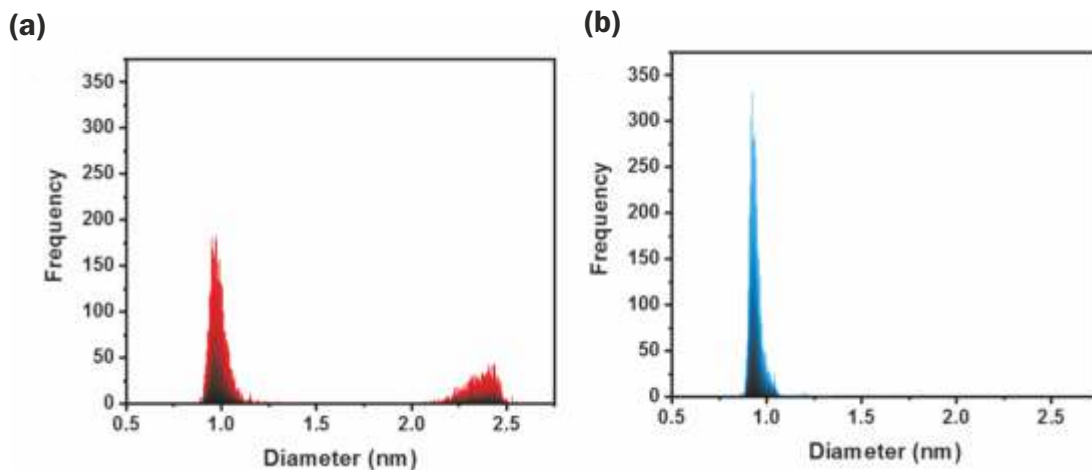


**Fig.6:** Diameter distribution in the CNT aerogel sample using (a) argon and (b) hydrogen as a carrier gas (calculated using RBM peak position observed in Raman spectrum)

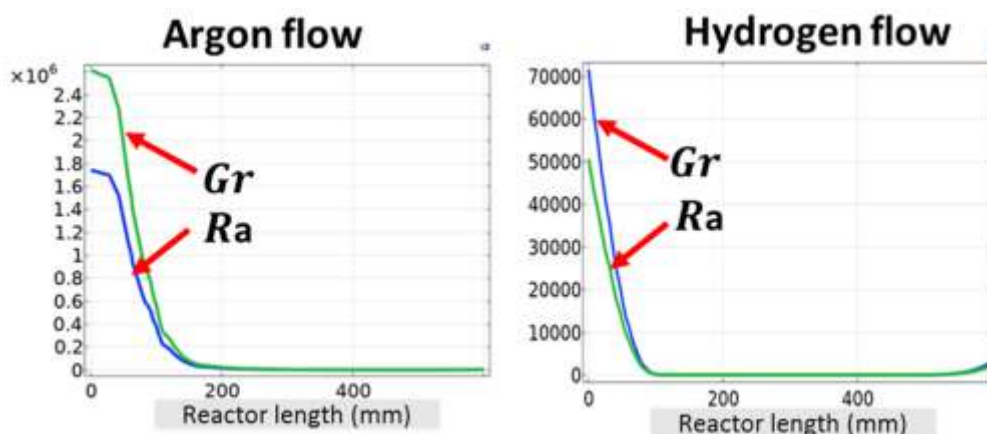


**Fig.7:** Grashoff and Rayleigh numbers plotted along the reactor length (starting from 100 mm before the heating zone)

using hydrogen and argon as a carrier gas is shown in Fig. 6. RBM peak position in Raman spectra of these two samples were used to calculate diameter according to formulae given in Eq. (1).

### Effect of flow rate on recirculation and CNT aerogel

Grashoff number ( $Gr$ ) and Rayleigh number ( $Ra$ ) are defined as given by Eq. 6 and 7, respectively. The plot of these numbers for argon and hydrogen flow along the length of reactor (starting from 100 mm before heating zone) are shown in Fig.7. Higher values of  $Gr$  and  $Ra$  indicate the significance of buoyancy effect which causes recirculation. In this way the location of recirculation can be predicted by these numbers. Higher values of  $Gr$  and  $Ra$  ( $>10^4$ ) are found only in first 100 mm which reduce to a very low value indicating no recirculation in heating zone in case of hydrogen. But in case of argon these values are much higher as compared to hydrogen and also extended beyond 100 mm, meaning there exists a recirculation current penetrating deeper into the heating zone.

$$Gr = \frac{g \cdot \beta \cdot \Delta T \cdot D^3}{\nu^2} \quad (6)$$

$$Ra = Gr \cdot Pr \quad (7)$$

$\beta$  is expansion coefficient,  $D$  is the diameter of reactor and  $\nu$  is kinematic viscosity of carrier gas.

The strength and location of recirculation at 2 lpm flow rate has been shown in Fig.8 for argon flow and hydrogen flow while at various flow rate of argon in Fig.9. It is found that recirculation reduces and shift in position with increase in flow velocity of carrier gas. Higher flow velocity have been achieved by using hydrogen as a carrier gas in place of argon (Fig.8) and increasing the total flow rate of argon gas (Fig.9). The retreat of recirculation at high flow velocity is attributed to increase in Peclet number (a dimensionless number defined as ratio of advective transport to diffusive transport of heat or momentum). Lower amount of short length CNT is produced at higher carrier flow rate as the recirculation zone is outside the thermal cracking zone of thiophene but the carbon conversion also decreases due to reduction in residence time. Fig.10(a) shows that RBM peak position changes with increase in argon flow rate and smaller diameter CNT is synthesized at higher flow rate. Fig.10 (b1 & b2) shows SEM images of CNT aerogel synthesized using hydrogen and argon flow, respectively. Hence, an optimum flow condition for feed (composition and flow rate) is required to be worked out for synthesis of high purity and uniform diameter CNT aerogel for continuous spinning of CNT fibre.

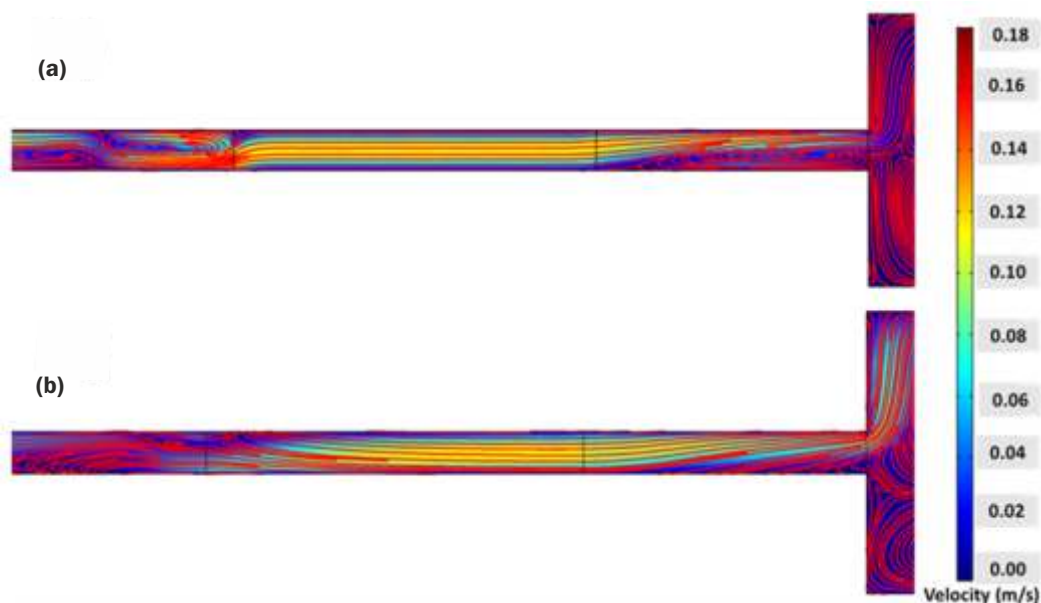


**Fig.8:** Flow field represented by streamlines over the velocity contour (colour map) showing recirculation at inlet and outlet of heating zone for (a) hydrogen and (b) argon flow

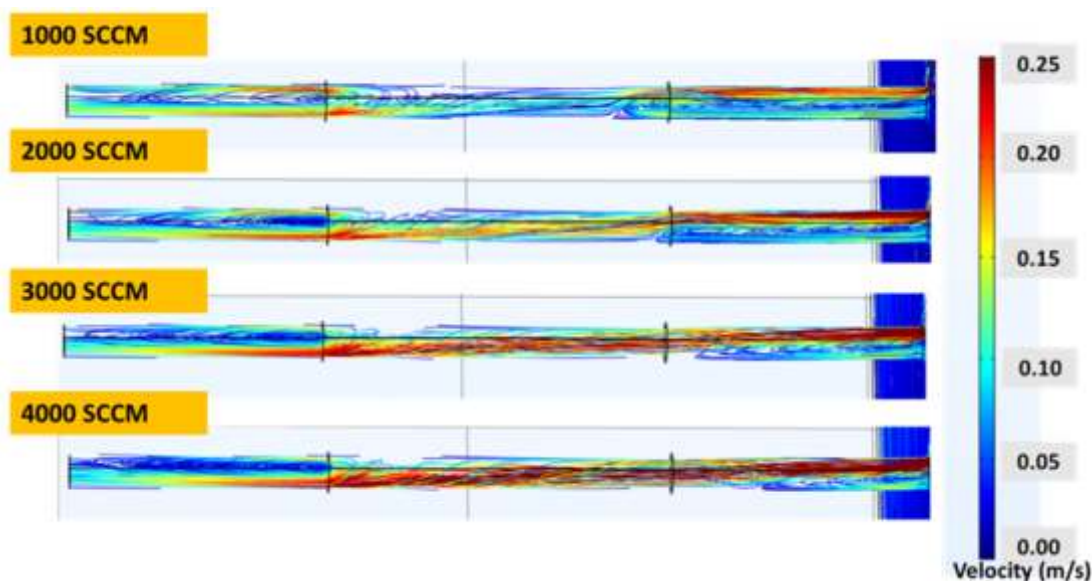


**Fig.9:** Streamline (colour representing the magnitude of flow velocity) showing the effect of argon flow rate on recirculation at inlet and outlet of heating zone

## Conclusion

- CFD analysis has been used to demonstrate the effect of flow and temperature conditions inside the reactor on the diameter distribution of CNTs in aerogel produced by FC-CVD process.
- The quality and properties of CNT aerogel synthesized in this process are affected by the location of recirculation in the flow field which is highly correlated with the selection of carrier gas and its flow rate.

- The recirculation penetrating deep inside the heating zone (in case of argon used as a carrier) provides a second zone of CNT growth where relatively lower size of CNT is produced.
- Recirculation decreases with increase in Peclet number due to reduction in diffusion transport as compared to advective transport of heat and momentum.

## Corresponding author\*

Amit Kaushal (akaushal@barc.gov.in)

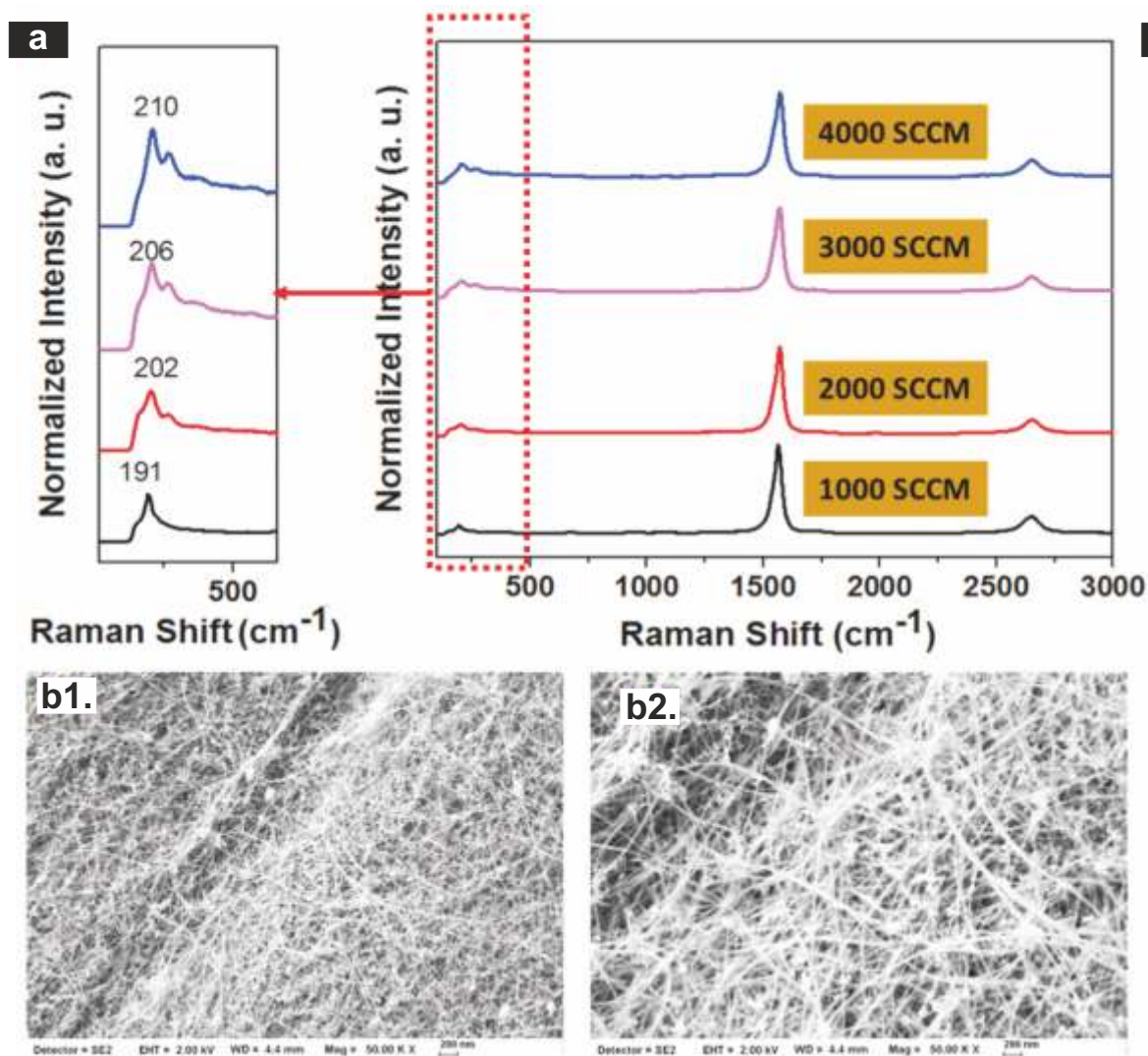


**Fig.10:** (a) Raman spectrum of CNT aerogel at different argon flow rate and (b) SEM images of CNT aerogel for hydrogen (b1) and argon (b2) used as a carrier flow

## References

- [1] M.F.L. De Volder, *et al.*, Carbon Nanotubes: Present and Future Commercial Applications. *Science*, 2013, **339**(6119), 535.
- [2] E. Dervishi, *et al.*, Carbon Nanotubes: Synthesis, Properties, and Applications. *Particulate Science and Technology*, 2009, **27**(2), 107-125.
- [3] K. Dasgupta, *et al.*, Fluidized bed synthesis of carbon nanotubes – A review. *Chemical Engineering Journal*, 2011, **171**(3), 841-869.
- [4] K. Dasgupta, *et al.*, Fluidized bed synthesis of carbon nanotubes: Reaction mechanism, rate controlling step and overall rate of reaction. *AIChE Journal*, 2014, **60**(8), 2882-2892.
- [5] H. Endo, *et al.*, CFD prediction of carbon nanotube production rate in a CVD reactor. *Chemical Physics Letters*, 2004, **387**(4), 307-311.
- [6] K. Kuwana, *et al.*, Catalyst deactivation in CVD synthesis of carbon nanotubes. *Carbon*, 2005, **43**(2), 253-260.
- [7] L., Samandari-Masouleh, *et al.*, Modeling the Growth of Carbon Nanotubes in a Floating Catalyst Reactor. *Industrial & Engineering Chemistry Research*, 2012, **51**(3), 1143-1149.
- [8] E. Oh, *et al.*, Super-strong carbon nanotube fibers achieved by engineering gas flow and postsynthesis treatment. *ACS Applied Materials & Interfaces*, 2020, **12**(11), 13107-13115.
- [9] S.-H. Lee, *et al.*, Deep-injection floating-catalyst chemical vapor deposition to continuously synthesize carbon nanotubes with high aspect ratio and high crystallinity. *Carbon*, 2021, **173**, 901-909.
- [10] G. Hou, *et al.*, Gas phase pyrolysis synthesis of carbon nanotubes at high temperature. *Materials & Design*, 2017, **132**, 112-118.
- [11] L. Weller, *et al.*, Mapping the parameter space for direct-spun carbon nanotube aerogels. *Carbon*, 2019, **146**, 789-812.
- [12] T.S. Gspann, *et al.*, Spinning of carbon nanotube fibres using the floating catalyst high temperature route: purity issues and the critical role of sulphur. *Faraday Discussions*, 2014, **173**, 47-65.

# Quantification of lead melting in a radioactive transport cask using CFD

Priyanshu Goyal\*, Vishnu Verma, Anu Dutta, J. Chattopadhyay

Reactor Safety Division

Bhabha Atomic Research Centre, Trombay, Mumbai-400085, India

## ABSTRACT

Shielded shipping casks are commonly used for the transportation of radioactive waste materials. Design approval of such a cask by the regulatory authority is subject to its demonstration of compliance with a thermal test, also known as fire test (among other tests). Lead shielding usually is provided for radiation protection. During cask transportation, an accident may cause fire, which may result in melting of lead provided for cask shielding. The molten lead may come out in case of mechanical seal failure resulting in shielding loss. Hence, cask has to maintain its structural integrity under normal and accidental (fire) conditions, and needs to be qualified with the prescribed code guidelines by the regulatory authorities. The present work reports a comprehensive CFD analysis of the thermal behaviour of lead melting for two different geometries (cylindrical and rectangular) considering natural convection in the melt. The study reveals a substantial influence of natural convection on the thermal state and melting behaviour of lead which may have a great bearing on the safety during transportation of cask.

**Keywords:** CFD, fire test, melting, natural convection, transport cask

## Introduction

A typical radioactive material transportation cask consists of a rectangular shaped box made of stainless-steel with an inner cavity to store the radioactive material for transportation. The inner cavity is encapsulated by lead sandwiched between two stainless steel liners. The lead provides the necessary shielding to minimize the radiation dose to the public domain. Design approval of such casks by the regulatory authority [1] is subject to its demonstration of compliance with a fire test (among other tests), which consists of exposure of the cask to hydrocarbon fuel/air fire on all sides with a flame temperature of about 800°C for a period of 30 minutes. During the fire test, the radiative flux from the fire is incident on the outer surface of the cask, which causes rapid heating of the various inner elements of the cask, and may cause melting of the shielding material i.e., lead. The melting of lead can cause loss of shielding capability due to relocation of molten lead in the lower region of

the cask, thus creating space in the top region. The molten lead may come out in case of mechanical seal failure due to high temperature and radiation dose may leak into the public domain. Therefore, it is of utmost importance to calculate the amount of lead melted during the fire test so as to assess the possible loss of shielding. The confirmation of design compliance mentioned above is generally shown by carrying out detailed steady-state and transient thermal analysis of the cask, which involves solving the basic transient 3-D conduction equation (ignoring natural convection) with the appropriate radiative and convective boundary conditions [2]. However, ignoring the natural (buoyancy driven) convection because of the density gradients in the molten pool of the lead may lead to a significant error in the predictions of both the extent of melting of lead and the pattern of melt front propagation during the transients. Not much literature is available on thermal analysis of transportation casks involving natural convection in the molten pool. This is due to the fact that numerical simulation of convective flow and heat transfer in the presence of phase change is a challenging task because the heat transfer is coupled with the turbulent flow field in 3D in a global domain where the pure solid and the pure liquid phases are separated by an ever-changing interface. At RSD, BARC, CFD analysis has been carried out for several transportation casks for the demonstration of their compliance with regulatory guidelines. The present article briefly describes the CFD analysis and the effect of natural convection phenomenon on thermal analysis of two different representative transportation casks.

## Geometries of selected shipping casks and test conditions

Two casks with different shape and size – one with a rectangular cross-section and the other with a cylindrical cross-section have been considered in the present analysis. Fig. 1 depicts the cross-section of the two casks.

Considering the symmetry axes in the rectangular and cylindrical cask, only sections of the entire cask were analyzed. For the rectangular cask, 3D analysis was done for the 1/4<sup>th</sup> section of the cask, retaining full vertical height to simulate the natural convection, which is a function of height. For the cylindrical cask, the axis is considered the symmetry axis. For the cylindrical cask, 2D axisymmetric case was analyzed.

Under normal storage conditions, the entire heat generated within the cask gets dissipated to the surroundings from its outer surface by natural convection and radiation mechanisms. Under

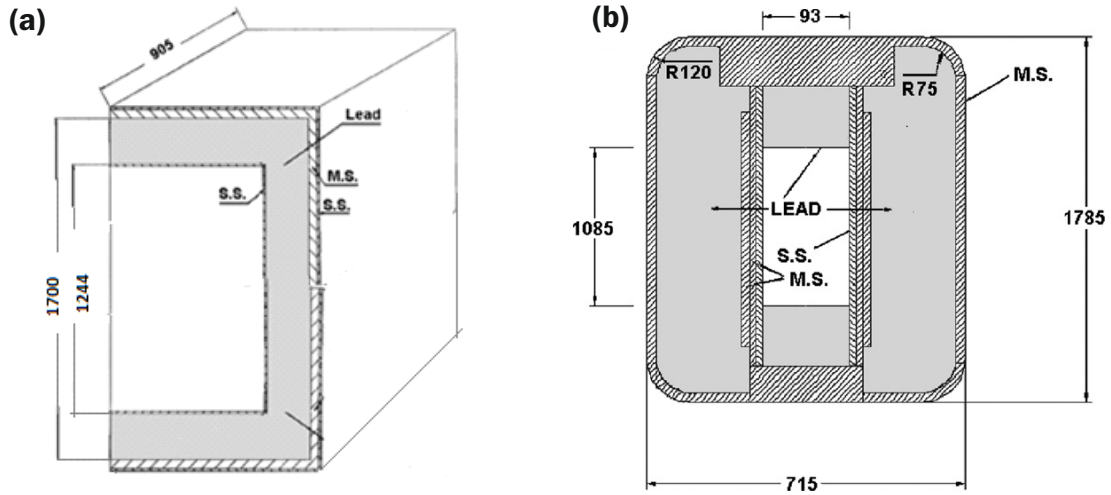


**Fig.1:** Sectional view of transportation cask (a) 1/4<sup>th</sup> section of rectangular cask (b) 1/2 section of cylindrical cask

the specified ambient conditions, the cask outer surface also receives solar radiation, which is dissipated to the surroundings. There is a possibility of melting of the lead layer in the annular region of the transport cask during an accidental fire. The regulatory guidelines stipulate that the fire test is to be carried out after the cask attains the steady-state in normal storage conditions. After the fire test, the analysis is continued with normal ambient conditions till the time temperature starts reducing in the cask. With this objective, the analysis was performed in three stages:

- Steady-state analysis
- Fire test analysis
- Post fire analysis

During transportation, the cask will be exposed to solar insolation and the values for the same are taken as per regulatory guidelines [1]. The heat generated within the over pack is specified as surface heat flux on the inner surface of the cask (for a typical case, heat generation of 456 W is taken for cylindrical cask and 7.4 kW for the rectangular cask). The heat generation is more in rectangular cask because of its larger Curie content compared to cylindrical cask. The emissivity of outer steel surface is taken as 0.3. The ambient temperature is specified as 42 °C. Convective heat transfer coefficient of 5W/m<sup>2</sup>K has been specified on the outer surface of the cask.

The steady state temperature distribution so obtained is used as initial temperature distribution for analyzing the transients during the fire test. During the fire test of 30 min duration, the radiative heat flux from the fire is incident on the outer walls, which will cause rapid heating of the various inner elements of the cask. Internal heat generation due to radioactive decay is same as in case of normal conditions. Ambient temperature of 800 °C, surface absorptivity of 0.8 and flame emissivity of 1.0 are specified for fire test condition. No solar heat flux is considered on the outer surface. Convective heat transfer coefficient on the outer surface typically recommended is 15 W/m<sup>2</sup>K which is based on a flue gas velocity of 10 m/s [1]. The temperature dependent thermophysical properties of various materials, such as, lead, mild steel (MS) and stainless steel (SS) are taken from literature [3].

## Numerical Modeling

The thermal analysis of cylindrical transport cask was carried out at RSD, BARC [4] using commercially available CFD code CFD-ACE+ [5], while the analysis of rectangular cask was carried out by Sanyal et al. at CGCRI, Kolkata (using CFD code FLUENT) under BRNS project with RSD [6]. At the time when the job was taken up, FLUENT already was capable of handling lead melting phenomenon through its inbuilt module. However, CFD-ACE+, at that time, had no inbuilt module to handle melting/solidification phenomenon directly. Therefore, with the help of user-subroutines, CFD-ACE+ was modified to model melting/solidification phenomenon.

The numerical model of the thermal transport in the cask and turbulent momentum transport of molten lead in the cask has been developed as a closely coupled set of transport equations for mass, energy and momentum along with turbulent fields, such as, turbulent kinetic energy and dissipation rate, using enthalpy porosity technique [7]. The set of governing equations in terms of primitive variables are as follows:

### Continuity:

$$\frac{\partial \rho}{\partial t} + \nabla \cdot (\rho \vec{v}) = 0 \quad (1)$$

### Momentum transport:

$$\frac{\partial \rho u}{\partial t} + \nabla \cdot (\rho \vec{v} u) = \nabla \cdot (\mu \nabla u) - \frac{\partial P}{\partial x} - Au + \tau_{turb} \quad (2)$$

$$\frac{\partial \rho v}{\partial t} + \nabla \cdot (\rho \vec{v} v) = \nabla \cdot (\mu \nabla v) - \frac{\partial P}{\partial y} - Av + \rho_{ref} g \beta \left( \frac{h - h_{ref}}{C_p} \right) + \tau_{turb} \quad (3)$$

$$\frac{\partial \rho w}{\partial t} + \nabla \cdot (\rho \vec{v} w) = \nabla \cdot (\mu \nabla w) - \frac{\partial P}{\partial z} - Aw + \tau_{turb} \quad (4)$$

$u, v, w$  are the velocity components in x, y and z directions, respectively.  $\vec{v}$  is the velocity vector,  $P$  is pressure,  $\mu$  is the viscosity,  $\rho$  is the density,  $\beta$  is thermal expansion coefficient and  $h_{ref}$  and  $\rho_{ref}$  are reference values of enthalpy and density, respectively.  $C_p$  is specific heat capacity and  $\tau_{turb}$  represents Reynolds stress due to turbulence[5].

Since buoyancy-driven natural convection generates a very high Rayleigh number flow (Ra  $10^{10}$ - $10^{12}$ ) in the molten lead during fire test, it is imperative to consider an appropriate turbulence model and couple the turbulence transport equations with the continuity, momentum and energy conservation equations. As reported by Sanyal *et al.* [6] based on the experimental studies of Ozoe *et al.* [8], Choi *et al.* [9], Michalek [10],  $k$ - $\omega$  shear stress transport (SST) model of turbulence is the best suited for simulating moderate to high Rayleigh number natural convection-driven turbulent flow of fluids with or without phase change. Therefore, for the analyses of both the casks,  $k$ - $\omega$  SST model of turbulence, developed by Menter [11], has been adopted. The model blends the  $k$ - $\omega$  formulation in the near-wall region with a modified  $k$ - $\varepsilon$  formulation in the far field employing a suitable blending function.

### Turbulent transport:

The governing equations of the turbulence model are given below.

$$\frac{\partial(\rho k)}{\partial t} + \nabla \cdot (\rho \vec{V} k) = \nabla \cdot (G_k \nabla k) + G_k - Y_k + S_k \quad (5)$$

$$\frac{\partial(\rho \omega)}{\partial t} + \nabla \cdot (\rho \vec{V} \omega) = \nabla \cdot (G_\omega \nabla \omega) + G_\omega - Y_\omega + S_\omega + D_\omega \quad (6)$$

where  $G_i$  ( $i=k, \omega$ ) is the effective diffusivity,  $G_i$  ( $i=k, \omega$ ) represents the generation,  $Y_i$  ( $i=k, \omega$ ) represents the dissipation and  $S_i$  ( $i=k, \omega$ ) represents the source term for  $k$  and  $\omega$ , respectively. In Eq. (6),  $D_\omega$  represents a cross-diffusion term for  $\omega$ . The detailed definition of these terms are available in Menter [11] and are not presented here for the sake of brevity.

### Energy transport:

The energy transport equation is given below.

$$\frac{\partial \rho h}{\partial t} + \nabla \cdot (\rho \vec{V} h) = \nabla \cdot (\eta \nabla h) - \frac{\partial \rho \Delta H}{\partial t} - \nabla \cdot (\rho \vec{V} \Delta H) \quad (7)$$

$h = \int_{T_{ref}}^T c_p dT$  is the sensible enthalpy,  $\eta$  ( $\eta = k/\rho c_p$ ) is thermal diffusivity, and  $\Delta H$  is the latent heat content and is a function of temperature.

The latent heat content can also be written in terms of the latent heat of the material ( $L$ ) as given by Eq. (8).

$$\Delta H = sL \quad (8)$$

where  $s$  is the liquid fraction and can be defined for the temperature between solidus and liquidus temperature as:

$$s = \frac{T - T_{solidus}}{T_{liquidus} - T_{solidus}} \text{ with } T_{solidus} < T < T_{liquidus} \quad (9)$$

Liquid fraction for the temperature in liquidus and solidus region can be given as

$$s = 0 \quad \text{if } T < T_{solidus}$$

$$s = 1 \quad \text{if } T > T_{liquidus}$$

The condition that all velocities in solid regions are zero is accounted for in the enthalpy-porosity approach by appropriately defining the parameter  $A$  in equations (2),(3) and (4). The basic principle is to gradually reduce the velocities from a finite value in the liquid to zero in the full solid. In order to achieve this behaviour, an appropriate definition of  $A$  is given as [7]:

$$A = -\lambda \frac{(1-s)^2}{s^3 + b} \quad (10)$$

where  $b$  is a small computational number (0.00001) to avoid division by zero and  $\lambda$  is a very large number ( $10^9$ ) [12].

It should be mentioned that although any convenient model may be acceptable for extinguishing velocities in solidifying cells in isothermal phase change systems, it is desirable that the method chosen allows a smooth, gradual transition rather than a step-change in the velocity. Step changes in the momentum equation source term tend to retard numerical convergence and may even lead to divergence.

The following assumptions were made during the analysis:

- Considering geometrical and thermal symmetry, a 2D axisymmetric model of the cylindrical cask and a 3D model representing 1/4<sup>th</sup> part of the rectangular cask were considered.
- For simplifying the CFD model and reducing the computational effort, the fuel bundles, trays, lifting arrangements and supports were not modeled.
- The internal heat generation in the spent fuel was applied in terms of average heat flux on the inner surface of the cask.
- Differential expansion and Marangoni convection of molten lead during fire and post fire test condition were not considered.

The following boundary conditions for heat transport are applied under normal, fire test and post-fire cool-down conditions:

### Normal:

$$-k_{ss} \frac{\partial T_{co}}{\partial n} = h_{co,\infty} (T_{co,s} - T_\infty) + \sigma \varepsilon_s (T_{co,s}^4 - T_\infty^4) - \alpha_{co,s} q_{co,solar} \quad (11)$$

### Fire Test:

$$-k_{ss} \frac{\partial T_{co}}{\partial n} = h_{co,f} (T_f - T_{co,s}) + \sigma \varepsilon_f T_f^4 - \sigma \varepsilon_{co,s} T_{co,s}^4 \quad (12)$$

### Post-Fire Cool Down:

$$-k_{ss} \frac{\partial T_{co}}{\partial n} = h_{co,pf} (T_{co,s} - T_\infty) + \sigma \varepsilon_s (T_{co,s}^4 - T_\infty^4) \quad (13)$$

$n$  is the local normal to the surface,  $\sigma$  is the Stefan–Boltzmann's constant,  $\varepsilon$  is the emissivity and  $\alpha$  is the absorptivity. Subscripts  $ss, co, f, pf$  and  $s$  refer to stainless steel, cask outer, fire, post fire and surface, respectively.

### Solution Methodology

For comparison purpose, two sets of simulations were carried out for transient fire analysis. In one simulation, analysis was carried out considering only pure conduction, and in the second simulation, the effect of natural convection with phase change along with full turbulent coupling was considered. Pressure–velocity coupling was achieved using SIMPLE algorithm of Patankar [13]. At first, the steady-state solution was achieved. The thermal state of the cask obtained as the steady-state solution was considered as the initial condition for the transient fire test for 30 min. Iterative implicit algorithm was employed for solving transient flow. The analyses revealed a significant change in the melting pattern with full convective and

turbulent coupling compared to the results obtained for conductive melting alone.

The 2-D axisymmetric simulation (with approximately 30,000 cells) of cylindrical cask was carried out on Quad-core CPU machine. The steady-state analysis took one-hour machine time to complete. The pure conduction fire-test analysis of 1800 s took 80 hours of machine time while the fire-test analysis with natural convection consideration took 300 hours of machine time. The 3-D simulation of rectangular cask (with approximately 3.5 lakh cells) was carried out on eight-core XEON machine. The steady-state analysis took two-hour machine time to complete. The pure conduction fire-test analysis of 1800 s took 300 hours of machine time while the fire-test analysis with natural convection consideration took 1300 hours of machine time.

### Results and Discussions

At first, steady state temperature profiles were computed for the cylindrical and rectangular casks considering internal heat generation due to radiation from the inner bundle, solar insolation on the outer surface and heat dissipation due to convective heat transfer from the outer walls to the ambient. The temperature

profiles for the casks of different cross-sections are depicted in Fig. 2. From this figure, it can be observed that under steady-state conditions, the maximum computed temperature in the cylindrical cask is 352 K, and the minimum computed temperature is 343.8 K. The maximum temperature occurs at the top half of the inner surface. The temperature falls from the inner to the outer wall in the cask. Since the maximum temperature is much lower than the melting point of lead, thermal transport occurs through pure conduction across the solid steel shells and shielding lead. The curved thermal contours are typical of conductive thermal profile with a thermal source in the inner wall. Similarly, for the rectangular cask, the maximum steady-state temperature is 392 K, and the minimum temperature is 368 K. Again, in this case, thermal transport occurs by means of pure conduction only.

The temperature distribution obtained as a solution of the steady state analysis is used as the initial condition for the subsequent transient analysis under fire test conditions with natural convection. For the cylindrical cask, the transient case was run with adaptive time-stepping for maximum time step of 0.1 s and a minimum time step of  $10^{-5}$  s, respectively up to a time of

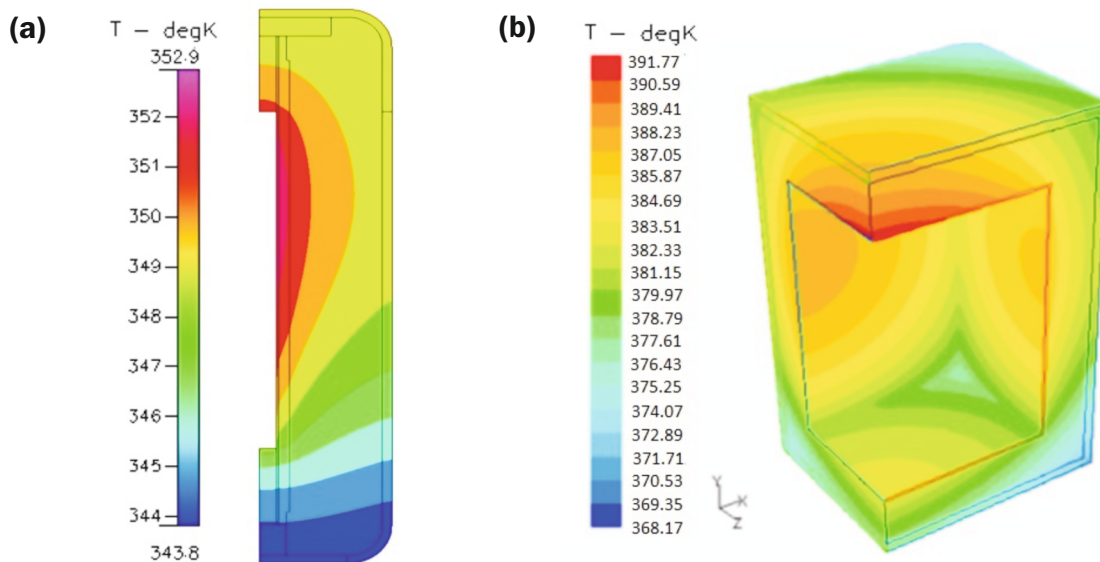


Fig.2: Steady state temperature profiles in (a) cylindrical cask (b) rectangular cask (1/4<sup>th</sup> section)

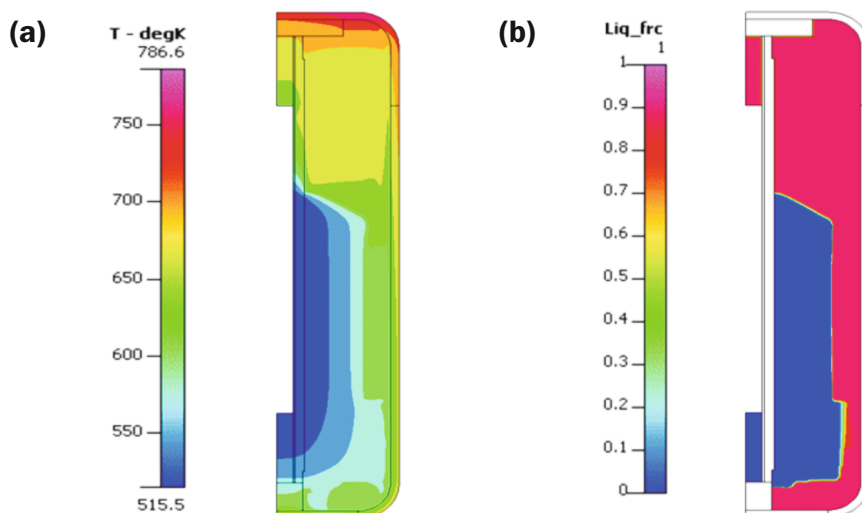
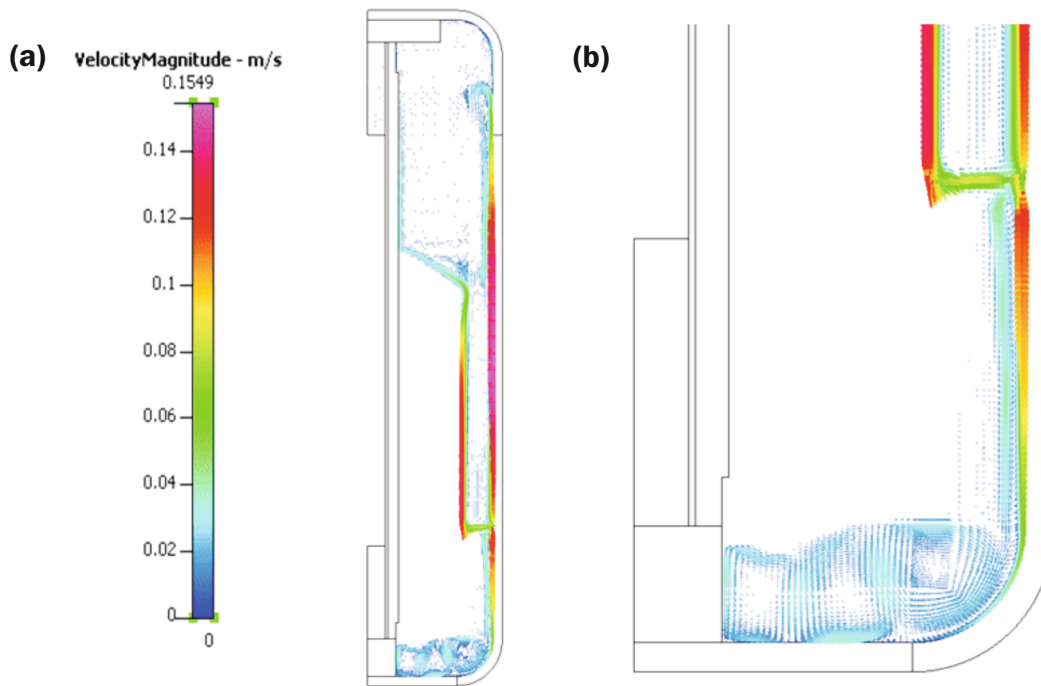
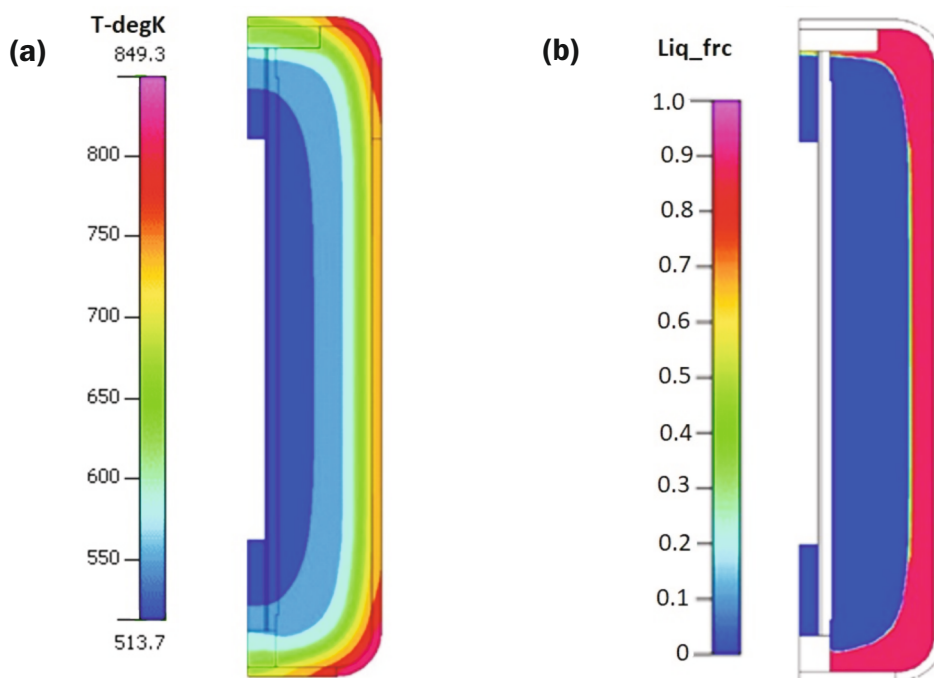


Fig.3: (a)Temperature contours and (b) melt interface contours at the end of fire test simulation for cylindrical transport cask considering natural convection





**Fig.4:** Velocity vectors (a) full view and (b) bottom zone view at the end of fire test simulation for cylindrical transport cask considering natural convection



**Fig.5:** (a)Temperature contours and (b) melt interface contours at the end of fire test for cylindrical transport cask considering pure conduction

1800s. The thermal contours and lead melt interface at  $t = 1800s$  for the cylindrical cask are shown in Fig. 3, while the velocity vectors are shown in Fig. 4.

From Figs. 3 and 4, it can be observed that thermal profiles are dictated by the high Rayleigh number convection patterns in the cask. There is a dominant anti-clockwise recirculation loop across the vertical direction of the cask with vertically downward flow along the melt interface and vertically upward flow along the cask wall. At the bottom of the cask, the flow exhibits multiple counteracting recirculation loops. This is typical of Rayleigh Bernard instability which originates at the bottom of cask due to a relatively thin layer of molten lead trapped between the bottom

wall of the cask and the solid lead. The Rayleigh Bernard flow with counteracting loops sets in because the molten lead at this location experiences higher temperature at the bottom wall and lower temperature at the melt interface.

For the sake of comparison, the temperature contours and melt front of cylindrical cask for pure conduction are presented in Fig.5. Conductive heat transport results in thermal and phase change contours symmetric with respect to the horizontal axis, which is physically inaccurate due to the effect of buoyancy being neglected. Fig. 6 depicts the comparison between the computed thermal profiles for convective and conductive melting of lead in the cylindrical cask obtained along the horizontal and vertical

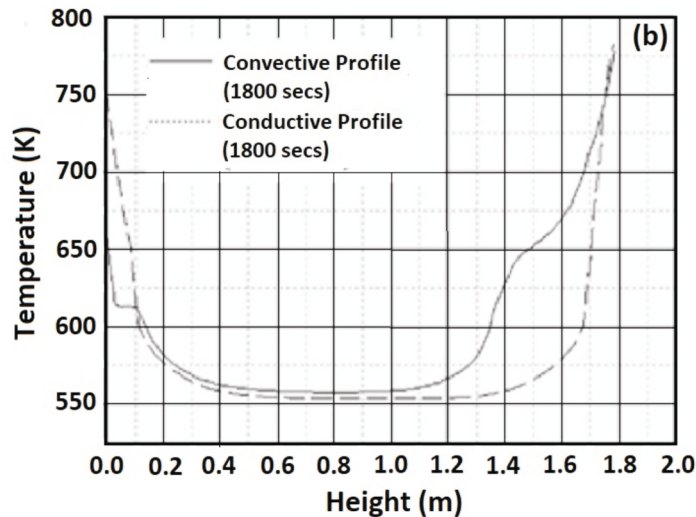
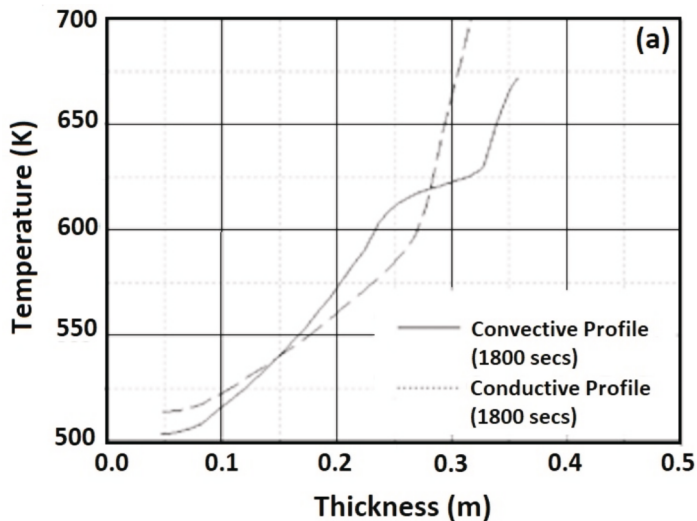


**Fig.6:** Comparison between temperature profiles in cylindrical cask (a) along the thickness at mid height and (b) along the height at mid thickness

direction at mid height and mid thickness of the cavity, respectively, at the end of the fire test.

From Figs. 5 and 6, it is observed that the profiles obtained for high Rayleigh number convection is significantly different from the profiles obtained computationally using the assumption of pure conductive heat transport in the cask. Along the thickness, the convection creates steep thermal gradient across the inner and outer walls of the cask than that in case of the conductive melting. Near the core, convection creates a nearly constant temperature unlike that for pure conduction. Along the height, convective heat transport results in an asymmetric thermal profile with respect to the horizontal axis unlike the nearly perfect symmetric thermal profile obtained using pure conduction analysis.

As a consequence of the effects of natural convection, the nature and extent of lead-melting in the cylindrical cask under convective flow is substantially different from that of conductive melting. At the end of 30 min of fire test, the lead melting for pure conduction analysis is 33% (v/v), while the extent of lead-melting estimated under convective melting is as high as 70% (v/v), which is more than twice the figure estimated by conductive melting. Moreover, the shape of the solid-liquid interface is substantially different in convective melting compared to the case of conductive melting due to high Rayleigh number turbulent convection.

From the analysis of the cylindrical cask, it was established that ignoring natural convection during thermal analysis of cask leads to erroneous results. Hence, the computations for rectangular cask were only carried out by considering natural convection. The  $k-\omega$  SST model with appropriate wall functions was employed with variable time stepping of maximum time step of 0.1 s and a minimum time step of  $10^{-5}$  s, up to 1800s. Figs. 7 and 8 show the temperature contours and melt interface contours for the rectangular cask, respectively.

In Fig. 8, it is clearly shown that after 30 minutes, melting of lead takes place only at a small fraction of the cavity volume at the top and bottom corners of the cavity. The rectangular cask is substantially larger than the cylindrical cask, resulting in much-reduced melting, 11% (v/v), at the end of the fire test, compared to more than six-fold melting in the case of the cylindrical cask.

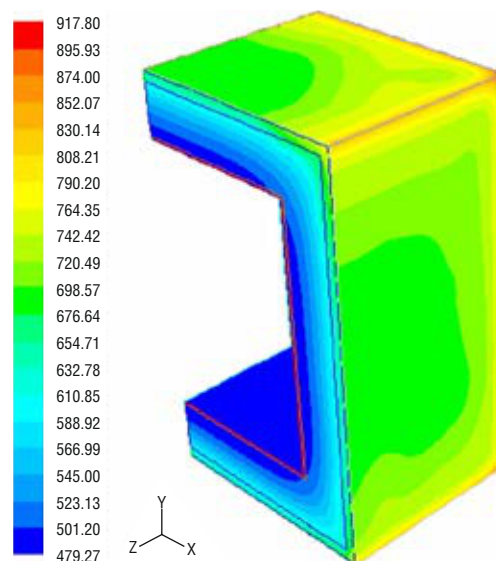


**Fig.7:** Temperature Contours in the rectangular cask (1/4<sup>th</sup> section) due to convective melting of lead at the end of fire test at 1800s (Full View)[6]

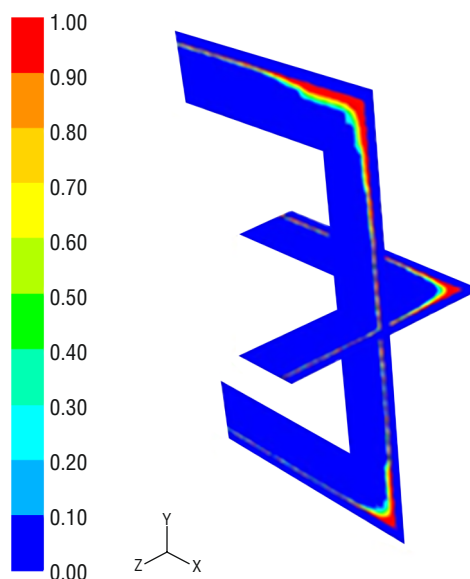


**Fig.8:** Melt interface contours in the rectangular cask (1/4<sup>th</sup> section) due to convective melting of lead at the end of fire test at 1800s across mid-planes perpendicular to Y and Z-axes[6]

For both the casks, since the melting patterns do not change in post-fire conditions, those results are not presented here for the sake of brevity.

## Conclusions

Comprehensive CFD analysis of transportation cask for two different geometries (cylindrical and rectangular) have been carried out considering natural convection in the lead melting. The study reveals a substantial influence of natural convection on the thermal state and melting behaviour of lead which may have a great bearing on the safety during transportation of cask. It was found that Rayleigh number convection was pronounced on the extent of melting of the lead layer in comparison with the conductive melting simulation study. Convective melting led to 70% (v/v) melting of lead layer in the cylindrical cask at the end of the fire test, compared to 33% (v/v) melting estimated in the case of conductive heat transport alone. For the larger cask of rectangular cross-section, the amount of melting was substantially smaller (approx. 11% by volume) compared to that of the cylindrical cask. The present work shows that the thermal design of a transport cask based only on conductive melting is grossly inaccurate and needs close coupling with an accurate turbulence model to account for the effects of high Rayleigh number convection generated during the fire test in a cask.

## Corresponding author\*

Priyanshu Goyal (pgoyal@barc.gov.on)

## References

[1] Code for Safety in Transport of Radioactive Materials, AERB Code No. SC/TR-1, 1986.

- [2] C.F. Bonilla, A.L. Strupczewski, *Nuclear Structural Engineering*, 1965, **2**, 40.
- [3] Eric. A. Brandes, *Smithells Metals Handbook*, Fulmer Research Institute Ltd, 6<sup>th</sup> Edition.
- [4] Chikanna Gowda, Priyanshu Goyal “Thermal Analysis of Transport Cask for Natural Convection During Melting of Lead: CFD Simulation”, M. Tech Thesis, June, 2009.
- [5] CFD-ACE+ User manuals, ESI CFD Inc V2009.
- [6] D. Sanyal, A. Chakraborty, V. Verma, P. Goyal, Final Report, BRNS Project, CSIR-CGCRI, Kolkata, India, 2005/36/7-BRNS/2283.
- [7] A.D. Brent, V.R. Voller and K.J. Reid, *Numerical Heat Transfer*, 1988, **13**, 297.
- [8] Ozoe, H., Mouri, A., M. Ohmuro, *Int. J. Heat Mass Transfer*, 1985, **28**, 125.
- [9] S.K. Choi, E.K. Kim, S.O. Kim, *5<sup>th</sup> Asian Computational Fluid Dynamics*, Busan, Korea, 2003, 27.
- [10] T. Michalek, *Numerical Heat Transfer*, Gliwice-Cracow, Poland, 2005.
- [11] F.R. Menter, *AIAA J.*, 1994, **32**, 1598.
- [12] R. Viswanath and Y. Jaluria, *Numerical Heat Transfer Part B - Fundamentals*, 1993, **24**, 77.
- [13] S.V. Patankar, *Numerical Heat Transfer and Fluid Flow*, 1980.

# Numerical modelling of deflagration to detonation transition in hydrogen air mixtures

Aditya Karanam\*, Vishnu Verma, Jayanta Chattopadhyay

Reactor Safety Division  
Bhabha Atomic Research Centre, Trombay, Mumbai-400085, India

## ABSTRACT

For over half a century, combustion researchers have studied the phenomenon of Deflagration-to-Detonation Transition (DDT). DDT phenomenon lies at the intersection of chemical kinetics, flow turbulence and compressible gas dynamics; and presents a formidable and challenging conundrum. In the nuclear industry, DDT is a known risk in accident scenarios involving unintended release and combustion of hydrogen. Through use of sophisticated measurements, experimentalists have clearly elucidated the mechanisms underlying DDT. More recently, numerical modeling has also been adopted as one of the methods for studying DDT. In this article, the multitude of effects involved in DDT have been presented from a physical standpoint. Then, numerical challenges and strategies to model DDT are described along with key validation results. Finally, the mechanistic aspects of DDT are also discussed.

**Keywords:** Numerical Modeling, Flame Acceleration, Shock Wave, DDT, Detonation

## Introduction

During severe accident in water-cooled nuclear power reactors, large quantities of hydrogen can be released into the atmosphere of the containment. The main source of hydrogen generation is the oxidation of zirconium clad and other metallic components in presence of steam, and Molten Corium Concrete Interaction (MCCI) after failure of reactor vessel. This hydrogen can get transported into the containment through a break in the reactor cooling system or during corium-concrete interaction. The hazard potential of hydrogen can be attributed to its physical properties as described in Table 1 [1]. Compared to a typical industrial gas like methane, hydrogen has a wider flammability limits, lower minimum ignition energy and higher reactivity (i.e. higher energy release and burning velocity). As a result, any unintended electrostatic discharge, hot surface, mechanical friction or an increase in local temperature above the minimum ignition threshold may lead to ignition.

Upon ignition, combustion usually starts locally but can quickly intumesce into a global deflagration. Under certain conditions, an abrupt transition called Deflagration-to-Detonation

Transition (DDT) may occur. Combustion in hydrogen-air mixture shows a particularly high propensity for DDT. Both deflagration and detonation are significant risks to containment integrity. The loading associated with detonation is of the impact type and may be more severe than the quasi-static loading of deflagrations. In the worst case scenario, if the containment design safety margin is crossed, the structural integrity of the containment may be breached. The potential risk associated with hydrogen combustion was first realized after the Three Mile Island (TMI) accident in 1979 where burning of a hydrogen cloud affected the integrity of the reactor containment. The Fukushima-Daiichi accident in 2011 reasserted that the hydrogen combustion issue cannot be neglected and control of hydrogen risk is still a key safety issue for operation of nuclear power plants.

## Physical Considerations of DDT

Across a combustion wave, the stored chemical energy of the reactants is converted into thermal and kinetic energy of the products. Broadly, combustion waves can be categorized as deflagration or detonation. Deflagrations propagate at subsonic speeds relative to the reactant mixture. These are expansion waves, across which the density decreases and the products are accelerated in a direction opposite to wave propagation. On the other hand, detonations are supersonic compression waves. The Mach number of a detonation wave relative to the reactants is

**Table 1: Comparison of physical properties between hydrogen and methane [1]**

Property	Hydrogen (H <sub>2</sub> )	Methane (CH <sub>4</sub> )
Flammability limits in air (%v/v)	4 -75	5 -15
Minimum ignition energy (mJ) <sup>1,2</sup>	0.02	0.33
Lower heating value (MJ/kg) <sup>1,2</sup>	118.8	50.0
Laminar burning velocity (m/s) <sup>1,2</sup>	3.06	0.39
Minimum ignition temperature (K) <sup>1,2</sup>	845	905
Density at STP (kg/m <sup>3</sup> )	0.0808	0.6430

<sup>1</sup>At stoichiometric conditions and STP

<sup>2</sup>Source: Sandia National Laboratories

**Table 2: Properties of deflagration and detonation**

Parameter	Deflagration	Detonation
Mach number <sup>1</sup>	< 1 (subsonic)	> 1 (supersonic)
Density ratio <sup>1,2</sup>	< 1 (expansion)	> 1 (compression)
Pressure ratio <sup>1,2</sup>	~1 (constant pressure process) >1 (constant volume process)	> 1
Temperature ratio <sup>1,2</sup>	> 1 (exothermic)	> 1 (exothermic)

<sup>1</sup>The actual values will depend on the gas mixture and initial conditions  
<sup>2</sup>Ratio of product value to reactant value

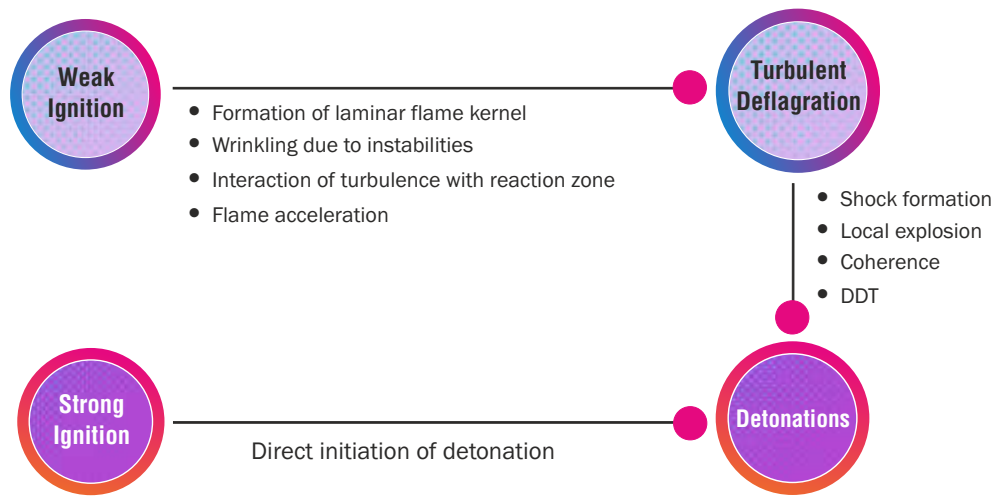


**Fig. 1:** Overview of the mechanisms leading to DDT

greater than one. Across a detonation front, there is a significant increase in density, and the products follow the direction of wave motion. Theoretical change in thermodynamic properties across a combustion wave (deflagration or detonation) can be computed using the Rankine-Hugoniot relations [2]. The properties of deflagration and detonation are summarized in Table 2.

Thermodynamic analysis merely tells us the existence of two types of waves and their properties, but it provides no information on which of these waves will actually persist in a domain. Whether a deflagration or detonation will initiate in a mixture primarily depends on the ignition source. In a weak ignition such as a spark discharge, a minute energy of the order of  $10^5$  J or higher is deposited in a very localized volume [3]. This leads to formation of a laminar flame kernel at the location of the ignition. If the mixture is flammable and quenching does not occur, a self-sustained deflagration wave can propagate. In a strong ignition, a gargantuan energy source of the order of  $10^4$  J or higher is deposited, for example through a high explosive charge [3]. Direct detonation can be initiated through a strong ignition.

Hydrogen deflagrations can undergo flame acceleration due to thermo-diffusive and hydrodynamic instabilities and turbulence [4]. An initially smooth laminar kernel gets wrinkled and entrains more of the reactant mixture; causing an increase in the flame surface area. An increase in flame surface area further

augments instabilities leading to higher flame wrinkling. This positive feedback loop ultimately leads to a fully developed turbulent deflagration. The primary propagation mechanism is turbulent transport and depends on the interaction between turbulence and heat release in the reaction zone. The average rate of propagation of a turbulent deflagration is characterized through turbulent flame speed, which for hydrogen flames can be 1-2 orders of magnitude higher than the laminar burning velocity [5].

During propagation of deflagration, acoustic disturbances can travel into the reactant mixture and coalesce into shock waves. Shock waves may reflect from the domain boundaries and pre-compress the reactant mixture to high temperature and pressure. In the absence of driving force, such shocks may get quickly attenuated. But, under certain critical conditions, a local explosion (strong ignition) can take place in the vicinity of a shock front. If the magnitude and rate of energy released from the local explosion are sufficient to sustain the shock propagation, then a spontaneous coupling can take place between the shock and the trailing explosion (coherence), eventually leading to a transition from deflagration to detonation. DDT is associated with an abrupt increase in local pressure and flame speed. Subsequently, a detonation wave propagates into the reactant mixture. Detonations are essentially self-sustained shock waves driven by a trailing local explosion. The various mechanisms leading to DDT are illustrated in Fig. 1.

During a severe accident, the possibility of strong ignition and direct detonation can be ruled out. However, weak ignition sources are abundant and the formation of detonation through DDT cannot be precluded. Thus, modeling of DDT is essential to calculate the design safety margin of equipment, internal structures and containment. Such studies also help in optimum design and placement of hydrogen mitigating devices.

### Numerical Modeling of DDT

Numerical modeling of DDT has specific challenges which are highlighted below:

- Combustion of hydrogen happens through a network of elementary reactions involving several intermediate species. The individual reactions occur at vastly different time scales and are coupled non-linearly. So, a direct modeling approach which resolves all the chemical time scales is highly computationally intensive.
- Due to presence of multiple species including steam, all the thermodynamic and transport properties have to be specified for multi-component mixtures. Some important properties like laminar burning velocity in presence of steam are not known in the existing literature and have to be derived from first principles.
- Modeling of combustion instabilities which is critical for the initial flame propagation from laminar flame kernel is a difficult problem. This is due to the sub-unity Lewis number and multiple instability mechanisms which are prevalent.
- Different turbulent intensities from low to high and associated length and time scales can exist during flame propagation. While turbulence modeling of non-reactive flows is well established, several gap areas exist for reacting flows due to the non-linear coupling between flow turbulence and heat release in the reaction zone. Modeling of this turbulence-chemistry interaction is of critical importance to accurately predict turbulent flame speed and burning rate. Turbulent quenching and local flame extinction also have to be modeled.
- DDT involves formation and propagation of shock waves. To capture these accurately, fully compressible and conservative form of the Navier-Stokes equations and appropriate shock resolving numerical schemes have to be employed. This increases the grid and time discretization requirements considerably.
- Mathematically, subsonic phenomena like deflagrations exhibit parabolic behavior while supersonic flows like detonations exhibit hyperbolic behavior. Separate numerical schemes are available for these class of flow problems, but less is known about their performance in mixed parabolic-hyperbolic behavior that can be expected during DDT.
- An important physical phenomenon that has to be accounted for is the local explosion. The explosion boundary for hydrogen-air mixture is highly dependent on the mixture composition and pressure, both of which can show significant gradients during DDT. Modeling the location of local explosion and the energy released therein is an important and challenging aspect.
- A key practical challenge is the geometric scalability to larger domains. For example, a domain of  $1\text{m}^3$  with a flame thickness of  $0.5\text{mm}$  and a modest number of 10 control volumes over the flame thickness will require 8 trillion computational cells. In the context of hydrogen safety for 700 MWe Indian PHWR, the geometric volume of the containment is of the order of  $70000\text{m}^3$ . As per Moores law, scaling up the fully resolved simulations to real-world

containment applications will increase the grid requirement exponentially, to a limit beyond the present availability of computational and time resources. When this is combined with shock resolving numerical schemes, it will increase the complexity to intractable dimensions.

Objective of the present work is to explore models and numerical techniques that can address some of the challenges mentioned above without compromising on the accuracy of predicting key safety parameters. The generalized conservative and compressible form of Navier-Stokes equations have been considered. To account for turbulence, Reynolds Averaged Navier Stokes (RANS) or Large Eddy Simulation (LES) may be used. In the present work, the RANS approach has been chosen so that it can be scaled up to larger physical domains. Also, RANS approach provides good estimates on the macroscopic parameters of interest. Due to variation in the density field, the averaging procedure is based on Favre decomposition.

For combustion modeling, the geometric approach based modeling has been employed [5]. In the geometric approach, the flame front is identified to be a surface convected and distorted by the flow field. Combustion is then quantified in terms of effective flame speed and the available flame surface. This approach is very well suited to situations in which combustion occurs in the flamelet regime. Flamelets can be described as thin regions in which combustion occurs. Whether combustion occurs in the flamelet region is governed by the Damkohler number, which is defined as the ratio of turbulent mixing to chemical time scales. For hydrogen combustion, the elementary reactions take place very fast for temperatures higher than the ignition temperature; therefore the chemical time scale is small. Also, there are no sources for large turbulence generation, except those generated by the propagating flame itself and its interaction with the surrounding domain. As the turbulence intensity is small, the time scale associated with turbulence eddies in the flow field are large. Therefore, one can expect that the Damkohler number is much higher than unity. But this is just a heuristic argument. Detailed Borghi diagram analysis has to be carried out to actually determine the variation of the Damkohler number during flame propagation in a constricted domain like a shock tube. This entails computation of turbulent time scale and various chemical time scales in real time and map the variation of the Damkohler number on the Borghi diagram. The authors have determined through such analysis that the Damkohler number varies in the range of  $10^2$ – $10^4$ , thus signifying that the combustion takes place in the flamelet regime and the geometric approach is indeed justified [6].

The geometric approach relies on the Turbulent Flame Closure (TFC) model of Zimont [7]. The TFC model is in-turn based on the transport equation for the progress variable; which can be defined as the non-dimensional temperature across the flame. The source term of this equation represents the heat release due to combustion. The turbulence-chemistry interaction is modeled using the flame wrinkling factor. As the turbulence modeling is based on RANS, all the fluctuations are averaged out. Thus the wrinkling phenomenon which is essentially a coupling between turbulent fluctuations and flame is also averaged out, and cannot be captured on a physical level and needs to be modeled. Even if the mesh is resolved to very fine levels, the inherent limitation of RANS prevents us from physical modeling of flame wrinkling. Thus, appropriate models have to be employed to include effect of flame wrinkling at the sub-grid scale. The

problem is now reduced to determining appropriate models for the sub-grid scale flame wrinkling factor. In essence, the model does not directly address various local processes occurring in turbulent flames, but assumes their universal character and accounts for the effects of such processes on the mean heat release rate. The model of Dinkelacker *et al.* has been adopted to model the sub-grid flame wrinkling factor [8]. This model accounts for the effect of thermo-diffusive instabilities through its dependence on the Lewis number. For lean hydrogen-air mixture, a sub-unity Lewis number enhances local diffusion of species thus increasing the burning rate and enhancing thermo-diffusive instability. In addition, this model captures the effects of increasing pressure on the turbulent flame speed. For the present problem, the authors have shown that the Dinkelacker model is highly appropriate [9].

To model local explosions, the induction delay times have been tabulated at various mixture compositions, pressures and temperatures using independent zero-dimensional kinetics calculations and made run-time available to the solver. This methodology has been adopted based on the work of Ettner *et al.* [10]. In locations where local explosion takes place, the heat release is augmented as an additional source term in the transport equation for progress variable. All the equations and models have been converted into a numerical framework using the open-source toolbox, OpenFOAM [11].

### Numerical Setup

The experimental data used to validate the present formulation is based on shock-tube experiments conducted at the GraVent facility, which is available in the open literature [12]. This facility is an entirely closed shock tube channel of high aspect ratio with a rectangular cross-section and channel length of 5.1 m, height of 0.06 m and width of 0.3 m. The mixture is ignited at one end of the channel and the flame propagation characteristics are studied along the channel length. To enhance turbulence, the channel has a provision to include periodic obstacles along its length. There are seven uniformly placed obstacles from 0.25 to 2.05 m from the ignition end. A schematic of the experimental setup is shown in Fig.2. The setup also has a provision to create a transverse (normal to flow direction) gradient of hydrogen distribution to capture the effects of stratification of hydrogen

during an accident scenario. This is achieved by injecting hydrogen through the top wall of the facility through small holes. Once hydrogen is injected, ignition is done within a certain time such that sufficient time is not allowed for uniform mixing, thus obtaining a stratified initial distribution.

Flame propagation in presence of obstacles with 30% blockage ratio has been considered. For an average concentration of 20%, if the mixing time is 3 sec, the initial stratified hydrogen concentration varies from 4.7% at the bottom wall to 37.5% at the top wall. Such distribution has been considered in the experimental work of Boeck *et al.* and available in the open literature [13]. The flame propagation in an obstructed geometry in presence of stratified initial distribution presents a realistic initial condition and is highly relevant from hydrogen safety in containment.

All numerical simulations have been carried out in a 2D domain using OpenFOAM. The initial conditions used are:  $T = 297$  K and  $P = 1$  atm. A grid size of 4 mm is used for all simulations after grid optimization study [14]. The grid is fully structured and orthogonal with zero skewness. The aspect ratio in all directions is unity. Such a grid setting is essential to capture shock discontinuities with minimum numerical diffusion. The mixture is assumed to be in quiescent state and hence the initial velocity in the domain is set to 0 m/s. Turbulence is modeled using the k-omega two equation model due to its good performance for both bulk and wall bounded flows. Since the flow is initially undisturbed, a low value of initial turbulent kinetic energy based on a turbulent intensity of 1% is used. The boundary conditions are described as adiabatic no-slip walls. The simulation is carried out in a transient way with implicit time discretization. The time step is determined during the solution based on the maximum acoustic Courant number of 0.3 to ensure stable progress of the solution. This resulted in an extremely small time steps of the order of  $0.5 \mu s$ . Local time step convergence within a time step has been ensured. All equations are discretized with second order upwind schemes and solved with a tolerance of  $10^{-6}$ . For high speed flows which are expected during FA and DDT, a flux-limited TVD scheme is used for better shock capturing. This scheme ensures stable convergence when the Mach number in the domain exceeds a value of 0.2. Density changes in the flow are accounted by using the ideal gas equation of state. Ignition is

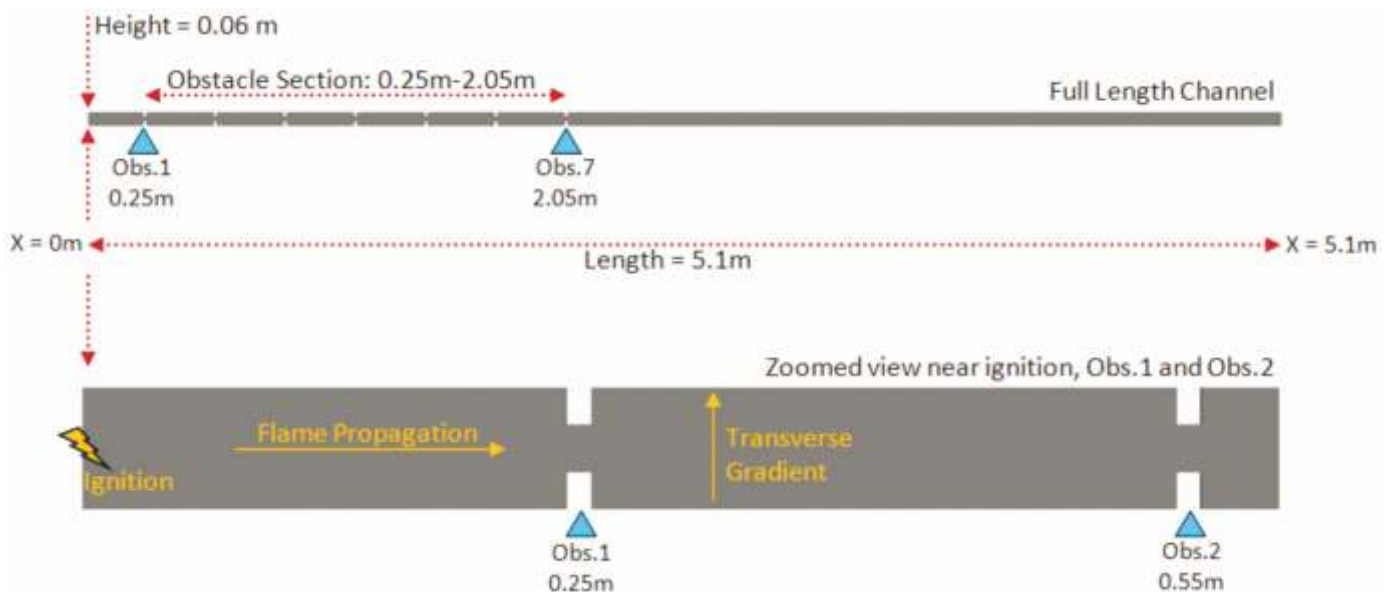


Fig.2: Schematic diagram of the GraVent experimental facility

modeled by patching a spherical region with temperature equal to the adiabatic flame temperature corresponding to 20%. Combustion modeling is based on the geometric approach i.e. progress variable equation with turbulent flame closure and tabulated ignition delay tables, as described in detail in the previous section.

### Numerical Results and Validation

The temperature contours at  $t = 10$  ms is depicted in Fig.3. The thin region separating the high and low temperature sides may be interpreted as the flame front. The flame front is observed to elongate over the propagation distance and results in an asymmetric shape. This is attributed to preferential flame propagation towards the upper regions of the domain where the hydrogen concentration is higher. Fig.4 depicts a plot of flame speed vs. flame position from numerical simulation and the corresponding experimental data. The flame speed and flame location are based on the leading edge of the flame at any instant, as per the experimental procedure. The increasing slope clearly indicates flame acceleration. As the flame propagates, different regimes of combustion and the transition between them can be identified. The figure is overlaid with acoustic speeds corresponding to reactant and product temperatures (387 m/s and 904 m/s respectively). For flame speed lower than acoustic barrier w.r.t reactant (region A), the propagation is a slow turbulent deflagration. Good qualitative agreement can be

observed between the numerical simulations and experiments. Flame speed is in the range of 0-387 m/s in region A ( $x < 0.85$  m). As the flame propagates further, flame acceleration continues due to turbulence-flame interaction. Region B indicated in Fig.4 corresponds to fast turbulent deflagration in which shock fronts may have formed ahead of the flame. Experimental data suggests that flame acceleration here is higher than that in region A. This trend is captured from numerical simulations also. Higher flame speeds in presence of shocks can be attributed to increase in turbulent diffusivity and heat release rate from pre-compression of the reactants. As seen from the numerical simulation, the flame speed exceeds acoustic barrier w.r.t products at  $x = 1.65$  m. At this condition, a sudden jump in propagation speed can be observed and interpreted as the transition from deflagration to detonation (DDT). Numerically predicted flame speed increases to a peak value of 2384 m/s at  $x = 2.06$  m, while the experimental value peaks to 2448 m/s at  $x = 2.45$  m. Thus, in terms of peak flame speed prediction, the numerical simulations are comparable to experimental data. Also, the slope of the numerical flame speed curve is comparable to the experimental values. Additionally, some heat loss from the enclosing walls is expected in the experiments and this can also lower the energy release rate. Due to these factors, the numerically predicted peak location may have shifted to an earlier axial location. Subsequently, numerical prediction shows a constant flame propagation at the speed of

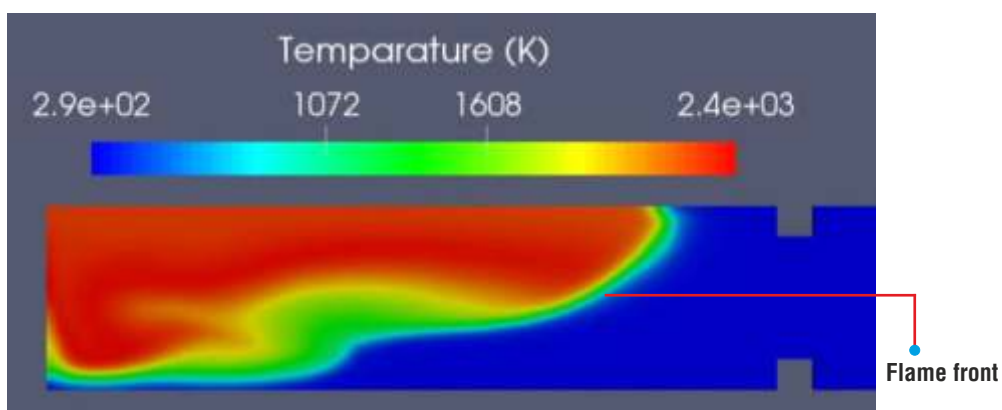


Fig.3: Temperature contours at 10 ms for stratified initial distribution

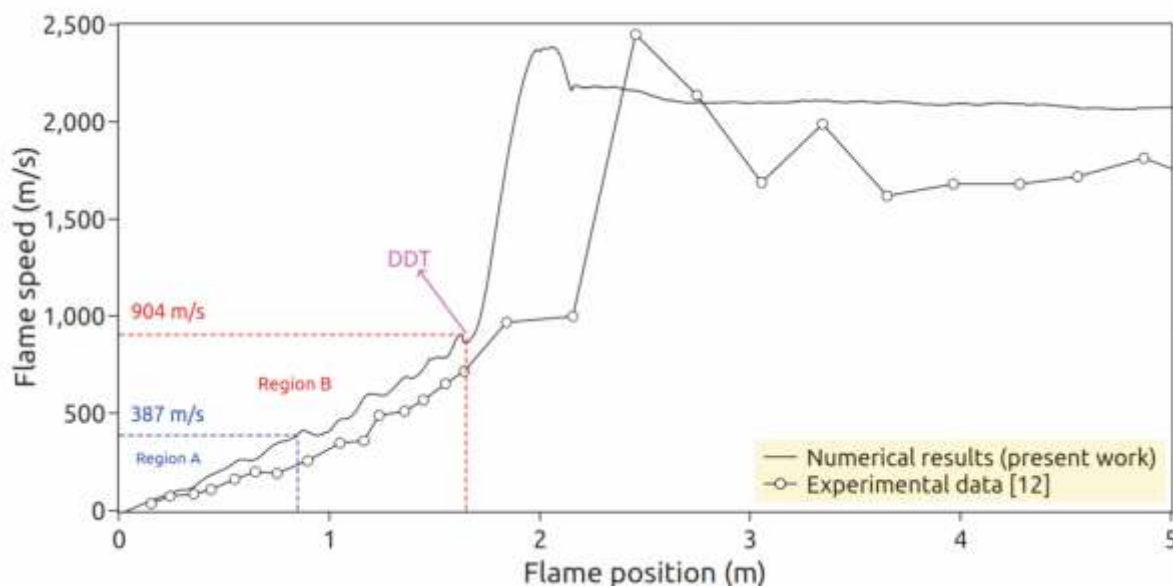


Fig.4: Different regimes of combustion, DDT and validation with experimental data



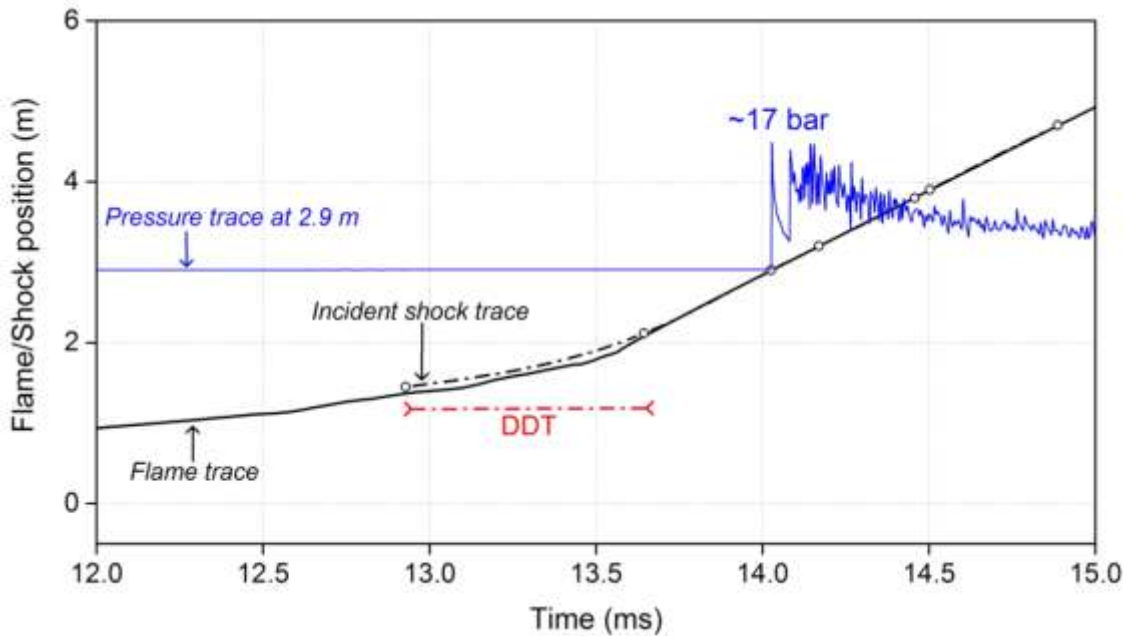


Fig.5: Flame, pressure and shock trace profiles during DDT

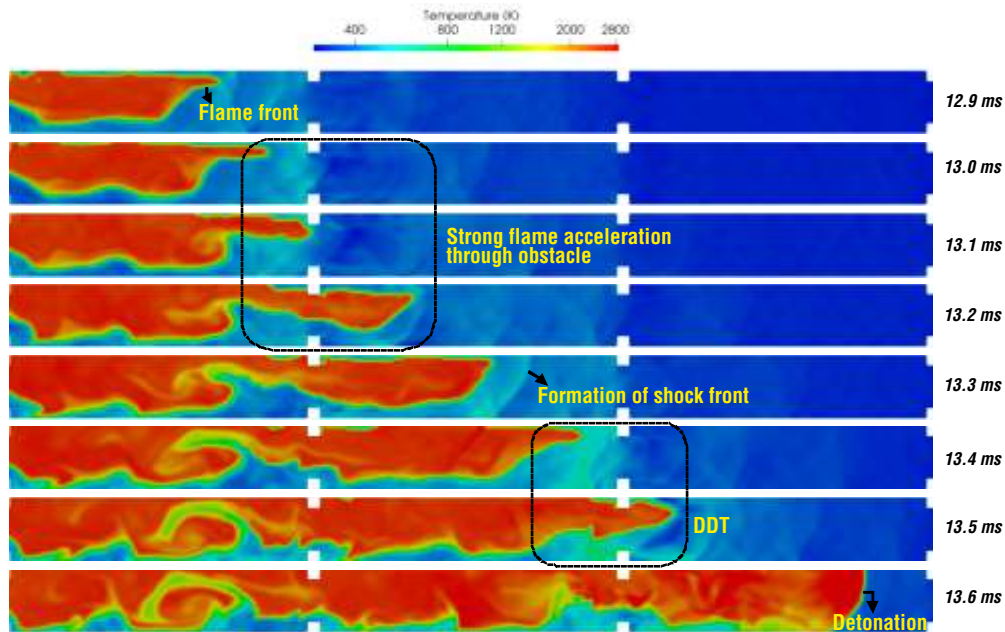


Fig.6: Visualization of flame propagation and interaction with shock front to elucidate DDT and formation of detonation wave

2069 m/s, while the experimental data suggest some oscillations. This has not been captured in the simulations and further analysis may be required to understand this behavior.

The DDT mechanism can be further explained through Fig.5 which shows flame and shock traces, both obtained from numerical simulations. Due to high flame speeds (Fig.4), shocks are expected to form ahead of 0.85 m in the domain. The first location of shock formation (incident shock) is at 1.45 m in the domain at an instant of ~12.9 ms. From the flame trace, it may be observed that the flame front is closely trailing the shock front. Thus, the reactants are pre-compressed by the leading shock before the flame zone. From the first instant of shock formation at 12.9 ms and up-to 13.6 ms, it may be observed that the distance between the flame and the leading shock front continuously

diminishes. This duration may be interpreted as DDT. At 13.6 ms, the flame front and the lead shock (incident shock) coalesce to complete the DDT process. Subsequently, the spike in pressure is collocated with flame as can be seen from the pressure trace at 2.9 m and further locations, and may be interpreted as a detonation front. The theoretical Chapman-Jouguet pressure rise corresponding to 20% of hydrogen in air is 13 bar and the pressure spike obtained numerically is 17 bar. This difference may be attributed to the initially stratified hydrogen distribution.

The temperature contours during DDT (12.9-13.6 ms) are presented in Fig.6. At 12.9 ms, the flame front is seen to approach the obstacle. The flame propagation through the obstacle can be observed in the duration from 13.0-13.2 ms. This enhances flame acceleration due to turbulence and creates a higher impetus for strong shock formation. As a result, at the instant of 13.3 ms, a

shock front has formed ahead of the flame. At further instants of time, the interaction between flame leading edge and shock front leads to DDT. At 13.6 ms, the flame and the shock coalesce to form a detonation wave, which propagates further into the unburned reactant mixture, as also explained in Fig.5.

## Conclusions

In this paper, a numerical method for modeling DDT has been presented. Appropriate sub-grid models have been used to account for instabilities, turbulent flame propagation, quenching and local explosion. Suitable numerical schemes have been adopted to model both subsonic deflagrations and supersonic detonations. The numerical method works on a relatively coarse grid and can be extended to larger domains. Detailed validation studies were carried out in a shock tube channel with obstacles in the flow path and with initially stratified hydrogen distribution. Different regimes of combustion like slow and fast deflagrations, DDT and detonations were observed from the numerical simulations. The numerically obtained flame speeds showed good agreement with experimental results for all regimes of combustion. Studies on pressure traces revealed the formation of a shock front in close proximity and ahead of the flame. Due to fast moving flame front, the distance between the flame and shock was observed to monotonically decrease until the flame and shock locations coincided, thereby completing the DDT process. Further modeling improvement is required to more accurately capture experimental trends and this work is in progress.

## Corresponding Author\*

Aditya Karanam (adityakb@barc.gov.in)

## References

- [1] A comparison of hydrogen and propane fuels, NREL report (<https://www.nrel.gov/docs/>)
- [2] S. Turns: An Introduction to Combustion, Third Edition, McGraw Hill, New Delhi, India, 2012.
- [3] IAEA-TECDOC-1661, Mitigation of Hydrogen Hazards in Severe Accidents in Nuclear Power Plants, 2011.
- [4] M. Matalon, *Annual Review of Fluid Mechanics*, 2007, **39**, 163.
- [5] D. Veynante and L. Vervisch, *Progress in Energy and Combustion Science*, 2002, **28**, 193.
- [6] Aditya Karanam, Sunil Ganju and Jayanta Chattopadhyay, *Combustion Science and Technology*, 2020, <https://doi.org/10.1080/00102202.2020.1732363>.
- [7] V.L. Zimont, *Experimental Thermal and Fluid Science*, 2000, **21**, 179.
- [8] Dinkelacker F, Manickam B and Muppala S, *Combustion and Flame*, 2011, **158**, 1742.
- [9] Aditya Karanam, P.K. Sharma, and S. Ganju, *International Journal of Hydrogen Energy*, 2018, **43(36)**, 17492.
- [10] F. Ettner, K.G. Vollmer and T. Sattelmayer, *Journal of Combustion*, 2014, Article ID 686347, 1.
- [11] OpenFOAM (Developed and distributed by CFD Direct). <http://openfoam.org>
- [12] K.G. Vollmer, F. Ettner and T. Sattelmayer, *Combustion Science and Technology*, 2012, **184**, 1903.
- [13] L.R. Boeck, J. Hasslberger, F. Ettner, and T. Sattelmayer, *Proc. of the Seventh International Seminar on Fire & Explosion Hazards (ISFEH7)*, 2013.
- [14] Aditya Karanam, Vishnu Verma, Jayanta Chattopadhyay, RSD internal report, 2021, RSD/CSS/017/05/2021.



# **REVIEW ARTICLE**

**This page is intentionally left blank**

# Computational fluid dynamics modelling of solvent extraction equipment: A Review

K. K. Singh<sup>1,2,\*</sup>, Sourav Sarkar<sup>1,2</sup>, Nirvik Sen<sup>1</sup>, S. Mukhopadhyay<sup>1,2</sup>, K.T. Shenoy<sup>3</sup>

<sup>1</sup>Chemical Engineering Division, BARC, Mumbai-400085, India

<sup>2</sup>Homi Bhabha National Institute, Anushaktinagar, Mumbai-400094, India

<sup>3</sup>Chemical Engineering Group, BARC, Mumbai-400085, India

## Abstract

Solvent extraction is the most important separation process in nuclear fuel cycle. Different types of equipment are required for specific solvent extraction processes in the front-end and back-end of the nuclear fuel cycle. The complexity of the underlying phenomena (turbulent flow, multiphase flow, breakage and coalescence of droplets) renders design of solvent extraction equipment from first principles impossible. As a result, design of solvent extraction equipment is largely based on empirical correlations reported in literature, experimentation at different scales and operational experience. However, with availability of modelling tools like Computational Fluid Dynamics (CFD) and advancement in computational hardware, there is increasing thrust on thoroughly understanding the functioning of solvent extraction equipment aimed at optimal design, operation and scale-up. This article provides an overview of CFD modelling of solvent extraction equipment. The utility of single-phase CFD modelling in design of solvent extraction equipment which essentially involve multiphase flow is emphasized. Two-phase CFD modelling with the assumption of constant diameter monodispersed droplets is discussed along with the governing equations and summary of some studies reported in literature. The necessity of coupling CFD and population balance modelling to capture the phenomena of continuously occurring breakage and coalescence of droplets to predict drop size along with the flow field is discussed. The approaches of population balance modelling and their governing equations are summarized. The need of interface tracking simulations for some solvent extraction equipment is discussed. The trends in using CFD modelling to predict mass transfer in solvent extraction equipment are also discussed.

**Keywords:** CFD, CFD-PBM, droplet, Euler-Euler, population balance, solvent extraction

## Introduction

Solvent extraction is the most commonly used separation process in nuclear fuel cycle. The key processes using solvent extraction in nuclear fuel cycles are uranium refining, thorium processing, zirconium refining, and spent fuel reprocessing for closed fuel cycle [1, 2]. Solvent extraction is also used in several other processes of interest to the Department of Atomic Energy (DAE) such as production of rare-earth elements, value recovery from high level waste (HLW) for societal use, actinide partitioning in HLW, separation and purification of radioisotopes for radiopharmaceuticals and oncology [3-5].

Specific applications in nuclear fuel cycle require specific solvent extraction equipment. For example, one of the most important requirement of a solvent extraction equipment to be used in the back-end of the nuclear fuel cycle is that it should not have mechanical moving parts which require maintenance. This makes air pulsed columns very attractive for majority of applications in the back-end. However, in fast reactor fuel reprocessing, solvent degradation due to very high radiation field becomes the most important concern and the equipment which minimizes the contact time such as annular centrifugal extractor takes precedence over air pulsed column despite having part rotating at high speed. In the front-end of the nuclear fuel cycle, though maintenance is possible, passive equipment are still preferred. Another additional requirement a solvent extraction equipment has to fulfil to be worthy of deployment in the front-end is that it should be able to handle solids. The requirement of solid handling ability makes slurry extractor and pulsed disc and doughnut columns attractive in the front-end solvent extraction processes. In several applications in nuclear fuel cycle, the throughputs are too small which rule out the use of conventional solvent extraction equipment and special equipment that are ideal for low throughput applications such as Combine Air-lift Mixer-settler Unit (CALMSU) are required. On the contrary, in applications in which value has to be recovered from lean streams, very large throughputs are required which makes pump-mix mixer settlers and mechanically agitated columnar contactors such as rotating disc contactor (RDC) or asymmetric rotating disc contactor (ARDC) ideal. Thus, there is no solvent extraction equipment which can cater to all solvent extraction processes of interest in the nuclear fuel cycle.

The traditional way of designing solvent extraction equipment has been conducting experiments at bench-scale and pilot-scale and utilize the experimental data to design the equipment considering design margins. If conducting experiments is ruled

out, then the design is largely based on thumb rules and empirical correlations which have been reported extensively in literature for commonly used solvent extraction equipment. Operational experience with similar equipment is also heavily relied upon for designing solvent extraction equipment for new and/or scaled-up facilities. In most cases, the scale-up followed in new facilities is incremental. The overwhelming reliance on experimentation, thumb rules, empirical correlations and operational experience is attributed to complexity of phenomena such as turbulent flow, multiphase flow, continuous brakeage and coalescence of droplets which are prevalent inside a solvent extraction equipment and which render mathematical modelling of solvent extraction equipment quite complex. However, traditional way of designing leads to significant design margins which must be avoided to reduce the capital and operating costs. Thus, there is growing need of using modelling tools such as Computational Fluid Dynamics (CFD) to thoroughly and fundamentally understand phenomena underlying solvent extraction equipment leading to optimized designs and confident scale-up while minimizing experimentation.

In nuclear fuel cycle, CFD is routinely used for design and thermal hydraulic analysis of nuclear reactors. But the application of CFD in the front-end and back-end of the nuclear fuel cycle, in which solvent extraction is arguably the most important unit operation, has lagged behind. However, in recent years, lot of work has been done on CFD modelling of solvent extraction equipment a glimpse of which is provided in this article to give an overview of the approaches used for and utility of CFD modelling of solvent extraction equipment relevant for nuclear fuel cycle.

### Single-phase CFD modelling of solvent extraction equipment

Flow in a solvent extraction equipment is two-phase flow comprising of a liquid phase dispersed in another immiscible liquid phase. In some cases, three immiscible phases (for example, in air agitated liquid-liquid dispersion) or four immiscible phases (for example, in air agitated contactors in which feed contains solids) may also be present inside a solvent extraction equipment. The droplets in the liquid-liquid dispersion continuously undergo brakeage and coalescence. In addition to being two-phase or multiphase, flow is turbulent also. These complexities make CFD modelling of solvent extraction equipment quite complex. However, in several instances single-phase CFD modelling can help in design without going for very complex CFD model catering to all the phenomena prevalent in a solvent extraction equipment.

CFD-assisted design of mechanically agitated mixers and pump-mix mixers is a very pertinent example of how single-phase CFD simulations can be useful for design of solvent extraction equipment. A mechanically agitated mixer is the basic equipment in a solvent extraction cascade comprising of mixer-settlers. The conventional method to design a mixer requires estimate of specific power input which can be estimated if the power number of the impeller to be used is known. Power number of conventionally used impellers (such as Rushton turbine, straight blade paddle, pitched blade turbine, propeller) are reported in literature. However, the reported values are for a specific geometric setting. The power number varies with varying impeller diameter to tank diameter ratio ( $D/T$ ), impeller off-bottom clearance to tank diameter ratio ( $C/T$ ), the blade width to impeller diameter ratio ( $B_w/D$ ) etc. The dependence of power number on these geometric parameters can be significant. For example, on reducing  $C/T$ , a radial flow impeller such as Rushton turbine may start behaving as an axial flow impeller leading to a step reduction in power number on reducing the clearance [6]. The dependence of power number on the aforementioned geometric parameters is difficult to find in literature. Single-phase CFD simulations are very useful to estimate the power number of an impeller for such specific geometric setting.

In a mixer-settler cascade, the inter-stage pumping can be achieved by harnessing the pumping capacity of the rotating impeller itself instead of using inter-stage pumps. Such mixers, in which the impeller is expected to do the job of both mixing and inter-stage pumping, are called pump-mixers [7]. A mixer-settler based on pump-mixers is called pump-mix mixer-settler. The challenge in designing a pump-mix mixer is to identify a pump-mix

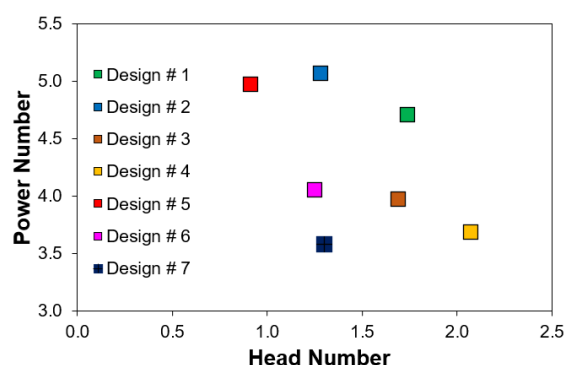


Fig.1: Power number and head number values of different designs of pump-mix mixers listed in Table 1.

**Table 1:** Different designs of pump-mix mixer for which single-phase CFD simulations were carried out to estimate head and power numbers as given in Fig. 1. (In all designs, the ratio of impeller diameter to tank diameter is 0.5,  $C/T$  represents impeller off-bottom clearance to tank diameter ratio,  $L_d/T$  represents the ratio of the length of the draft tube to tank diameter).

Type-1 pump-mix impeller: Top-shrouded turbine having radial trapezoidal blades		Type -2 pump-mix impeller: Top-shrouded turbine having non-radial rectangular blades	
Design No.	Impeller type	$C/T$	$L_d/T$
1	Type-1	0.5	250/700
2	Type-1	0.5	115/700
3	Type-1	0.3	115/700
4	Type-2	0.3	115/700
5	Type-1	0.5	-
6	Type-1	0.3	-
7	Type-2	0.3	-

impeller which does the dual job of mixing and pumping satisfactorily. This requires knowledge of the power number as well as head number of the pump-mix impeller. While power number data can be obtained from literature, the data on head number is almost non-existent. Also, the impellers used for pump-mix action are different from the impellers used for just mixing. For example, the pump-mix impeller are usually top-shrouded. The power number and head number data of such specialized impellers are not easily available in literature. Thus, single-phase CFD simulations for estimating power number and head number of pump-mix impeller being contemplated in design become very useful in designing a cascade of pump-mix mixer-settlers. For example, Fig.1 shows the power number and head number values predicted from single-phase CFD simulations of different designs of a pump-mix mixer described in Table 1. The pump-mix mixer (diameter = height = 700 mm) is to be designed to handle a total throughput of 4 m<sup>3</sup>/hr with a residence time of 4 minute. Different designs involve two different types of impellers placed inside the mixing tank differently. First 4 designs have the provision of draft tube which is required to increase the pumping head. Fig. 1 can help select an appropriate design for a given mixing and pumping tasks. For example, Design # 4 is suitable if very high pumping head is required with mild mixing, whereas Design # 1 is suitable if high pumping head is required with high degree of mixing.

When throughputs to be handled are very high, meeting the pumping requirement without causing excessive mixing becomes a design challenge. In such cases, the impeller is placed close to the

bottom of the mixer where the liquids are coming in. However, such a placement of impeller may cause poor mixing in the top part of the mixer causing the mixer to deviate from a well-mixed vessel. Single-phase CFD modelling can be used also to simulate the non-ideal mixing in such cases [7]. Single-phase CFD simulations of mixers and pump-mix mixer typically involve solving Reynolds Averaged Navier–Stokes (RANS) equations along with an appropriate set of equations to model turbulence. Standard k-ε model is the most commonly used model of turbulence. Modelling of rotating impeller poses some challenges but over the years several techniques have been developed and incorporated in CFD solvers [8].

Single-phase CFD simulations are useful not only for mechanically agitated solvent extraction equipment but also for columnar solvent extraction equipment. In columnar equipment, it has been reported in literature that axial dispersion in single-phase flow is higher than in two-phase flow. Thus, the use of single-phase axial dispersion coefficient estimated from single-phase CFD modelling in conventional design procedure to predict mass transfer performance of the columnar contactor can give a working design while avoiding rigorous and hence complex two-phase simulations. Some of the single-phase CFD studies on solvent extraction equipment are summarized in Table 2.

### Two-phase CFD modelling assuming monodispersed drops

The most common approach used to simulate liquid-liquid two-phase flow in a solvent extraction equipment is Euler-Euler

**Table 2:** Summary of some of the reported studies on single-phase CFD modelling of solvent extraction equipment. (PDDC: Pulsed Disc and Doughnut Column; APDDC: Annular Pulsed Disc and Doughnut Column; PSPC: Pulsed Sieve Plate Column; RDC: Rotating Disc Contactor)

Contactor	Turbulence model	Objectives
PDDC [9]	Standard $k-\epsilon$	Understanding flow patterns, estimation of pressure drop and axial dispersion coefficient
APDDC [10]	Standard $k-\epsilon$	Understanding flow pattern, estimation of pressure drop and axial dispersion coefficient
PDDC having different design of disc and doughnut type plates [11]	Standard $k-\epsilon$	Understanding flow patterns, estimation of Peclet number, shear rate, turbulent energy dissipation rate and pressure drop per unit length for different designs of disc and doughnut internals
PSPC [12]	Standard $k-\epsilon$	Understanding flow patterns, estimation of axial dispersion coefficient
Pump-mix mixer [13]	Standard $k-\epsilon$	Estimation of head and power characteristics of pump-mix mixers
Pump-mix mixers [14]	Standard $k-\epsilon$	Understanding flow patterns and estimation of head number, power number and prediction of RTD.
Pump-mix mixers [7]	Standard $k-\epsilon$	Estimation of head and power characteristics of different designs of pump-mix impellers, thoroughly understand pump-mix action
RDC [15]	Standard $k-\epsilon$ , RNG $k-\epsilon$ , realizable $k-\epsilon$ , RSM	Understanding flow patterns and comparison of different turbulence models
PDDC [16]	Standard $k-\epsilon$ , RNG $k-\epsilon$ , Low Re $k-\epsilon$ , RSM	Understanding flow patterns and comparison of different turbulence model
PDDC [17]	Standard $k-\epsilon$	Understanding flow patterns and estimation of axial dispersion coefficient.

approach. This approach is necessary as in a solvent extraction equipment the volume fraction of the dispersed phase is significant. In this approach, the continuity and momentum equations are solved separately for the dispersed phase and the continuous phase along with the equations of an appropriate model of turbulence. The equations of the continuous and dispersed phase are linked through the interphase momentum exchange term. The interphase momentum exchange in two-phase flow may be due to drag force, lift-force and added mass force. However, for liquid-liquid two-phase flow, drag force is considered the most important and in majority of two-phase CFD models of solvent extraction equipment reported in literature only drag force is considered to model interphase momentum exchange term. Similarly, mixture k-ε model is the most widely used turbulence model. In this model, turbulence is solved for the mixed phase rather than solving turbulence separately for individual phases using per-phase turbulence model. This helps in reduction in computational time. The Euler-Euler simulations require an estimate of drop diameter as drop diameter appears in the term used for quantification of the drag force. In reality, the diameter of the drops in a solvent extraction contactor is not constant as drops are continuously flowing and simultaneously undergoing breakage and coalescence. In fact, there always exists a drop size distribution. Thus, drop size distribution or at least average drop diameter should also be computed along with other flow variables. However, this approach is computationally demanding and often dispersed phase is assumed to have monodispersed drops having constant diameter.

Thus, the drop diameter becomes a user input to the CFD model. As expected, the results of the CFD simulations depend on how good is the estimate of the drop diameter. The drop diameter to be used in the simulations can be based on the experimental measurements or it may be estimated from a suitable correlation reported in literature [18, 19]. A drag coefficient model is necessary to estimate the drag force to model interphase momentum exchange. One of several drag coefficient models reported in literature or available in CFD solver can be used to model interphase momentum exchange in liquid-liquid two-phase flow. Most of the reported drag models and drag models available in CFD solvers are empirical in nature and several of them are based on a single solid particle settling in quiescent liquid. Strictly speaking, use of such drag models in two-phase CFD models of solvent extraction equipment is not advisable as these models do not account for the presence of swarm of droplets, effect of turbulence and effect of internal circulation in the drops on the drag coefficient. For want of drag models which should be used for turbulent swarm of internally circulating droplets, the drag models which are strictly not applicable for turbulent liquid-liquid dispersion continue to be used for two-phase CFD modelling of solvent extraction equipment. As expected, the choice of the drag model may significantly affect the results of Euler-Euler CFD simulations [18]. This limitation of two-phase CFD models of solvent extraction equipment should be addressed by using CFD modelling to understand the effect of turbulence, internal circulation and presence of other droplets on the drag force exerted by the continuous phase on a droplet.

**Table 3:** Typical governing equations used for Euler-Euler two-phase simulations of solvent extraction equipment

$\nabla \cdot (\phi_a \vec{u}_a + \phi_c \vec{u}_c) = 0$		(1)
$\frac{\partial \phi_a}{\partial t} + \nabla \cdot (\phi_a \vec{u}_a) = \nabla \cdot D_{m,d} \nabla \phi_a$	Continuity equations	(2)
$\rho_c \frac{\partial \vec{u}_c}{\partial t} + \rho_c (\vec{u}_c \cdot \nabla) \vec{u}_c = \nabla \cdot [-p \vec{I} + \vec{\tau}_c] + \frac{\nabla \phi_c}{\phi_c} \vec{\tau}_c + \rho_c \vec{g} + \frac{\vec{F}_{m,c}}{\phi_c}$	Momentum equation of the continuous phase	(3)
$\rho_a \frac{\partial \vec{u}_a}{\partial t} + \rho_a (\vec{u}_a \cdot \nabla) \vec{u}_a = \nabla \cdot [-p \vec{I} + \vec{\tau}_a] + \frac{\nabla \phi_a}{\phi_a} \vec{\tau}_a + \rho_a \vec{g} + \frac{\vec{F}_{m,d}}{\phi_a}$	Momentum equation of the dispersed phase	(4)
$\vec{\tau}_c = (\mu_c + \mu_T) \left( \nabla \vec{u}_c + (\nabla \vec{u}_c)^T - \frac{2}{3} (\nabla \cdot \vec{u}_c) \vec{I} \right) - \frac{2}{3} \rho_c k \vec{I}$	Closure for the continuous phase momentum equation	(5)
$\vec{\tau}_a = (\mu_a + \mu_T) \left( \nabla \vec{u}_a + (\nabla \vec{u}_a)^T - \frac{2}{3} (\nabla \cdot \vec{u}_a) \vec{I} \right) - \frac{2}{3} \rho_a k \vec{I}$	Closure for dispersed phase momentum equation	(6)
$\vec{F}_{m,c} = \chi (\vec{u}_a - \vec{u}_c)$	Equation for interphase force	(7)
$\chi = \frac{3 \phi_a \phi_c \rho_c C_d  u_a - u_c }{4 d_{32}}$	Interphase exchange term	(8)
$C_d = \max \left\{ \frac{24}{Re_p} (1 + 0.15 Re_p^{0.687}); 0.44 \right\}$	Equation for drag coefficient	(9)
$Re_p = \frac{\phi_c d_{32} \rho_c  \vec{u}_a - \vec{u}_c }{\mu_c}$	Drop Reynolds number	(10)
$\rho_m \frac{\partial k}{\partial t} + \rho_m (\vec{u}_m \cdot \nabla) k = \nabla \cdot \left[ \left( \mu_m + \frac{\mu_T}{\sigma_k} \right) \nabla k \right] + P_k - \rho_m \varepsilon$	Transport equation of turbulent kinetic energy for mixture k-ε model	(11)
$\rho_m \frac{\partial \varepsilon}{\partial t} + \rho_m (\vec{u}_m \cdot \nabla) \varepsilon = \nabla \cdot \left[ \left( \mu_m + \frac{\mu_T}{\sigma_\varepsilon} \right) \nabla \varepsilon \right] + C_{1\varepsilon} \frac{\varepsilon}{k} P_k - C_{2\varepsilon} \rho_m \frac{\varepsilon^2}{k}$	Transport equation of turbulent energy dissipation rate for mixture k-ε model	(12)
$\rho_m = \phi_c \rho_c + \phi_a \rho_a$	Mixture density for use in mixture k-ε model	(13)
$\vec{u}_m = \frac{\phi_c \rho_c \vec{u}_c + \phi_a \rho_a \vec{u}_a}{\phi_c \rho_c + \phi_a \rho_a}$	Mixture velocity for use in mixture k-ε model	(14)
$\mu_T = \rho_m C_\mu \frac{k^2}{\varepsilon}$	Equation to estimate turbulent viscosity	(15)
$P_k = \mu_T \left[ \nabla \vec{u}_m : (\nabla \vec{u}_m + (\nabla \vec{u}_m)^T) - \frac{2}{3} (\nabla \cdot \vec{u}_m)^2 \right] - \frac{2}{3} \rho_m k \nabla \cdot \vec{u}_m$	Source term for turbulent kinetic energy in mixture k-ε model	(16)

$\phi_a$ : dispersed phase volume fraction;  $\vec{u}_a$ : dispersed phase velocity vector;  $\phi_c$ : continuous phase volume fraction;  $\vec{u}_c$ : continuous phase velocity vector;  $t$ : time;  $\vec{I}$ : Identity tensor;  $\vec{F}_{m,c}$ : Volumetric interphase force on continuous phase;  $\vec{F}_{m,d}$ : Volumetric interphase force on dispersed phase;  $\vec{\tau}_c$ : Continuous phase stress tensor;  $\vec{\tau}_a$ : Dispersed phase stress tensor;  $D_{m,d}$ : Turbulent dispersion coefficient;  $\mu_c$ : Continuous phase viscosity;  $\mu_a$ : Dispersed phase viscosity;  $\mu_T$ : Turbulent viscosity;  $p$ : Pressure;  $\vec{g}$ : Acceleration due to gravity;  $\rho_c$ : Continuous phase density;  $\rho_a$ : Dispersed phase density;  $C_d$ : Drag coefficient;  $Re_p$ : Droplet Reynolds number;  $P_k$ : Rate of generation of turbulent kinetic energy;  $d_{32}$ : Sauter mean drop diameter;  $k$ : Turbulent kinetic energy;  $\varepsilon$ : Turbulent energy dissipation rate;  $\vec{u}_m$ : Mixture velocity;  $\rho_m$ : Mixture density;  $C_{1\varepsilon}$ ,  $C_{2\varepsilon}$ ,  $C_\mu$ ,  $\sigma_k$ ,  $\sigma_\varepsilon$ : Constants of mixture k-ε model of turbulence.



Table 3 lists the equations typically solved in Euler-Euler CFD model of a solvent extraction equipment. CFD simulations based on Euler-Euler approach assuming monodispersed droplets can help estimate spatial variations and average value of dispersed phase holdup. With drop diameter known, specific interfacial area can be estimated by using dispersed phase holdup. With specific interfacial area and dispersed phase holdup known, mass transfer can be estimated by using suitable correlations of mass transfer coefficient along with thermodynamic data. In case, the equipment is suspected to have significant deviation from ideal flow behaviour (which is the case more often than not), virtual residence time distribution experiments can also be carried out using CFD modelling to predict axial dispersion coefficient of the continuous phase and dispersed phase. This requires solving species transport equations for each phase. If the flow is steady, the

species transport can be solved without simultaneously solving the flow field. In such case, the CFD simulations will comprise of two steps. In the first step, flow is solved and in the second step the species transport equations are solved utilizing the flow field solved in the first step. If the flow is inherently transient, as in air pulsed columns, species transport equations need to be simultaneously solved along with two-phase flow equations.

As an illustration, Fig. 2 shows the results of Euler-Euler two-phase simulations of Pulsed Disc and Doughnut Column (PDDC) reported in a recent study [20]. The study reported two-phase CFD modelling of PDDC using Euler-Euler approach assuming monodispersed drops to predict flow field and dispersed phase holdup. Drop diameter used in the CFD model was estimated from a correlation reported in literature. Further,

**Table 4:** Summary of some of the reported studies on Euler-Euler approach based two-phase CFD modelling of solvent extraction equipment assuming monodispersed drops. (RDC: Rotating Disc Contactor, ARDC: Asymmetric Rotating Disc Contactor, ARIC: Asymmetric Rotating Impeller Contactor)

Contactors	Turbulence model	Source of drop diameter	Drag model	Objective
PSPC [18]	mixture $k-\epsilon$	Experimental data	Schiller–Naumann, Morsi–Alexander, Symmetric, Barnea–Mizrahi, Kumar–Hartland, Augier et al.	Estimation of dispersed phase holdup
PSPC [19]	mixture $k-\epsilon$	Correlation	Kumar–Hartland, modified Kumar–Hartland	Estimation of dispersed phase holdup
PDDC [20]	mixture $k-\epsilon$	Correlation	Schiller–Naumann	Estimation of dispersed phase holdup
PDDC [21]	mixture $k-\epsilon$	Correlation	Schiller–Naumann	Estimation of dispersed phase holdup and Peclet number of both phases
RDC [15]	Realizable $k-\epsilon$ , RSM	Experimental data	Schiller–Naumann	Understanding flow pattern and comparison of turbulence models
APDDC [22]	mixture $k-\epsilon$	Experimental data	Ishii and Zuber	Estimation of dispersed phase holdup
APDDC [23]	mixture $k-\epsilon$	Experimental data	Ishii and Zuber	Estimation of dispersed phase holdup and axial dispersion coefficient of continuous phase
ARDC, ARIC [24]	mixture $k-\epsilon$	Experimental data	Kumar–Hartland	Estimation of dispersed phase holdup
RDC [25]	Realizable $k-\epsilon$	Experimental data	Schiller–Naumann	Estimation of dispersed phase holdup
Hybrid PSPC [26]	Realizable $k-\epsilon$	Experimental data	Schiller–Naumann	Estimation of dispersed phase holdup and axial dispersion coefficient of continuous phase

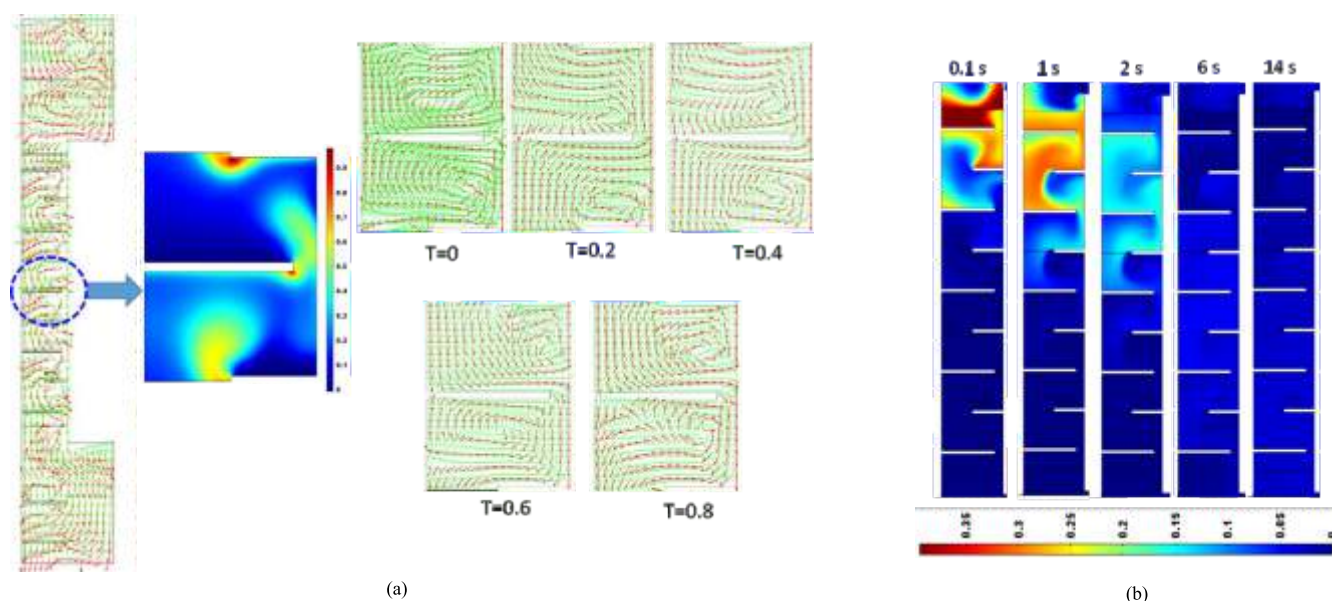


**Fig. 2:** (a) Typical velocity vectors of continuous and dispersed phase, dispersed phase holdup profile in an inter-disc space and velocity vectors of both phases in an inter-disc space at different instants of a pulsing cycle, (b) Typical progression of tracer in the computational domain with time in CFD-based RTD studies. “Reprinted with permission from {Sarkar et al., CFD modelling of pulsed disc and doughnut columns: prediction of axial dispersion in two-phase flow, Industrial & Engineering Chemistry Research, 2019, 58, 33, 15307-15320}. Copyright {2019} American Chemical Society.”

it also reported solution of species transport equation along with the equations of Euler-Euler approach to obtain residence time distribution (RTD) of the continuous phase for estimation of axial dispersion coefficient or Peclet number of the continuous phase. Validation was done by comparing predicted and experimentally measured dispersed phase holdup, residence time distribution and Peclet number of the continuous phase for different dispersed phase velocities, continuous phase velocities and pulsing velocities. Table 4 summarizes some of the two-phase CFD studies on Euler-Euler simulations of solvent extraction equipment carried out by assuming monodispersed droplets.

### Computational Fluid Dynamics – Population Balance Modelling

The CFD modelling approach discussed in the previous section is based on the assumption of monodispersed drops. Though, the assumption is often essential to simplify CFD model and reduce computational time, with this assumption phenomena of breakage and coalescence of drops which occur everywhere inside a solvent extraction equipment are not captured. The CFD model can be improved by doing away with this assumption by solving population balance equations along with the flow equations. This modelling approach is called as Computational Fluid Dynamics – Population Balance (CFD-PB) modelling. The modelling approach is schematically shown in Fig. 3. The solution of flow equations provides local values of the velocities of the two phases, dispersed phase holdup and turbulent energy dissipation rate which are utilized for solution of population balance equations. Solution of population balance equations provides local drop size distribution which can be used to obtain local value of an average diameter (most often Sauter mean diameter) which is used in the interphase momentum exchange term of the momentum equations of the Euler-Euler model. There are two widely used methods to solve the population balance equations. The first method is the method of classes. In the method of classes, the expected size range of the drops (e.g. 0-2000  $\mu\text{m}$ ) is divided into several classes. Each class has a size range and all the drops having size in that range are assumed to have a single size (representative class size). A population balance equation is solved for each class along with the equations of the Euler-Euler CFD model summarized in Table 3. The population balance equation for the drops having class diameter  $L$  is given in Table 5. The population balance equation is essentially a convection-diffusion equation with source and sink terms. The diffusion is often

neglected. The source terms correspond to the generation of drops of that particular class due to breakage of drops of larger diameter classes and coalescence of the droplets of smaller diameter classes. The sink terms are due to loss of drops of the drop class because of their breakage and coalescence with drops of other drop classes. The source and sink terms require the kernels of breakage rate, coalescence rate and daughter droplet distributions. These kernels, based on empirical or semi-empirical models, are reported in literature [27]. Table 6 lists a set of often-used kernels. The solution of population balance equation gives the population of droplets in each class and hence the drop size distribution which can be used to obtain average droplet diameter. Sauter mean diameter is often used as the average droplet diameter. The Sauter mean diameter is used in the interphase momentum exchange term of the two-phase flow equations. The turbulent energy dissipation rate and dispersed phase holdup obtained from CFD simulations are used in the population balance equations. The method of classes is computationally expensive as one additional equation is solved along with two-phase flow equations for each drop class considered. For example, 10 additional equations will be solved along with the two-phase flow equations if the droplet size range expected in the solvent extraction equipment is discretized into 10 drop classes. To overcome this, another method called as the method of moments is used to solve the population balance. In this method, the transport equations of the moments of the drop size distribution are solved instead of the transport equations for the number density of the droplets. The typical equations of the method of moments are given in Table 7. This approach is computationally less expensive than the method of classes as only first three moments of the drop size distribution are of practical significance. Thus, only three equations representing the first three moments of the drop size distribution need to be solved along with the flow equations. The Sauter mean diameter to be used in the momentum equations can be obtained from the ratio of the third and the second moments of the drop size distribution. As in the method of classes, in the method of moments too, the source and sink terms representing breakage and coalescence are present in the transport equations.

CFD-PB model helps predict dispersed phase holdup, drop size and hence specific interfacial area. Axial dispersion coefficient can also be estimated by solving species transport along with the equations of CFD-PB model. Thus, CFD-PB model can provide estimates of all hydrodynamic variables which are required to predict mass transfer performance of a solvent extraction equipment. Population balance is an area of extensive research. Several new approaches to solve population balance equations in computationally efficient manner have been reported [28, 29].

Fig. 4 shows some results from a recently reported study on CFD-PB modelling of pulsed sieve plate column [30]. Method of classes was used for solving population balance equations. Validation was done by comparing predicted and measured dispersed phase holdup and Sauter mean drop diameter for different pulsing velocities and dispersed phase velocities. Validated CFD-PB model was used to have detailed insights into two-phase hydrodynamics such as axial variation of Sauter mean diameter and turbulent energy dissipation rate and spatial variations of Sauter mean diameter, turbulent energy dissipation rate, turbulent intensity, coalescence rate, Kolmogorov length scale between two sieve plates (shown in Fig. 4). Table 8 summarize some of the studies in which CFD-PB modelling of solvent extraction equipment has been reported. The approach

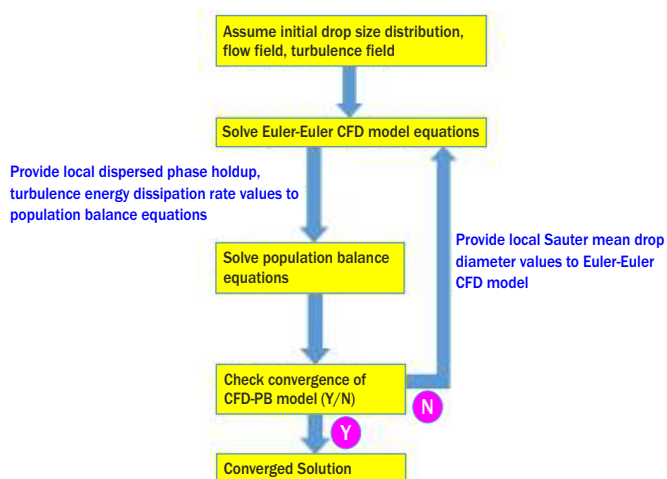


**Fig. 3:** Schematic of workflow in a CFD-PB model of solvent extraction equipment

**Table 5:** Typical population balance equation solved along with Euler-Euler CFD model in method of classes to predict drop size distribution [30].

$\frac{\partial}{\partial t}\{n(L; t)\} + \nabla \cdot (\vec{u}_d \cdot n(L; t)) = B^b - D^b + B^c - D^c$	Convection-diffusion equation of population of drops of diameter $L$	(17)
$B^b = \int_L^\infty \nu(\lambda)\beta(L \lambda)a(\lambda) n(\lambda; t)d\lambda$	Source term for the birth of drops of diameter $L$ due to breakage of larger drops	(18)
$D^b = a(L)n(L; t)$	Sink term for the death of drops of diameter $L$ due to breakage	(19)
$B^c = \int_0^{L/\sqrt[3]{2}} h\{(L^3 - \lambda^3)^{1/3}, \lambda\}n\{(L^3 - \lambda^3)^{1/3}, t\}n(\lambda; t)d\lambda$	Source term for the birth of drops of diameter $L$ due to coalescence of smaller drops	(20)
$D^c = n(L; t) \int_0^\infty h(L, \lambda)n(\lambda; t)d\lambda$	Sink term for the death of drops of diameter $L$ due to coalescence with drops of other sizes	(21)
$d_{32} = \frac{\int_0^\infty L^3 n(L; t)dL}{\int_0^\infty L^2 n(L; t)dL}$	Expression to evaluate Sauter mean diameter from drop size distribution.	(22)
<p><math>n(L; t)</math>: Number of drops of diameter <math>L</math> at time <math>t</math> per unit volume of dispersion; <math>\vec{u}_d</math>: Dispersed phase velocity vector; <math>t</math>: time; <math>B^b</math>: Source term for birth of drops of diameter <math>L</math> due to breakage of larger drops; <math>D^b</math>: Sink term for death of drops of diameter <math>L</math> due to their breakage into smaller drops; <math>B^c</math>: Source term for birth of drops of diameter <math>L</math> due to coalescence of smaller drops; <math>D^c</math>: Sink term for death of drops of diameter <math>L</math> due to coalescence with other drops; <math>a(L)</math>: Breakage rate of drops of diameter <math>L</math>; <math>h(L, \lambda)</math>: Coalescence rate of droplets of diameter <math>L</math> and <math>\lambda</math>; <math>\beta(L \lambda)</math>: Distribution of daughter drops produced due to breakage of a drop of size <math>\lambda</math>; <math>d_{32}</math>: Sauter mean drop diameter; <math>\nu(\lambda)</math>: number of drops formed due to breakage of a drop of diameter <math>\lambda</math>.</p>		

**Table 6:** Typical breakage, coalescence and daughter droplet distribution models used to define the source and sink terms of population balance equation [31].

$a(L) = C_1 \frac{\varepsilon^{1/3}}{(1 + \phi_d)L^{2/3}} \exp \left\{ -C_2 \frac{\sigma(1 + \phi_d)^2}{\rho_d \varepsilon^{2/3} L^{5/3}} \right\}$	Breakage rate kernel defining rate of breakage of drops of diameter $L$	(23)
$h(L, \lambda) = \gamma(L, \lambda)\eta(L, \lambda)$	Coalescence rate kernel defining the rate of coalescence between drops of size $L$ and $\lambda$ . This is a product of collision rate and coalescence efficiency.	(24)
$\gamma(L, \lambda) = \left[ C_3 \frac{\varepsilon^{1/3}}{(1 + \phi_d)} (L + \lambda)^2 (L^{2/3} + \lambda^{2/3})^{1/2} \right]$	Collision rate to model the rate of collision between droplets of size $L$ and $\lambda$	(25)
$\eta(L, \lambda) = \exp \left\{ -C_4 \frac{\mu_c \rho_c \varepsilon}{\sigma^2 (1 + \phi_d)^3} \left( \frac{L\lambda}{L + \lambda} \right)^4 \right\}$	Coalescence efficiency kernel to estimate the fraction of collisions between drops of size $L$ and $\lambda$ resulting in coalescence	(26)
$\beta(L \lambda) = 30 \left( \frac{L^3}{\lambda^3} \right) \left( 1 - \frac{L^3}{\lambda^3} \right)$	Distribution of daughter drops produced due to breakage of a drop of diameter $\lambda$	(27)
<p><math>\varepsilon</math>: Turbulent energy dissipation rate; <math>\sigma</math>: Interfacial tension; <math>C_1</math>-<math>C_4</math>: Constants in the breakage rate, collision rate and coalescence efficiency kernels.</p>		

**Table 7:** Typical equations solved along with Euler-Euler CFD model to predict drop size distribution by using method of moments [32].

$\frac{\partial m_k}{\partial t} + \nabla \cdot (-D_T \nabla m_k + \overline{u_d} m_k) = S_k^{bb} + S_k^{bc} - S_k^{db} - S_k^{dc}$	The transport equation for $k^{\text{th}}$ moment of the drop size distribution	(28)
$m_k = \int_0^{\infty} n(L) L^k dL$	Equation to evaluate $k^{\text{th}}$ moment of the drop size distribution	(29)
$S_k^{bb} = \int_0^{+\infty} L^k \int_0^{+\infty} a(\lambda) \beta(L \lambda) n(\lambda) d\lambda dL$ $S_k^{bc} = \frac{1}{2} \int_0^{+\infty} n(\lambda) \int_0^{+\infty} h(q, \lambda) (q^3 + \lambda^3)^{k/3} n(q) dq d\lambda$ $S_k^{db} = \int_0^{+\infty} L^k a(L) n(L) dL$ $S_k^{dc} = \int_0^{+\infty} L^k n(L) \int_0^{+\infty} h(L, \lambda) n(\lambda) d\lambda dL$	Source and sink terms of the transport equation of the $k^{\text{th}}$ moment	(30)
$d_{32} = \frac{m_3}{m_2}$	Equation to obtain Sauter mean drop diameter from the moments of the drop size distribution.	(31)
<p><math>m_k</math>: <math>k^{\text{th}}</math> moment of drop size distribution; <math>t</math>: Time; <math>D_T</math>: Turbulent dispersion coefficient of the dispersed phase; <math>\overline{u_d}</math>: Dispersed phase velocity; <math>S_k^{bb}</math>: Source term for birth due to breakage; <math>S_k^{bc}</math>: Source term for birth due to coalescence; <math>S_k^{db}</math>: Sink term for death due to breakage; <math>S_k^{dc}</math>: Sink term for death due to coalescence; <math>a(L)</math>: Breakage rate of drops of diameter <math>L</math>; <math>h(q, \lambda)</math>: Coalescence rate of drops of diameter <math>q</math> and <math>\lambda</math>; <math>\beta(L \lambda)</math>: Distribution of daughter drops produced due to breakage of a drop of diameter <math>\lambda</math>; <math>n(L)</math>: Number of droplet of size <math>L</math> per unit volume; <math>d_{32}</math>: Sauter mean drop diameter.</p>		

**Table 8:** Summary of some of the reported studies on CFD-PB modelling of solvent extraction equipment

Contactors	Turbulence model	PBM approach	Drag model	Objective
PSPC [30]	mixture $k-\epsilon$	Method of classes	Kumar-Hartland	Estimation of $d_{32}$ and dispersed phase holdup
PDDC [32]	mixture $k-\epsilon$	Quadrature Method of Moments (QMOM)	Schiller-Naumann	Estimation of $d_{32}$ and dispersed phase holdup
PSPC [33]	mixture $k-\epsilon$	Method of classes	Modified Schiller-Naumann	Estimation of $d_{32}$ , dispersed phase holdup and axial dispersion
PDDC [34]	mixture $k-\epsilon$	Method of classes	Ishii-Zuber	Estimation of $d_{32}$ and dispersed phase holdup. The breakage kernel obtained in a previous work by the authors was implemented in PBM.
PDDC [35]	mixture $k-\epsilon$	Method of classes	Ishii-Zuber	Estimation of drop size distribution in PDDC after modifying PBM to account for the presence of liquid layer on wettable discs and doughnuts.
PDDC [36]	mixture $k-\epsilon$	Method of classes	Ishii-Zuber	Determination of droplet breakup frequency and daughter droplet size distribution functions in a small computational domain using level-set method and subsequently implement them in a CFD-PBM of full-scale PDDC.
Pump-mixer [37]	mixture $k-\epsilon$	Method of classes	Schiller-Naumann	Understanding the flow pattern and estimation of dispersed phase holdup and Sauter mean drop diameter
Continuous stirred settler [38]	mixture $k-\epsilon$	QMOM	Morsi-Alexander	Estimation of dispersion band thickness
PDDC [39]	mixture $k-\epsilon$	QMOM	Schiller-Naumann	Estimation of $d_{32}$
RDC [40]	mixture $k-\epsilon$	Method of classes & QMOM	Schiller-Naumann	Estimation of $d_{32}$ and dispersed phase holdup

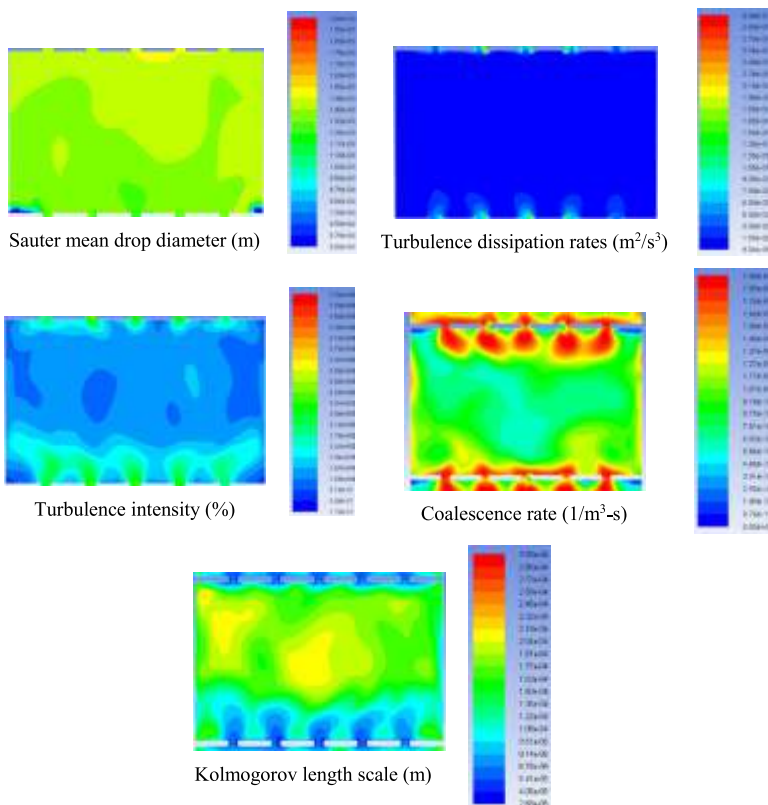


**Table 8:** Spatial variation of Sauter mean drop diameter, turbulence dissipation rate, turbulence intensity, coalescence rate and Kolmogorov length scale in an interplate space ( $A_{mf} = 0.02$  m/s;  $v_d = 0.004$  m/s,  $v_c = 0.00207$  m/s) “Reprinted from Progress in Nuclear Energy, 111, Nirvik Sen, K.K. Singh, A.W. Patwardhan, S. Mukhopadhyay, K.T. Shenoy, CFD-PBM simulations of a pulsed sieve plate column, 125-137, Copyright (2019), with permission from Elsevier”.

obtained using high-speed flow imaging and Laser Doppler Velocimetry (LDV) measurements. Subsequently, similar simulations to understand the effect of geometry of the mixing vanes at the bottom of the stationary bowl on hydrodynamics in ACE were reported. VOF method was used along with LES model of turbulence to track the air-water interface and capture turbulent flow field in the annular gap [42].

Recently, advanced computational approaches to simulate flow in solvent extraction equipment are being explored and reported. In a very recent study, the proof-of-concept of a novel modelling approach for ACE was reported [43]. This approach called GEneralized Multifluid Modelling Approach (GEMMA) is a hybrid approach which toggles between multifluid model (Euler-Euler type of model) and VOF kind of model for small-scale dispersed flow and large-scale segregated flow, respectively. One Secondary Particle Method (OSPM) was also coupled with CFD model.

Interface tracking simulations have also been reported for micro-scale solvent extraction slug contactors in which prediction of the flow regime (slug flow, droplet flow, parallel flow etc.) is important [44].

### CFD modelling of mass transfer in solvent extraction equipment

Though the ultimate objective of a solvent extraction equipment is to ensure interphase mass transfer, most of the literature on CFD modelling of solvent extraction equipment is limited to flow simulations. The studies on CFD modelling of mass transfer in solvent extraction equipment, particularly, the ones which involve liquid-liquid dispersion are very few. While majority of large-scale solvent extraction equipment involve mass transfer in dispersive mode, equipment such as hollow fiber modules can be made to operate to achieve liquid-liquid mass transfer in non-dispersive mode. Two non-dispersive modes of operation of hollow fibre modules are solvent extraction mode and supported liquid membrane mode of operation. In solvent extraction mode of operation, the feed flows through the lumens of the hollow fiber whereas the solvent phase flows through the shell. The pores of the lumens are impregnated with the solvent phase flowing on the shell side. The solvent phase impregnated in the pores of the lumens facilitates mass transfer of the desired solute from the feed flowing in the lumen to the solvent flowing in the shell. In supported liquid mode of operation, the aqueous feed flows in the lumens and an aqueous strip phase flows in the shell side while the solvent phase fills the pores of the lumens of the hollow fibre. The mass transfer of the solute from the feed to the strip phase takes place through the solvent phase impregnated in the pores of the lumens. CFD modelling of mass transfer in hollow fibre module involves single-phase simulations of laminar flow of the aqueous phase and solvent/strip phase in the lumen and shell side, respectively. Mass transfer is simulated by solving convection-diffusion equations for the feed, shell sides and diffusion equation in the solvent phase impregnated in the pores of the lumen after applying complex boundary conditions of flux continuity and concentration jump at the feed side-lumen pore and lumen pore-shell side interfaces [45, 46]. Thus, the complexity in CFD simulation lies not in the governing equations but in implementation of the boundary conditions. As a result, the simulations of non-dispersive flow in hollow fibre are simpler than

used for CFD modelling in majority of these studies is Euler-Euler approach.

### Interface tracking simulations of solvent extraction equipment

While most of the studies reported on CFD modelling of solvent extraction equipment can be classified in the categories described in the previous sections, there are several studies which do not fall in one of the above-mentioned categories. Though in most of the solvent extraction equipment, the flow is dispersed flow and the active volume of the equipment (the volume in which liquid-liquid dispersion is present) is known. However, in some equipment, the active volume is not constant but may vary depending on the operating conditions. Annular centrifugal extractor (ACE) is an example of such a contactor. In an ACE, the dispersion and mass transfer take place in the annular gap between a stator and a rotor. However, the volume present in the annular space is not fixed and may depend on several factors, the most important being the rotor speed and flow rates of the two liquid phases. To estimate liquid holdup in the annular gap, tracking of the free-surface (gas-liquid interface) in the annular gap is required. This can be done by using an interface tracking method like Volume of Fluid (VOF) method. There are several reported studies in which VOF model has been used for tracking the air-liquid interface in an ACE. Wardle and co-workers used VOF method to simulate gas-liquid flow in the annular gap of an annular centrifugal extractor considering only water as the liquid flowing through the centrifugal extractor [41]. Different turbulence models (RNG *k*- model, large eddy simulation method, and the detached eddy simulation) were compared. The experimental data was

simulations of dispersed flow in conventional solvent extraction equipment in which governing equations are complex but boundary conditions are simpler. Like hollow fibres, CFD modelling of mass transfer in microcontactors have also been reported. Such simulations typically involve a single entity (slug or drop) having continuous phase in its surrounding as the computational domain. Very small computational domain along with the fact that flow in a microcontactor is usually laminar make the simulations of liquid-liquid mass transfer in microcontactor relatively simpler. However, CFD modelling of mass transfer in conventional equipment which involve liquid-liquid dispersion are very few [47, 48]. This is primarily due to complexity in implementing additional species transport equations having source/ sink terms representing interphase mass transfer along with already complex flow equations and the equations of turbulence model. Also, such model requires overall mass transfer coefficient for which one of the several empirical models reported in literature can be used. The mass transfer prediction from the CFD model thus significantly depend on the choice of the mass transfer coefficient model.

As mentioned in the introduction section, some of solvent extraction equipment involve gas-liquid-liquid or gas-liquid-liquid-solid flows. Literature on CFD modelling of such solvent extraction equipment is practically non-existent.

## Conclusions

The article provides an overview of approaches used for CFD modelling of solvent extraction equipment. Though the flow in a solvent extraction equipment is two-phase flow or multiphase flow, in some cases single-phase CFD modelling can provide useful data required for design. A pertinent example is design of pump-mix mixer in which single-phase CFD modelling can be used to design pump-mix impellers to meet the dual requirement of pumping and mixing in a mixer-settler cascade. Single-phase CFD simulation can also be used for performing virtual residence time distribution experiments to quantify and understand the deviation from ideal flow behaviour.

Two-phase CFD modelling of liquid-liquid dispersed flow assuming monodispersed droplets represents the next higher level of difficulty in CFD modelling of solvent extraction equipment. Euler-Euler method is the most widely used method whereas mixture k- $\epsilon$  model of turbulence is the most widely used model of turbulence for two-phase CFD modelling of solvent extraction equipment. The drag force is assumed to be the most important contributor to interphase momentum exchange. The results of CFD model may depend on the selection of drag model and this is the main source of empiricism in the two-phase CFD model of solvent extraction equipment.

Coupling of two-phase CFD modelling with population balance modelling leading to CFD-PB model is required if the assumption of constant diameter monodispersed drops is to be done away with to realistically model breakage and coalescence of drops which occur continuously in a solvent extraction equipment. Two approaches of population balance modelling – method of classes and method of moments – are briefly discussed. The flow field and drop size predicted by CFD-PB model depend on the models selected for breakage rate, coalescence rate and daughter droplet distribution and the values of the constants in these models. This

necessitates a careful selection of these models and validation of CFD-PB model with experimental data.

While above-mentioned modelling approaches cover the vast majority of studies on CFD modelling of solvent extraction equipment, some special class of equipment such as annual centrifugal extractors which do not have fixed active volume or microcontactors in which dispersed phase may have size of the order of the diameter of the contactor may require interface tracking simulations. Such simulations are briefly discussed.

Though the ultimate objective of using a solvent extraction equipment is to achieve mass transfer, CFD modelling of mass transfer in solvent extraction equipment are scant. This is attributed to the complexities introduced due to solution of additional equations required to model mass transfer and also in conducting mass transfer experiments which require once through flow unlike the flow experiments which are generally closed loop. However, CFD modelling of mass transfer in equipment which work on the principle of non-dispersive flow such as hollow fibre contactor or microcontactors, in which it is possible to simulate mass transfer with a single entity of the dispersed phase (e.g. a single slug or droplet) rather than a swarm of dispersed phase entities, have been reported. This is due to significant reduction in the complexity of the governing equations to be solved or reduction in the size of the computational domain.

Like in any other field, advances in the field of CFD modelling of solvent extraction are taking place such as development of hybrid models suitable for multiscale flows as in an annular centrifugal extractor, reduced population balance model to make computations faster and fundamental understanding of the phenomena of drag, droplet breakage, droplet coalescence in the quest for minimizing empiricism in equipment level CFD modelling.

## Corresponding Author\*

K.K. Singh (kksingh@barc.gov.in)

## References

- [1] H. Singh, and C.K. Gupta, *Mineral Processing and Extractive Metallurgy Review*, 2000, **21**,(1-5), 307.
- [2] R. Natarajan, *Progress in Nuclear Energy*, 2017, **101**, 118.
- [3] P. Sinharoy, D. Banerjee, S. Manohar, and C.P. Kaushik, *Separation Science and Technology*, 2021, **56**(8), 1450-1456.
- [4] S. Manohar, J.N. Sharma, B.V. Shah, and P.K. Wattal, *Nuclear Science and Engineering*, 2007, **156**(1), 96-102.
- [5] N.V. Thakur, *Mineral Processing and Extractive Metallurgy Review*, 2000, **21**(1-5), 277-306.
- [6] K.K. Singh, K.T. Shenoy, A.K. Mahendra, and S.K. Ghosh, *Chemical Engineering Science*, 2004, **59**(14), 2937-2945.
- [7] K.K. Singh, S.M. Mahajani, K.T. Shenoy, and S.K. Ghosh, *AIChE Journal*, 2008, **54**(1), 42-55.
- [8] A. Brucato, M. Ciofalo, F. Grisafi, and G. Micale, *Chemical Engineering Science* 1998, **53**(21), 3653-3684.
- [9] S. Sarkar, K.K. Singh, and K.T. Shenoy, *Separation Science and Technology*, 2017, **52**(18), 2863-2877.

- [10] S. Sarkar, K.K. Singh, and K.T. Shenoy, *Progress in Nuclear Energy*, 2018, **106**, 335-344.
- [11] S. Sarkar, K.K. Singh, and K.T. Shenoy, *Chemical Engineering and Processing-Process Intensification*, 2020, **155**, 108052.
- [12] N. Sen, K.K. Singh, A.W. Patwardhan, S. Mukhopadhyay, and K.T. Shenoy, *Separation Science and Technology*, 2015, **50(16)**, 2485-2495.
- [13] K.K. Singh, S.M. Mahajani, K.T. Shenoy, A.W. Patwardhan, and S.K. Ghosh, *Chemical Engineering Science*, 2007, **62**, 1308-1322.
- [14] K.K. Singh, S.M. Mahajani, K.T. Shenoy, and S.K. Ghosh, *Industrial and Engineering Chemistry Research*, 2007, **46**, 2180-2190.
- [15] C. Drumm, and H.-J. Bart, *Chemical Engineering and Technology*, 2006, **29(11)**, 1297-1302.
- [16] A. Amokrane, S. Charton, F. Lamadie, J.F. Paisant, and F. Puel, *Chemical Engineering Science*, 2014, **114**, 40-50.
- [17] M.A. Nabli, P. Guiraud, and C. Gourdon, *Chemical Engineering Science*, 1997, **52(14)**, 2353-2368.
- [18] N. Sen, K.K. Singh, A.W. Patwardhan, S. Mukhopadhyay, and K.T. Shenoy, *Separation Science and Technology*, 2016, **51(17)**, 2790-2803.
- [19] N. Sen, K.K. Singh, A.W. Patwardhan, S. Mukhopadhyay, and K.T. Shenoy, *Separation Science and Technology*, 2018, **53(16)**, 2587-2600.
- [20] S. Sarkar, K.K. Singh, and K.T. Shenoy, *Separation and Purification Technology*, 2019, **209**, 608-622.
- [21] S. Sarkar, K.K. Singh, and K.T. Shenoy, *Industrial & Engineering Chemistry Research*, 2019, **58(33)**, 15307-15320.
- [22] X. Yu, H. Zhou, S. Jing, W. Lan, and S. Li, *Solvent Extraction and Ion Exchange*, 2018, **36(5)**, 480-498.
- [23] X. Yu, H. Zhou, Q. Zheng, S. Jing, W. Lan, and S. Li, *Chinese Journal of Chemical Engineering*, 2020, **28(6)**, 1504-1513.
- [24] R.A. Farakte, N.V. Hendre, and A.W. Patwardhan, *Industrial & Engineering Chemistry Research*, 2018, **57(50)**, 17192-17208.
- [25] F. Onink, C. Drumm, G.W. Meindersma, H.-J. Bart, and A.B. de Haan, *Chemical Engineering Journal*, 2010, **160(2)**, 511-521.
- [26] H. Yi, K.H. Smith, W. Fei, and G.W. Stevens, *Solvent Extraction and Ion Exchange*, 2020, **38(1)**, 88-102.
- [27] K.K. Singh, S.M. Mahajani, K.T. Shenoy, and S.K. Ghosh, *Industrial and Engineering Chemistry Research*, 2009, **48(17)**, 8121-8133.
- [28] S. Alzyod, M. Attarakih, A. Housseine, and H.-J. Bart, *Chemical Engineering Research and Design*, 2017, **117**, 549-556.
- [29] S. Alzyod, M. Attarakih, and H.-J. Bart, *Computer Aided Chemical Engineering*, 2018, **43**, 451-456.
- [30] N. Sen, K.K. Singh, A.W. Patwardhan, S. Mukhopadhyay, and K.T. Shenoy, *Progress in Nuclear Energy*, 2019, **111**, 125-137.
- [31] M.A. Hsia, and L.L. Tavlarides, *The Chemical Engineering Journal*, 1980, **20(3)**, 225-236.
- [32] S. Sarkar, K.K. Singh, S.M. Mahajani, and K.T. Shenoy, *Solvent Extraction and Ion Exchange*, 2020, **38(5)**, 536-554.
- [33] N. Sen, K.K. Singh, A.W. Patwardhan, K.T. Shenoy, *Solvent Extraction and Ion Exchange*, 2021, **39(3)**, 328-352.
- [34] X. Yu, H. Zhou, S. Jing, W. Lan, and S. Li, *Chemical Engineering Science*, 2019, **201**, 349-361.
- [35] X. Yu, H. Zhou, S. Jing, W. Lan, and S. Li, *Industrial and Engineering Chemistry Research*, 2020, **59(17)**, 8436-8446.
- [36] X. Yu, H. Zhou, S. Jing, W. Lan, and S. Li, *Chemical Engineering Science*, 2020, **226**, 115851.
- [37] H. Zhou, X. Yu, B. Wang, S. Jing, W. Lan, and S. Li, *Industrial and Engineering Chemistry Research*, 2021, **60(4)**, 1926-1938.
- [38] X.H. Guo, Q.Y. Zhao, T.A. Zhang, Z.M. Zhang, and S. Zhu, *JOM*, 2019, **71(5)**, 1650-1659.
- [39] A. Amokrane, S. Maaß, F. Lamadie, F. Puel, and S. Charton, *Chemical Engineering Journal*, 2016, **296**, 366-376.
- [40] C. Drumm, M. Attarakih, and H.-J. Bart, *Chemical Engineering Science*, 2009, **64(4)**, 721-732.
- [41] K.E. Wardle, T.R. Allen, M.H. Anderson, M.H., and R.E. Swaney, *AIChE Journal*, 2008, **54(1)**, 74-85.
- [42] K.E. Wardle, T.R. Allen, M.H. Anderson, and R.E. Swaney, *AIChE Journal*, 2009, **55(9)**, 2244-2259.
- [43] A.D. Santis, B.C. Hanson, M. Fairweather, *Chemical Engineering Science*, 2021, **242**, 116729.
- [44] R. Filimonov, Z. Wu, and B. Sundén, *Chemical Engineering Research and Design*, 2021, **166**, 135-147.
- [45] B. Swain, K.K. Singh, and A.K. Pabby, *Separation Science and Technology*, 2021, **56(16)**, 2848-2863.
- [46] B. Swain, K.K. Singh, and A.K. Pabby, *Solvent Extraction and Ion Exchange*, 2019, **37(7)**, 526-544.
- [47] N. Sen, K.K. Singh, A.W. Patwardhan, S. Mukhopadhyay, and K.T. Shenoy, CFD modelling to predict mass transfer in pulsed sieve plate extraction columns, 12<sup>th</sup> International Conference on Computational Fluid Dynamics in the Oil & Gas, Metallurgical and Process Industries (CFD-2017), 30 May-June 1 (2017), Trondheim, Norway.
- [48] X. Yu, H. Zhou, S. Jing, W. Lan, and S. Li, *Chemical Engineering Science*, 2021, **230**, 116184.

**This page is intentionally left blank**





# **BOOK REVIEW**

**This page is intentionally left blank**

# Computational fluid dynamics in nuclear reactor design and safety assessment

Dr. R.B. Grover

For the design of nuclear reactors with improved safety features, a thorough understanding of the complex phenomena at play inside the reactor core and various processes and safety systems is necessary. In recent years, computational fluid dynamics (CFD) has emerged as a dependable tool to develop that understanding and play with various parameters to understand their importance to design. The number of publications on the use of CFD for the design of reactors is too many and there is a need for a book that can help the designers to navigate this topic with ease. The book, edited by Prof. Jyeshtharaj B. Joshi and Prof. Arun K. Nayak, is a collection of 12 chapters and is an attempt in this direction.

The 1<sup>st</sup> chapter (Introduction) of the book provides a brief historical account of the development of nuclear reactors. It starts with notable early reactors and briefly describes the growth of nuclear power. It moves on to the safety in the design and the role of CFD in the safety assessment of the nuclear reactors.

The 2<sup>nd</sup> chapter titled Computational Fluid Dynamics is the longest chapter of the book. Authors illustrate the relationship of the 'physical world' with the 'mathematical world' and of the mathematical world with its numerical approximation. They remind the reader that the simpler versions of the models remain gross approximations of real-world engineering problems. However, they do provide specific insights. The chapter provides comprehensive coverage of turbulence models for single-phase flow, CFD modelling for multiphase flows including dense particulate flows. The chapter is immensely useful as a quick read for a reader who has some working knowledge of CFD.

The 3<sup>rd</sup> chapter describes physical processes involved in heat transfer, microscopic models for boiling, and macroscopic boiling models and their implementation in two-fluid CFD models for reactor-scale flows and geometries. The chapter is focussed on BWR and also covers bubble dynamics in the suppression pool.

The 4<sup>th</sup> chapter includes case studies on CFD modelling for the safety assessment of light-water-cooled reactors. Specifically, CFD modelling of coolant mixing in a test facility, and CFD modelling of horizontal stratified two-phase flows are presented.

The 5<sup>th</sup> chapter discusses the applications of CFD for designing passive safety systems for advanced nuclear reactors. CFD modelling of natural convection (buoyancy models and turbulence models) is discussed. CFD modelling of passive residual heat removal system, design of passive moderator cooling system, design of passive air-cooled condenser to condense steam coming from turbines, and design of venturi scrubber for filtered containment venting system are discussed as case studies for the applications of CFD in the design of passive systems for advanced reactors.

The 6<sup>th</sup> chapter is dedicated to CFD modelling of core melt accident scenarios in light and heavy water reactors. Modelling of in-vessel retention of corium in PHWRs, simulation of debris bed coolability, modelling to assess ex-vessel melt pool coolability are discussed as case studies.

The 7<sup>th</sup> chapter is focussed on using CFD for the assessment of reactor containment safety and covers the prediction of distribution inside the containment of hydrogen generated in a post-accident scenario due to oxidation of clad and other metallic components in the presence of steam. Subsequently, modelling of hydrogen recombination in plate type passive autocatalytic recombiners and tubular packed bed catalytic recombiner is presented. Modelling of hydrogen combustion and analysis of hydrocarbon fireballs are also discussed.

The 8<sup>th</sup> chapter is focused on CFD modelling of fire. It provides a useful introduction to various aspects of fire modelling and presents the fire hazard analysis of a nuclear power plant as a case study.

While chapters 3 to 8 are focussed on light water and heavy water-cooled

reactors, subsequent chapters are focused on some of the Generation IV reactors. The 9<sup>th</sup> chapter is focussed on CFD applications in the design of sodium-cooled fast reactors. The 10<sup>th</sup> chapter provides an overview of the use of CFD for graphite-moderated gas-cooled Very High-Temperature Reactor and the Molten-Salt Cooled Reactor. The 11<sup>th</sup> chapter delves deeper into various aspects of heat transfer and CFD modelling for molten salt reactors.

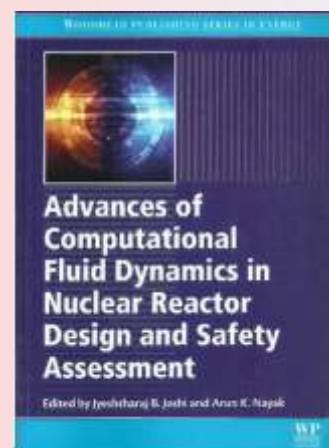
The last chapter titled 'conclusions and future recommendation' could have been expanded to include a section that presents an integrated view of all the chapters. Also, the recommendations should have been linked to what is included in the chapters of the book.

The book has a large number of high-quality figures and illustrations which make reading the book a pleasure.

The book is a must-read for researchers and designers working on the design and safety aspects of nuclear reactors.



R.B. Grover is Emeritus Professor, Homi Bhabha National Institute and Member, Atomic Energy Commission, India. His email is [rbgrover@hbni.ac.in](mailto:rbgrover@hbni.ac.in)



The book is edited by Prof. Jyeshtharaj B. Joshi and Prof. Arun K. Nayak

(ISBN: 978-0-08-102337-2 for printed version; 978-0-08-102338-9 for online version)

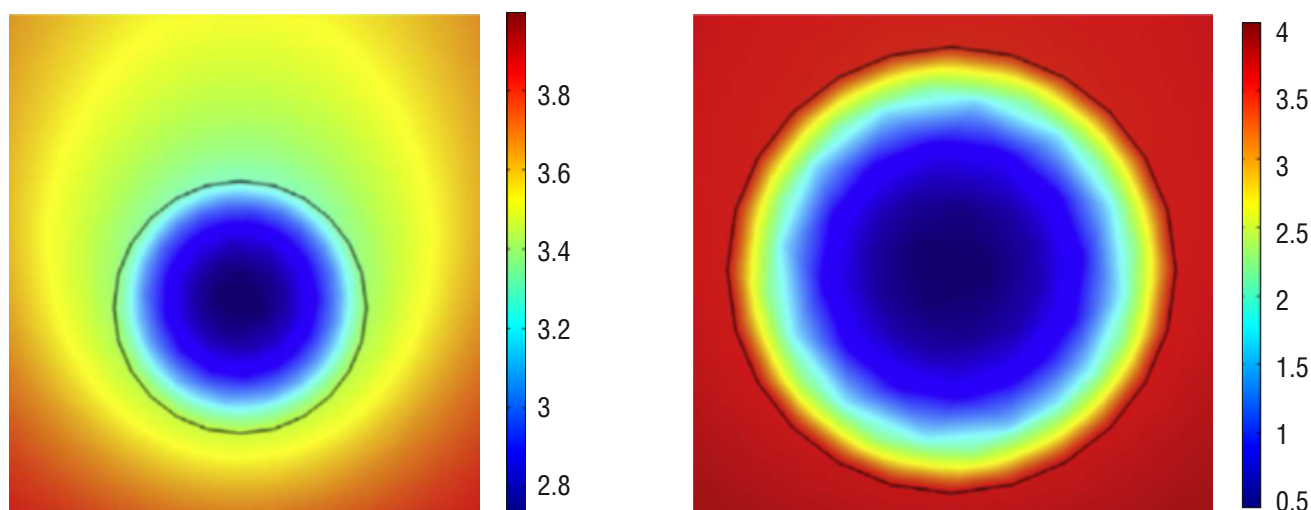
**This page is intentionally left blank**



# **RESEARCH SYNOPSIS**

**This page is intentionally left blank**

# Diffusion and decomposition of SO<sub>3</sub> in non-isothermal catalyst particles



Concentration profiles (in mol/m<sup>3</sup>) of SO<sub>3</sub> in catalyst pellet (right) and catalyst foam (left)

*Endothermicity of SO<sub>3</sub> decomposition reaction leads to high thermal gradients and lower reaction rates within the catalyst particles. Catalyst parameters, which can be tuned to minimize the gradients (concentration and temperature), are identified in this study.\**

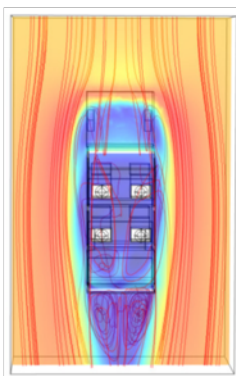
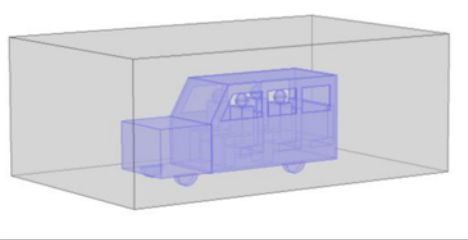
\*S. Sujeesh  
Chemical Technology Division  
Chemical Technology Group, BARC

**H**ydrogen is considered as a clean energy carrier in the future energy system. Sulphur-based water splitting processes (Iodine-Sulphur and Hybrid-Sulphur) are efficient and green technologies for hydrogen production. Decomposition of sulphuric acid is the high temperature and energy intensive step in these processes.

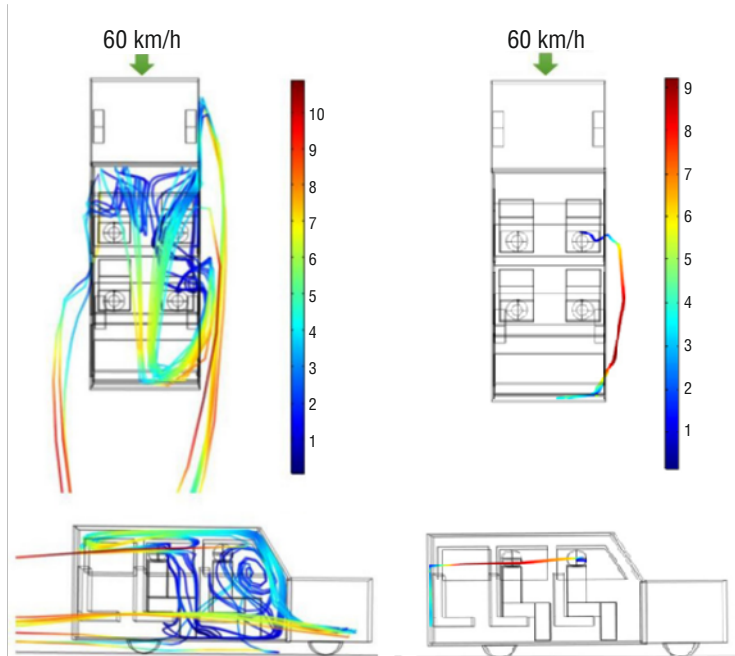
A recent report, (S. Sujeesh et al., 2021, 'Kinetic study and modeling of sulphuric acid decomposition using Cr-Fe<sub>2</sub>O<sub>3</sub> catalyst for sulphur based water splitting processes' Int J Hydrogen Energy , 46: 27282-27292) shows that the chromium doped iron oxide catalyst (Cr-Fe<sub>2</sub>O<sub>3</sub>) particles; less porous 'pellet' and porous 'foam' are non-isothermal particles for decomposition of SO<sub>3</sub>. This is due to high endothermicity of SO<sub>3</sub> decomposition reaction. Multiphysics numerical simulations of diffusion and decomposition of reactant, SO<sub>3</sub> in these non-isothermal particles are carried out by solving multi-physics reactive species transport, fluid flow and energy transport in porous media.

Kinetic parameters (activation energy and frequency factor) and effectiveness factor of Cr-Fe<sub>2</sub>O<sub>3</sub> catalysts (pellet and foam) obtained from experimental studies are also reported in this work. Experimental study shows strong pore diffusion resistance (small internal effectiveness factor) in these catalyst types. Effectiveness factor ( $\eta$ ) of these non-isothermal catalyst particles can be maximised by tuning various catalyst parameters such as particle size, porosity and effective thermal conductivity for which numerical simulations are immensely useful.

# Dispersion of aerosols inside SUV



Computational domain (top) and streamlines showing formation of wakes behind the SUV (bottom)



Trajectories of the ejected aerosols when a person sitting in 2nd row speaks (left) and when a person sitting in driver's seat speaks (right). The colour scales show the velocity (in m/s)

*Risk assesment for each passenger travelling in a SUV for four different scenarios. Significant recirculation of aerosols is possible even if all windows are completely open\*.*

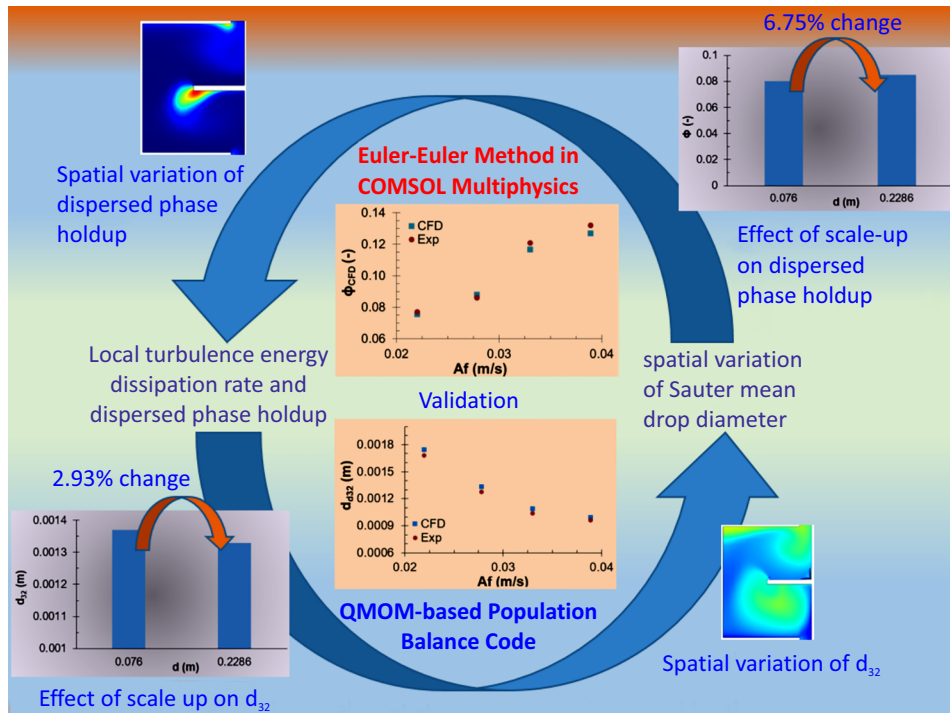
**C**OVID-19 rages on. Now that we need to live with the virus the onus is on us to prevent ourselves from contracting it. As life limps back to normalcy travelling of more than one person in a car/taxi becomes common. In Indian context we often travel in a non-air-conditioned car with windows open. In a recent study, (Sen & Singh, 2021, Physics of Fluids, 33(9): pp.095117) we have reported how aerosols (produced as one of the passengers speaks without mask on) can spread across the vehicle and affect other three co-passengers in a SUV (6 seater). Air exchange with the surroundings through open windows strongly affect the state of dispersion. An Euler-Lagrangian 3D CFD model implemented in COMSOL Multiphysics is used for the study.

Four sets of scenarios of practical interest have been considered. The first set shows the effect of vehicle speed on aerosol transport, the second set describes what happens when some of the windows are closed while the third describes how aerosol transport is affected by position of the passenger speaking. The fourth set of simulations describe how a gush of cross-wind affects aerosol transport. Simulation results reveal that when all windows are open aerosols can go out of one window and then return back to the vehicle interior through another window. Results also reveal that when passenger sitting in the second row speaks the aerosols generated may sweep the entire volume of the vehicle interior before going out through the open windows.

\*Nirvik Sen  
Chemical Engineering Division  
Chemical Engineering Group, BARC



# CFD–PB modelling of pulsed disc and doughnut column



*Coupled CFD-PB modelling is used to estimate dispersed phase holdup and Sauter mean drop diameter for liquid-liquid two-phase flow in a pulsed disc and doughnut column\*.*

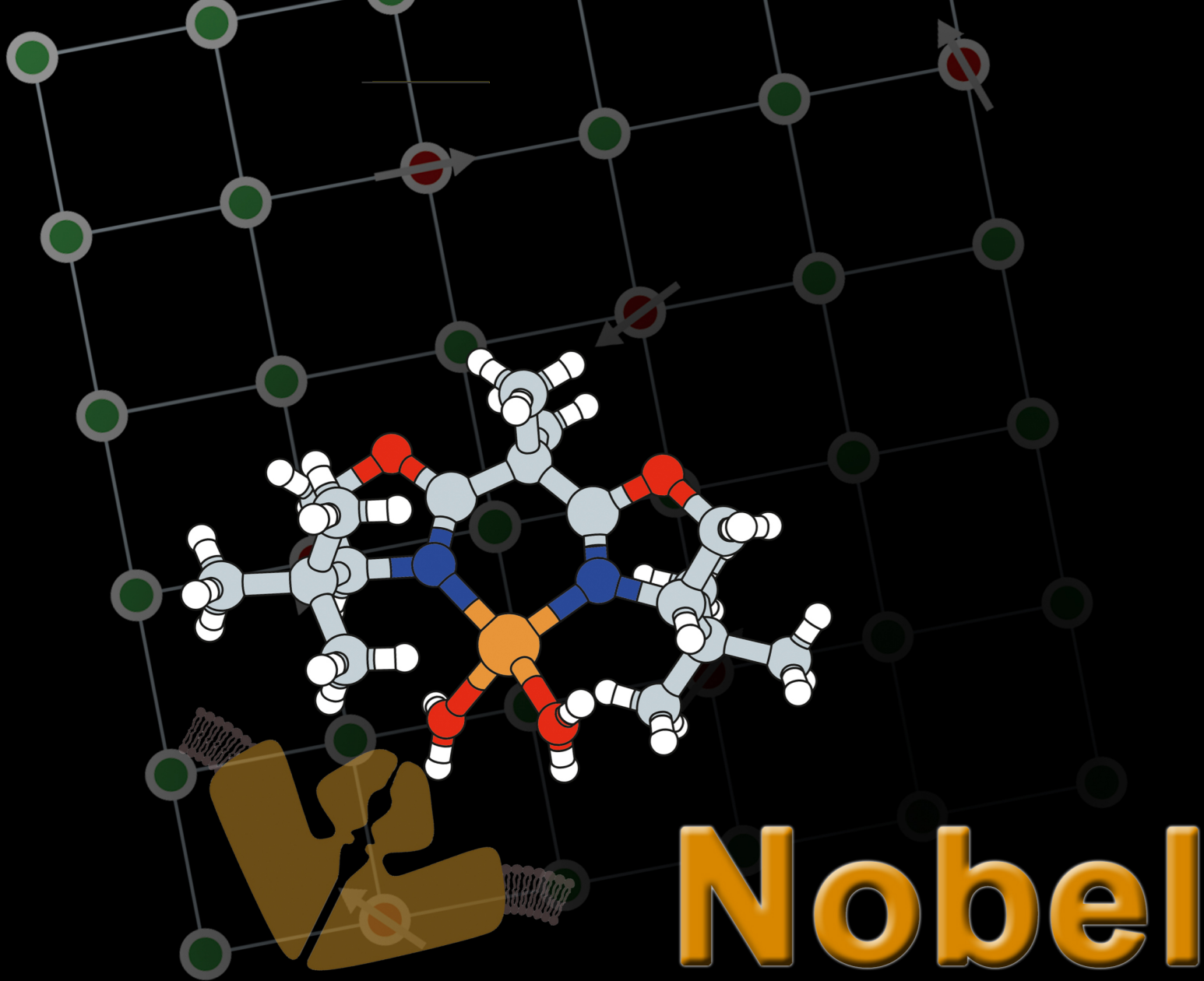
**P**ULSED DISC and DOUGHNUT COLUMN (PDDC) is a modified design of PULSED SIEVE PLATE COLUMN (PSPC). In a PDDC, sieve plates are replaced by disc and doughnut shaped plates. Unlike a PSPC which has sieve plates containing small holes, internals of PDDC allow it to handle feed containing solids without tendency of choking. For identical geometry and operating conditions, a PDDC has higher dispersed phase holdup than a PSPC resulting in lower HETP in PDDC compared to PSPC. In a recent article (Sarkar et al., 2020, 'CFD-PB Modelling of Liquid-liquid Two-phase Flow in Pulsed Disc and Doughnut Column', Solvent Extraction and Ion Exchange, 38:536) CFD-Population Balance (CFD-PB) modelling to estimate dispersed phase holdup and Sauter mean drop diameter in a PDDC is reported. Prediction of these hydrodynamic variables is important to estimate specific interfacial area available for mass transfer. An in-house Quadrature Method of Moment (QMOM) code is coupled with a CFD solver using the methodology pictorially shown above. The CFD-PB model is validated with experimentally measured dispersed phase holdup and drop diameter. Further, the CFD-PB model is used to check the validity of the scale-up scheme proposed in literature.

\*S. Sarkar  
Chemical Engineering Division  
Chemical Engineering Group, BARC

**This page is intentionally left blank**



# **FEATURES SEGMENT**



## Towards making chemistry **Greener**

Sk. Musharaf Ali

**T**he ultimate dream of a chemist is to create a new molecule by linking together small chemical building blocks via chemical reaction through fewer steps with high yield and zero waste generation in faster and reasonably cheap route.

To accomplish this, catalysts, which can breakdown molecule or join them together are often used. These substances that control and accelerate chemical reaction were earlier considered to be of two types: metal and enzymes. The metal to act as a catalyst should be free of oxygen and moisture, which is difficult to achieve in large scale. Moreover, metals are harmful to the environment. Enzyme, which build complicated molecules with amazing precision in living body usually can't be synthesized in the lab and needs to be isolated from biological sources. Since enzymes mostly get inactivated by heat and solvents, their in-vivo performance efficacy is much higher than in in-vitro condition.

These drawbacks lead to the discovery of third type catalysis, namely asymmetric organocatalysis. Benjamin List and David MacMillan are awarded the Nobel Prize in Chemistry 2021 for their development of a precise new tool for molecular construction: organocatalysis. This will have a great impact on pharmaceutical research, and will make chemistry greener.

In catalysis, there is an emphasis on not only making reactions faster, but also doing asymmetric or enantioselective reactions – those that produce only one mirror image (enantiomer) of handed molecules. As certain biological molecules – amino acids and sugars – only occur as single enantiomers, our bodies have an inherent ability to distinguish between enantiomers. This means the same molecule can smell of orange or lemon depending on its handedness.



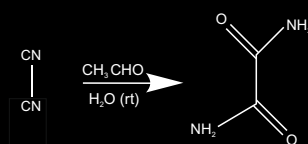
# Prize 2021

S-limonene molecule has lemon scent, while its mirror image (R-limonene) smell like orange.

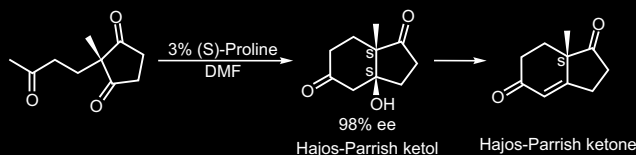
Liebig's synthesis of oxamide as the first organocatalysis reaction.

Asymmetric organocatalysts have been around for centuries, with an early example coming from Justus Liebig, who in 1860 reported that acetaldehyde catalyses cyanogen hydrolysis. Over the period of the 20th century, there were some reports of organic molecules acting as asymmetric catalysts (with varying success). But nobody thought of developing a comprehensive methodology or understanding how they work.

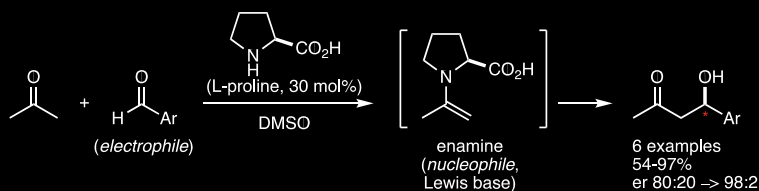
The Hajos-Parrish-Eder-Sauer-Wiechert reaction discovered in the 1970s was an example of asymmetric organocatalysis but didn't gain much attraction – possibly because the mechanism remained mysterious at the time.



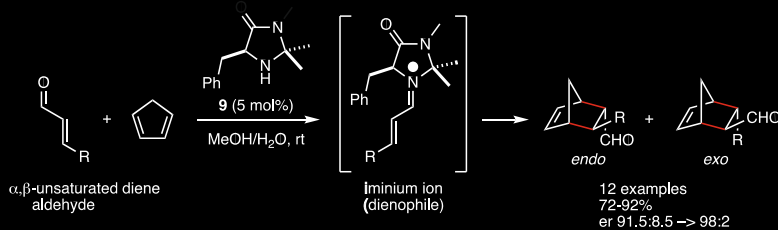
Liebig's synthesis of oxamide as the first organocatalysis reaction



The Hajos-Parrish-Eder-Sauer-Wiechert reaction



L-proline a brilliant asymmetric organocatalysis for intermolecular Aldol reaction



L-phenylalanine works as an asymmetric organocatalysis in Diels-Alder reaction

Because enzymes are such efficient catalysts, researchers in the 1990s tried to develop new enzyme variants to drive the chemical reactions needed by humanity. List decided to try and find out what happens when biocatalysts are stripped down to their most basic chemical form. In 2000, List and his team found out that one of them – proline – can on its own catalyse asymmetric aldol reactions with enantiomeric ratios up to 98:2.

List described proline as a micro-aldolase, an enzyme mimic that combines a nucleophilic centre (the amino group) and an acid–base co-catalyst (the carboxylic acid group). In the aldol reaction, proline binds to the ketone, forming an enamine intermediate that is more reactive than the ketone itself, as its highest occupied molecular orbital (HOMO) is higher in energy. Proline's handedness then infuses the reaction with asymmetry by only allowing the aldehyde to approach in one position.

MacMillan wanted to develop a catalyst for the Diels–Alder reaction, which could alleviate the shortcomings of the highly air- and moisture-sensitive metal catalysts. He discovered that a modified phenylalanine could catalyse asymmetric reactions between  $\alpha,\beta$ -unsaturated aldehydes and dienes with enantiomeric ratios up to 98:2.

L-phenylalanine works as an asymmetric organocatalysis in Diels-Alder reaction.

The phenylalanine derivative reacts with the unsaturated aldehyde to form an iminium ion, whose lowest unoccupied molecular orbital energy is lower than that of the aldehyde – making it more reactive. As in the case of List's enamine catalysis, iminium attaches itself to the substrate with a reversible covalent bond, which allows it to transfer its chirality onto the reagents.

Since then, the process they evolved has led to a “gold rush” in the catalysis field. The multitudes of new organocatalysts developed have helped drive a variety of chemical reactions, in turn accelerating pharmaceutical drug research. The asymmetric organocatalysts have allowed researchers to efficiently produce new molecules with complete certainty of the 3-D orientation.

When strychnine was first synthesized in 1952, it required 29 different chemical reactions and only 0.0009 per cent of the initial material formed strychnine and rest was wasted. In 2011, with organocatalysis, strychnine was built in just 12 steps with 7,000 times more production efficiency. Today, organocatalysis is recognized as the third pillar of asymmetric catalysis. List, MacMillan and a host of chemists inspired by their work, are discovering more and more organocatalytic reactions, including organocatalysed versions of classic asymmetric reactions, such as Mannich reactions, Michael additions and Friedel–Crafts reactions. Organocatalysis has even been merged with another green corner of chemistry: photocatalysis. The real revolution of this discovery is only surfacing now with extremely reactive catalysts that can do wonders that which cannot be achieved with enzymes or even with the most sophisticated metal complexes.

Given the huge growth and impact of organocatalysis in its present form, it will certainly be exciting to observe the development of the field upon heterogenization. In the coming years, various approaches for immobilization will be considered, with a focus on whether a novel methodology for the immobilization of organocatalysts could be discovered. It would be also interesting to see the explorations of noncovalent interactions and entrapment in nanosized materials in developing supported organocatalysts.

# Making sense out of senses

Dr. Birija Sankar Patro

## How we sense

our surroundings remained most enigmatic for ages in human minds. Our ability to sense heat, cold and touch is essential for survival and underpins our interaction with the world around us. However, the science behind the sense of touch and pain remained unknown for long.

Several breakthrough discoveries in the field of sensory systems had already recognised many Nobel prizes:

(1) Sherrington and Adrian, awarded 1932 Nobel prize in Physiology or Medicine "for their discoveries regarding the functions of neurons". (2) Erlanger and Gasser were awarded the Nobel prize in 1944 "for their discoveries relating to the highly differentiated functions of single nerve fibres. (3) Georg von Békésy, awarded the 1961 Nobel prize in Physiology or Medicine "for his discoveries of the physical mechanism of stimulation within the cochlea." (4) Ragnar Granit, Haldan Keffer Hartline and George Wald were awarded the 1967 Nobel prize in Physiology or Medicine "for their discoveries concerning the primary physiological and chemical visual processes in the eye. (5) Richard Axel and Linda B. Buck were awarded the 2004 Nobel prize in Physiology or Medicine "for their discoveries of odorant receptors and the organization of the olfactory system.

After a year and a half of devastating pandemic and extraordinary feats of developing multiple lifesaving vaccines, this year's Nobel prize in Physiology or Medicine was something of a surprise. It was awarded for discoveries related to a series of pioneering studies clarified how our neurons with thermosensors and mechanosensors works. The prize went to David Julius and Ardem Patapoutian.

In the 1990s, David Julius and colleagues at the University of California, San Francisco (San Francisco, CA, USA) asked most sought-after question to answer – as how do we perceive heat or temperature? In this regard, they have exploited unique characteristics of some of the spice derived molecules, e.g. Capsaicin from chilly, which triggers hot sensation. In their one of the most seminal paper (Caterina et al., 1997), Julius and colleagues conducted a series of experiments to isolate mRNAs from dorsal root ganglia, converted them into a library of complementary cDNAs and expressed them heterologously in heat insensitive embryonic kidney cells. These genetically transformed cells were challenged with capsaicin to evoke intracellular calcium. This led to discovery of mammalian homologue of the transient receptor potential (Trp) ion channel, later named as TRPV1, which uniquely responds to capsaicin and temperature in neurons. This seminal discovery further begets several other astounding findings by Julius and colleagues. In another 5 years, Julius and colleagues discovered cold and menthol-sensitive receptor (CMR1), a member of the TRP family of excitatory ion channels, and proposed that it functions as a transducer of cold stimuli in the somatosensory system (McKemy et al., 2002).

Interestingly, Patapoutian (Genomics Institutes of Novartis Research Foundation, San Diego and The Scripps Research Institutes, La Jolla, CA) independently began to answer his curiosity to understand the thermosensory properties of additional TRP family proteins. In their seminal discoveries, Patapoutian and colleagues have shown that TRPM8 responds to cold and cooling sensation of menthol and icillin (Peier et al., 2002) while TRPA1 responds to cold and garlic, wasabi and mustard (Story et al., 2003). This discovery of Patapoutian led to understanding that TRP1 variants are associated with diverged sensory functions in the living world. The variants of TRPV1 help camels and squirrels to resist high temperature while TRPA1 is used as infrared detector by some snakes.

A decade after the discovery of TRPV1 by Julius, Patapoutian and colleagues started tweeking to understand the enigmatic science behind the mechanical touch. Employing high risk brute force but systematic approach, Patapoutian team embarked upon identifying a mouse neuroblastoma cell and zeroed in 72 putative ion channels with hitherto unknown functions. In their years of research, they have knocked down these channels one by one by small interfering RNA

(siRNA) but failed miserably to identify the change in electrophysical parameters in response to pressure stimulation in knockdown cells. However, the eureka moment experienced when they finally knocked down one of the proteins, which showed dynamic changes in the inward current in response to pressure (Figure 1). They named these mechanically-activated channels as Piezo1 and Piezo2, after the Greek term for pressure, in their seminal discovery, published in "Science" in 2010 (Coste et al., 2010). Piezos are transmembrane proteins and expressed in several tissues in vertebrates. Its homologues are also found in invertebrates and plants.

Patapoutian with Sanjeev S Ranade, one of the key Indian researchers in his team, showed that Piezo1 knockout mice are embryonically lethal due to defects in vascular remodeling and inability of responding to shear stress of blood flow by endothelial cells, due to lack of Piezo1 (Ranade et al., 2014a). Intriguingly, they discovered that Piezo2 knockout mice are viable. They showed that mice lacking Piezo2 exhibit a profound loss of touch sensation. In their seminal discovery, they reveal that "We find that touch and pain sensation are separable, suggesting that as-yet-unknown mechanically activated ion channel(s) must account for noxious (painful) mechanosensation." (Ranade et al., 2014b). More recently, Patapoutian extended the science behind the function of Piezo in baroreflex and blood pressure and advocated its critical sensory function in other species too (*Drosophila*, *Cenorhabditis* and *Arabidopsis*).

The discoveries of Julius and Patapoutian have immense translation opportunities. TRP channels are considered as attractive druggable targets for managing pain. Both agonists and antagonists of TRP channels have therapeutic potentials for relieving muscle and bone joints. For example, resiniferatoxin, an analogue of capsaicin, show excellent effect in relieving pain in dogs with bone cancer. Mavatriptan, a second-generation drug, has recently found to be effective against osteoarthritic pain. Although pharmacological targeting of TRP channels was focussed on pain but its

potential hitherto extended to many new clinical conditions like respiratory disorders, neurological and psychiatric diseases, diabetes and cancer. The discoveries of Julius and Patapoutian undoubtedly opened up whole new era of our understanding the sensory function behind pain, touch, pressure and other internal homeostatic process.

".....The challenge is to develop drugs that don't have side effects outside of pain and to develop drugs that diminish chronic pain but don't interfere with the pain system doing its job as an acute warning system," .....David Julius.

Albeit discoveries are sometime accidental and serendipitous, the seminal discoveries of sensory channels by Julius and Patapoutian was based on "curiosity driven research" and "research driven curiosity" for decades. Experimental failures, long lonely hours in the labs, clueless real science than expected, sometime too good to believe the results are the ways forward to great science – In short, there is no shortcut for achieving the best.

Patapoutian tweeted once ".....But there is hope! My first grant after cloning PIEZOs was triaged. But @NIH did ultimately fund the work that showed PIEZO2 is the principal mechanosensor for touch and proprioception. Message: stay positive, don't doubt yourself, and keep trying."

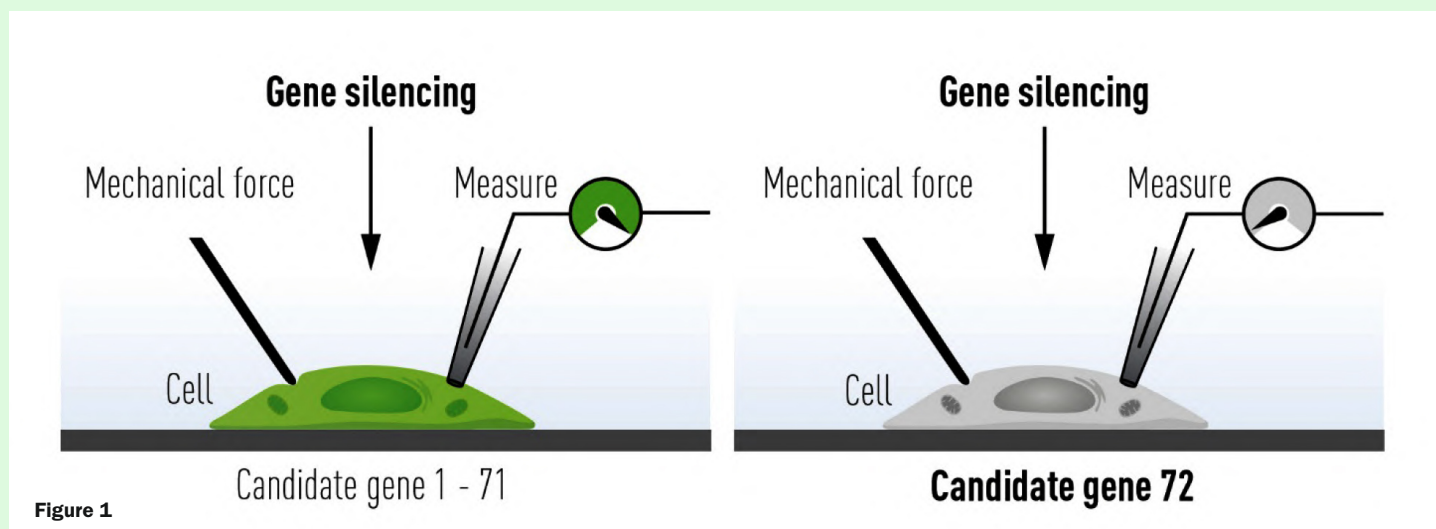
When Dr Julius was asked what did he learn from his Nobel Laureate mentors (Randy Schekman and Richard Axel), he said

".....I worked with them long before they got their Nobel Prizes but, you know, they're all unbelievably curious, that's the main thing. But you know they have an intensity and a curiosity that's just really special."

The Nobel Prize is wonderful recognition of these discoveries," Congratulations to Dr Julius and Dr. Patapoutian for the Nobel Prize in Physiology or Medicine; your success is great motivation for all the researchers to excel in science while answering fundamental questions.

## References

1. Caterina, M. J., Schumacher, M. A., Tominaga, M., Rosen, T. A., Levine, J. D. and Julius, D. (1997). The capsaicin receptor: a heat-activated ion channel in the pain pathway. *Nature* **389**, 816-824.
2. Coste, B., Mathur, J., Schmidt, M., Earley, T. J., Ranade, S., Petrus, M. J., Dubin, A. E. and Patapoutian, A. (2010). Piezo1 and Piezo2 are essential components of distinct mechanically activated cation channels. *Science* **330**, 55-60. [10](#)
3. Mckemy, D. D., Neuhauser, W. M. and Julius, D. (2002). Identification of a cold receptor reveals a general role for TRP channels in thermosensation. *Nature* **416**, 52-58.
4. Mckemy, D. D., Neuhauser, W. M. and Julius, D. (2002). Identification of a cold receptor reveals a general role for TRP channels in thermosensation. *Nature* **416**, 52-58.
5. Peier, A. M., Moqrich, A., Hergarden, A. C., Reeve, A. J., Andersson, D. A., Story, G. M., Earley, T. J., Dragoni, I., McIntyre, P., Bevan, S. and et al. (2002). A TRP channel that senses cold stimuli and menthol. *Cell* **108**, 705-715.
6. Ranade, S. S., Qiu, Z., Woo, S.-H., Hur, S. S., Murthy, S. E., Cahalan, S. M., Xu, J., Mathur, J., Bandell, M., Coste, B. et al. (2014a). Piezo1, a mechanically activated ion channel, is required for vascular development in mice. *Proc. Natl. Acad. Sci. USA* **111**, 10347-10352.
7. Ranade, S. S., Woo, S.-H., Dubin, A. E., Moshourab, R. A., Wetzel, C., Petrus, M., Mathur, J., Bégay, V., Coste, B., Mainquist, J. et al. (2014b). Piezo2 is the major transducer of mechanical forces for touch sensation in mice. *Nature* **516**, 121-125.
8. Story, G. M., Peier, A. M., Reeve, A. J., Eid, S. R., Mosbacher, J., Hricik, T. R., Earley, T. J., Hergarden, A. C., Andersson, D. A., Hwang, S. W. et al. (2003). ANKTM1, a TRP-like channel expressed in nociceptive neurons, is activated by cold temperatures. *Cell* **112**, 819-829.



**Piezo and Piezo2 mechanoreceptors were discovered in neuroblastoma cells through gene silencing of candidate 72 genes expressions.**  
Adapted from <https://www.nobelprize.org/prizes/medicine/2021/press-release/>

# Reliably predicting global warming

Dr. Krishna  
Kumar Singh

**T**he 2021 Nobel Prize in Physics has been jointly awarded to three scientists for their study of role of humanity in the climate change of our planet Earth. According to the Nobel Committee for Physics, the discoveries recognized for 2021 Nobel Prize demonstrate that our knowledge about the climate rests on a solid scientific foundation, based on a rigorous analysis of observations. The first half of the Nobel Prize is shared by Prof. Syukuro Manabe of Princeton University, USA and Prof. Klaus Hasselmann of the Max Planck Institute for Meteorology in Hamburg, Germany “for the physical modelling of Earth's climate, quantifying variability and reliably predicting global warming”. The other half of this Nobel Prize is rewarded to Prof. Giorgio Parisi of the Sapienza University of Rome, Italy “for the discovery of the interplay of disorder and fluctuations in physical systems from atomic to planetary scales”. This is the first time the Physics Nobel Prize is shared by a climate scientist. The climate change can be described as a complex physical system which is defined by its disorder. The Earth's



**This is the first time the Physics Nobel Prize is shared by a climate scientist**

atmosphere is a complex and chaotic system in which the weather is highly unpredictable on the day timescale and therefore it is extremely important to explore the reliability of climate models on the timescale of months and years. The models developed by Prof. Manabe have made fundamental contributions in understanding the human caused climate change and dynamical mechanisms. Prof. Hasselmann has proposed a model to connect the short-term climate phenomena (rain and other types of weather) to the long-term climate phenomena (ocean and atmospheric currents). This work laid the foundation for studies to establish the influence of climate change on events like intense rainstorm, drought and heat wave and to detect the impacts of climate change. Ordered phenomena emerge from the disordered and chaotic systems through the subtle mechanisms and fluctuations. Prof. Parisi discovered the interplay between disorder and fluctuations in the complex physical systems ranging from a tiny collection of atoms to the atmosphere of planets. This study suggested that if a completely random system is analyzed properly, it can make a robust prediction for a collective behavior arising from the fundamentally disordered, chaotic and frustrated systems on all length scales from materials like glass to the climate.

## About the authors



**Sk. Musharaf Ali**, PhD, presently heading the Laboratory Services Section, ChEG. He is keenly associated with BARC News Letter. His main thrust of research is in the field of computational and experimental molecular modeling for the design, development and demonstration of existing and

novel molecular system for efficient extraction and separation of radionuclide and isotopes; nanomaterials for water purification, glass formulation for nuclear waste immobilization and tritium barrier materials using the tools of ab-initio and MD simulations. He has over 265 publications to his credit in journals, symposia, conferences and book chapters. He is editorial board member of The Open Chemical Engineering Journal.



**Dr. Birija Sankar Patro** is currently with the Bio-Organic Division, BARC. His areas of research include DNA repair and autophagy signalling in Cancers



**Krishna Kumar Singh**, a Ph. D. from the Homi Bhabha National Institute, Mumbai, is an astrophysicist with specialization in the field of high energy gamma ray astronomy and observational cosmology. He is from the 51st batch of BARC Training School under the Physics discipline. His main area of research includes

multi-wavelength study of astrophysical sources, propagation effects of very high gamma ray photons in the Universe, and gamma ray astronomy with the space and ground-based telescopes.





# **BOOK REVIEW**

**This page is intentionally left blank**

# Natural hazards, impact assessment and eco-engineering through Artificial Intelligence

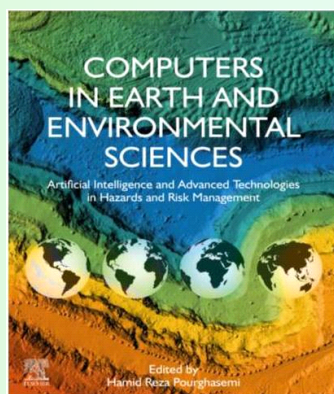
Tirumalesh Keesari

With a commanding experience in spatial modeling and multi-criteria decision-making methods and being an author of over 150 peer reviewed journal articles, the editor Dr. Hamid Reza, has compiled this thoughtful book with chapters pertaining to natural and environmental hazards and role of machine learning techniques. The book is well organized and covers three main themes; i) natural and environmental hazards, ii) advanced tools and technologies in risk management and iii) future challenges in computer applications. These themes are detailed through 48 diligently written chapters mostly contributed by researchers, faculty and scientist who have sound knowledge on the current advancements in the respective fields. Even though most of the chapters describe current research in Iran, the editor could successfully expand the coverage of the book by including research works of over 20 countries both developed and developing. By maintaining a proper blend of basic and applied research, the editor has also made sure that the book won't look monotonous and readers are encouraged to read through all chapters.

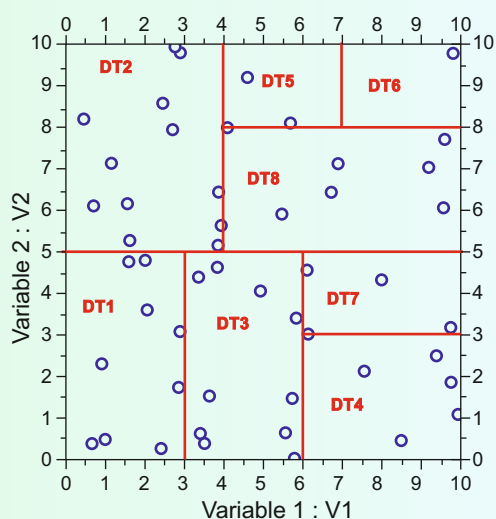
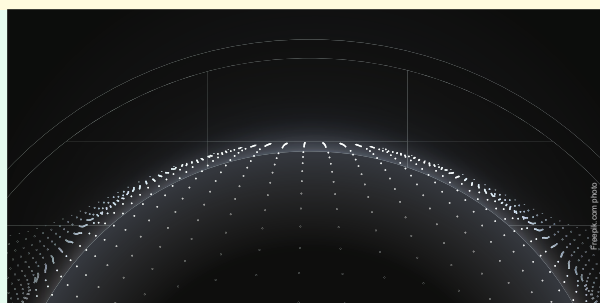
Basic research chapters that caught my eye include those by Hamidreza Mosaffa et al. on "Application of machine learning algorithms in hydrology". This chapter presents an overview on the application of machine learning and deep learning in the subfields of hydrology, including flood, precipitation estimation, water quality, and groundwater. It is not always easy to monitor the contaminant in situ with the available instrumentation in an economically viable manner. In this respect the chapter on "Application of data driven approach" is a useful and timely contribution by D. Saha and K. Tirumalesh (self). Here we discussed how electrical conductivity of water samples can be used as a potential proxy for obtaining Cl<sup>-</sup> concentration through decision tree model. The chapter also informs about the limitations of such estimations and suggests methods for betterment. In addition, there are many interesting chapters on the application of Long - short term memory, neural networks, spatial modeling, analytical hierarchy

process (AHP) and meta-heuristic techniques, and also chapters on some basic aspects of erosion and land degradation, and multi-fractal analysis of basin drainage.

Hazard prediction has been covered extensively in this book. Many chapters were dedicated to evaluation of natural hazards, like landslides, forest fires, soil degradation, soil erosion and impact of land use changes, etc. Other chapters of interest are drought hazard assessment using random forest method and environmental impacts assessment using spatial multi-criteria decision analysis. Apart from natural hazard prediction, the book also contains chapters dealing with application of advanced tool to evaluate the eco-engineering practices for restoration of soil health as well as other natural resources. There are two chapters on the COVID related research, one of them by Abdullah Kaviani et al., which highlights the direct linkage with human activities and global warming gas emission with a soft caution to reduce emission of global warming gases. Another chapter



Edited by:  
Hamid Reza Pourghasemi  
(<https://doi.org/10.1016/C2020-0-03210-X>)



Sample schematic details of decision tree - model domain split

by Soheila Pouyan et al., draws parallels related to COVID-19 pandemic impacts between Iran and the world averages using polynomial curve fitting. The authors admit there is a lack of information on the protocols to contain the virus spread.


This book is a good medium to create awareness among the upcoming researchers who are new to data treatment through machine learning and other data handling algorithms.

Researchers and professionals in earth and environmental sciences who require the latest technologies and advances multi-hazard assessments, natural and manmade hazards, risk management in hazards, remote sensing and spatial modeling, restoration of natural resources will find this book to be a valuable source of information.



Tirumalesh Keesari is a Scientific Officer in Isotope Hydrology Section of Isotope Radiation and Application Division in BARC and also Associate Professor in Chemical Sciences in HBNI. His research interests include water contamination, geochemical modeling, groundwater recharge, spring revival in Himalayan regions, coastal salinity and studies on extreme climatic regions of India through application of isotope technologies. He has over 80 international journal publications to his credit and also a recipient of DAE Science and Technology Award and Indo-US Science and Technology Award.

**This page is intentionally left blank**



# **TECHNOLOGY TRANSFER & HONORS**

**This page is intentionally left blank**

# BARC develops Titanium Diboride Ceramics

Materials Group, BARC

The technology for synthesis and densification of Titanium diboride ( $TiB_2$ ) based ultra-high temperature ceramics, with potential applications in development of body armours, high-end cutting tools, molten metal crucibles and wear-resistant-parts was developed in-house by Materials Processing and Corrosion Engineering Division, Materials Group, BARC.  $TiB_2$  is gifted with attractive properties such as high melting temperature, high hardness, good thermal conductivity and chemical inertness. The technology was transferred to a Gujarat-based firm for industry-scale production.

## $TiB_2$ ceramics: From powder form to densified shapes

- (i) Synthesizing of phase pure  $TiB_2$  powder by carbothermic reduction of titanium oxide in the presence of boron carbide.
- (ii) Densification of  $TiB_2$  powder into high dense pellets by hot pressing at  $1800^\circ C$  in high vacuum at a pressure of 32 Mpa.



$TiB_2$  chunks (Top) Flat dense shapes of  $TiB_2$  (Bottom)

# BARC scientist elected fellow of Indian National Science Academy



**Dr. Prasun K. Mukherjee**, Scientific Officer/H and Head, Environmental Biotechnology Section, Nuclear Agriculture and Biotechnology Division, has been elected as a Fellow of the prestigious Indian National Science Academy (INSA), New Delhi.

Dr. Mukherjee joined BARC as a Scientific Officer/ SD in 1993, on completion of Ph.D. (Plant Pathology) from G.B. Pant University of Agriculture and Technology, Pantnagar, as a "Dr. K.S. Krishnan DAE Research Fellow". Dr. Mukherjee is an internationally acclaimed scientist, known for his high quality, well-cited publications, and technologies in the area of biological control of plant diseases, and biocomposting using the beneficial fungus *Trichoderma*.

Dr. Mukherjee is a Fellow of the National Academy of Sciences, India (NASI) and the National Academy of Agricultural Sciences (NAAS). He is a recipient of Homi Bhabha Science and Technology Award, Fulbright-Nehru Academic and Professional Excellence Fellowship, DAE Group Achievement Award (twice, as a group leader), VASVIK Award, BOYSCAST Fellowship, and many other accolades from various professional societies. He has been a visiting scholar/postdoctoral fellow at the Technion-Israel Institute of Technology, Haifa, and Texas A&M University, College Station. He is on the editorial board of international journals of repute like "Fungal Genetics and Biology" and "3 Biotech", and has edited two books entitled "Trichoderma-Biology and Applications" and "Genomics of Soil- and Plant-associated Fungi".



**Research reactors Dhruva & CIRUS in BARC, Trombay**

Edited & Published by:  
Scientific Information Resource Division  
Bhabha Atomic Research Centre, Trombay, Mumbai 400 085, India  
BARC Newsletter is also available at URL:<http://www.barc.gov.in>